

Tracing Gas Properties in Merging Galaxy Clusters in *Magneticum*



Bachelor thesis at the Faculty of Physics
Ludwig-Maximilians-University Munich

Submitted by

Johannes Stoiber

Supervised by

PD Dr. habil. Klaus Dolag

Dr. Ildar Khabibullin

Munich, 15th of July 2022

Nachverfolgung von Gaseigenschaften in
kollidierenden Galaxienhaufen in
Magneticum



Bachelorarbeit an der Fakultät für Physik der
Ludwig-Maximilians-Universität München

Vorgelegt von

Johannes Stoiber

Betreut von

PD Dr. habil. Klaus Dolag

Dr. Ildar Khabibullin

München, den 15.07.2022

Contents

1	Introduction	1
1.1	Motivation	1
1.2	Cosmology	2
1.2.1	Friedmann Equation	2
1.2.2	Cosmological Parameters	4
1.2.3	Distance Measures	5
1.3	Dynamics of Galaxy Clusters	6
1.3.1	Formation of Galaxy Clusters	6
1.3.2	Mass and Radius Definitions	7
1.3.3	Accretion of Substructures	8
1.3.4	Mergers	9
1.3.5	Rankine-Hugoniot Jump Conditions	11
1.4	Properties of the ICM	13
1.4.1	Isothermal Beta Model	14
1.4.2	Time Scales and Length Scales	14
1.4.3	Entropy in the ICM	17
1.4.4	Metallicity in the ICM	19
2	Methodology	21
2.1	N-Body Simulations	21
2.1.1	Calculation of the Gravitational Potential	21
2.1.2	Time Integration	22
2.2	Hydrodynamical Simulations	24
2.2.1	SPH	26
2.3	Magneticum	28
2.3.1	Snapshot File	28
2.3.2	Services and CosmoWebPortal	29
2.3.3	Units	30
2.4	Center of Mass	30

2.5	Calculating Radial Velocities	31
2.6	Phase Diagrams	31
3	Analysis	33
3.1	Projected Scatter Plots	33
3.2	Phase Diagrams	40
3.3	Tracing Particles	40
3.3.1	Sub Sample	40
3.3.2	Tracing of Gas Properties of the Sub Sample	44
3.3.3	Particles Tracks	49
3.3.4	Tracing the Radial Velocities of the Tracks	49
3.4	Temperature and Gas Density Jump Ratios and Image Arithmetic	52
3.5	Radial Profiles via Radial Binning	58
3.5.1	Profiles over the Infalling Substructure	58
3.5.2	Profile over the Whole Cluster	59
3.5.3	Profile over the Outgoing Shock	62
4	Summary and Conclusion	65
4.1	Summary	65
4.2	Problems	66
4.3	Conclusion	66
	Appendices	77
A	Derivation of the Rankine-Hugoniot Jump Conditions	79
B	Methodology	83
B.1	Python Code Orbit	83
B.2	Comparison of a Gaussian and B_2 -spline Kernel for SPH	86
C	Snapshot File	87
C.1	Snapshot Blocks	87
C.2	Snapshot Header	88
D	Data of the Investigated UID1 Cluster	89

Chapter 1

Introduction

1.1 Motivation

Galaxy clusters play an important role in cosmology, the mystery of dark matter, plasma physics and in many other areas. Structure formation models can be tested by measuring the abundance of large halos like galaxy clusters (Kravtsov and Borgani 2012). Dark Matter was first observed by Fritz Zwicky in the Coma Cluster by measuring the velocity dispersion of individual galaxies. Their velocities are so high that the cluster should fly apart if they are only bound together by the mass of the luminous matter. He stated that dark matter needs to have a much higher density within the cluster than previously expected (Zwicky 1933). Another interesting galaxy cluster is the so called Bullet Cluster shown in (Fig. 1.4). It consists of a main cluster through which a sub cluster passes at a high velocity. Currently this Bullet already had one core passage and now moves away from the center. By creating gravitational lensing maps the complete mass of both clusters can be measured, revealing, that the main component of the matter is separated from the X-ray emitting gas that used to sit in between the galaxies but was stripped from them and now sits in the middle of their respective stellar components. The gas clouds are slowed down by ram pressure, whereas galaxies and DM pass through each other and themselves. From this offset an upper bound to the self-interaction cross section of dark matter can be estimated. The result suggests that dark matter is collisionless. The fact, that the mass peak calculated from the lensing maps is coincident with the galaxies and not with the gas clouds is regarded as a proof for the existence of dark matter by some (Clowe et al. 2006, Markevitch et al. 2004). As this X-ray emitting gas is fully ionized it can be used as a laboratory for plasma physics. In merging systems like the Bullet Cluster there will be shock fronts within the gas. A shock will heat up ions immediately, while electrons are compressed adiabatically to a lower temperature, because their thermal velocity is higher than the shock velocity. They then equilibrate via Coulomb collisions over a certain time scale. But some observations suggest an immediate shock heating of the electrons (ZuHone and Su 2022). A sketch of the gas of a merging system like the Bullet Cluster is shown in (Fig. 1.1).

The gas-dark matter offset was simulated e.g. by (Mastropietro and Burkert 2008) confirming, that such a system agrees with the currently accepted Λ CDM cosmology model. Many other features of observed galaxy clusters have been simulated in the last decades. In order to not just capture the physics of one specific cluster, but to study the structure formation in a cosmological framework cosmological simulations like *Magneticum*¹(Dolag et al. 2016) have been and are performed. The goal of this work was to investigate how different particles types move and to trace the properties of gas within merging galaxy clusters in such simulations.

¹<http://magneticum.org/index.html>

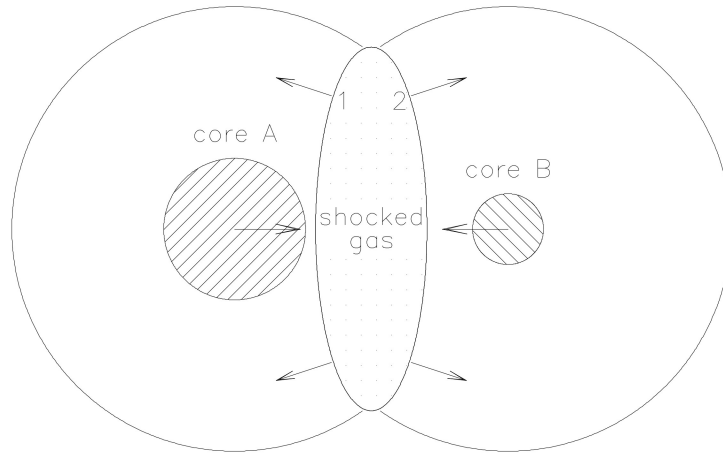


Figure 1.1: The gas of merging galaxy clusters; shaded circles depict dense cores of the colliding subclusters; The shock fronts 1 and 2 in the central region will propagate to the outskirts without affecting the cores; taken from (Markevitch and Vikhlinin 2007).

The results were supplemented with radial profiles over certain features of the cluster. In the Introduction (Sec. 1), the cosmological framework, galaxy cluster formation and basic cluster physics, focusing on mergers and the intracluster medium (ICM), is presented. Secondly the Methodology (Sec. 2), from simulation tools to basic mathematical manipulations is explained. The results of tracing gas particles and their properties, dark matter and star particles and the radial profiles are displayed in (Sec. 3). Finally the results are summarized in (Sec. 4).

1.2 Cosmology

1.2.1 Friedmann Equation

Galaxy clusters and the physics governing them act over cosmological distances. They can give not only insight into the behavior of plasma and dark matter but also into cosmological parameters (Kravtsov and Borgani 2012, p. 4). In order to be able to understand galaxy cluster we need to know the basics of cosmology.

The first indication of the expansion of the universe was given 1917 by Vesto Slipher (1875-1969) and Carl Wirtz (1876-1939) who observed that the majority of the then so-called nebulae were moving away from us. In the early 1930s Edwin Hubble and Milton Humason could determine that not only are they moving away from us but also do that in an accelerating fashion as their distances become larger.

The second realization that led to modern cosmology was the 1915 released Theory of General Relativity (GR) by Albert Einstein (1879 - 1955), which determines how the matter and energy content of the universe effect the geometry of space and how the geometry in return governs the motion of matter and energy. In 1922 Alexander Friedmann derived a class of cosmological models from GR. George Lemaître (1894 - 1966) also came to the same conclusions independently and was the first to connect these models to the receding motion of the galaxies. Today this is known as the Hubble-Lemaître law (if $v \ll c$ and $D \ll \frac{c}{H_0}$)

$$v = H_0 D \tag{1.1}$$

where v is the escape velocity, D the distance of the galaxy and H_0 the Hubble constant. In this case it also can be shown that

$$1 + z = \left(\frac{c + v}{c - v} \right)^{1/2} \approx 1 + \frac{v}{c} \implies v \approx cz \quad (1.2)$$

In addition to the Theory of General Relativity two important assumptions are made:

1) *Isotropy*: Over large scales the properties (e.g. matter density) of the universe are the same in every direction. 2) The cosmological principle: Our position in the universe is not distinguishable from any other, i.e. for every other observer the first assumption also has to be true, which makes the universe *homogeneous*.

The four dimensional space-time can be described by a metric (4×4 -matrix $g_{\mu\nu}$). A metric that satisfies both above assumptions is called the Robertson-Walker (RW) metric given by the line element

$$ds^2 = -c^2 dt^2 + a^2(t) \left[dw^2 + f_K^2(w) d\Omega^2 \right] \quad (1.3)$$

where $a(t)$ is the scale factor that describes the expansion of space, $dw = \frac{dr}{\sqrt{1+Kr^2/4}}$ is the radial coordinate corrected for curvature K and $d\Omega = d\theta^2 + \sin^2 \theta d\varphi^2$. Also the radial function $f_K(w)$ depends on the sign of K and is equal to w if $K = 0$ (flat geometry). Today measurements show that $K \approx 0$ and therefore the RW metric can be written as $ds^2 = -c^2 dt^2 + a^2(t) [dr^2 + r^2(d\theta^2 + \sin^2 \theta d\varphi^2)]$.

Because of the expansion of space electro-magnetic waves moving through it get stretched according to the scale factor which leads to a *redshift* z of the photons. For a comoving light source and a comoving observer w is equal to 0 and therefore also $r = 0$. For light $ds = 0$ is true. The RW metric becomes $c|dt| = a(t)dw$ and with some calculations one ends up with

$$\frac{v_e}{v_o} = \frac{a(t_o)}{a(t_e)} = \frac{\lambda_o}{\lambda_e} = 1 + \frac{\lambda_o - \lambda_e}{\lambda_e} =: 1 + z \quad (1.4)$$

where the subscript e stands for the emitting reference frame and o for the observing reference frame. ν and λ are the frequency and the wavelength of the photon respectively. $a(t)$ and z are the scale factor and the redshift. Most of the time $a(t_o) \equiv 1$ and $a(t_e) = a(t)$ are convention.

Finally, inserting the RW metric into the Einstein field equations

$$G_{\alpha\beta} = \frac{8\pi G}{c^4} T_{\alpha\beta} - \Lambda g_{\alpha\beta} \quad (1.5)$$

where $G_{\alpha\beta}$ is the Einstein tensor which is constructed out of the curvature tensor, $T_{\alpha\beta}$ is the energy-momentum tensor, $g_{\alpha\beta}$ is the metric and the cosmological constant Λ describes the dark energy, yields the Friedmann Equations

$$\begin{aligned} \left(\frac{\dot{a}}{a} \right)^2 &= \frac{8\pi G}{3} \rho - \frac{Kc^2}{a^2} + \frac{\Lambda c^2}{3} \\ \frac{\ddot{a}}{a} &= -\frac{4\pi G}{3} \left(\rho + \frac{3P}{c^2} \right) + \frac{\Lambda c^2}{3} \end{aligned} \quad (1.6)$$

A RW metric that satisfies these equations is called *Friedmann-Lemaître-Robertson-Walker* (FLRW) metric (Bartelmann 2019, p. 2-11).

1.2.2 Cosmological Parameters

The cosmological density parameters describe the content of the universe which consists of relativistic particles (*radiation*, also neutrinos are included here) and non-relativistic particles (*dust*). Their density evolution can be described by

$$\rho(a) = \rho_0 a^{-3(1+w)} \quad (1.7)$$

where a is the scale factor and $w = \frac{P}{\rho c^2}$ is the dimensionless ratio of pressure and energy density. For radiation $w = 1/3$ and for dust it is $w = 0$. Therefore we get

$$\rho_r(a) = \rho_{r,0} a^{-4} \quad \rho_m(a) = \rho_{m,0} a^{-3} \quad (1.8)$$

For $w = -1$ the density evolution becomes $\rho_\Lambda(a) = \rho_{\Lambda,0}$ (constant), which is equal to the scaling relation of the cosmological constant. That means Λ can also be a form of matter or energy, which pressure equals a negative energy density.

Inserting (Eq. 1.8) into (Eq. 1.6) yields

$$\left(\frac{\dot{a}}{a}\right)^2 = \frac{8\pi G}{3} \rho_{r,0} a^{-4} + \frac{8\pi G}{3} \rho_{m,0} a^{-3} - K c^2 a^{-2} + \frac{\Lambda c^2}{3} \quad (1.9)$$

We can define the Hubble function as the relative cosmic expansion rate and the Hubble constant as its value at the current time (Bartelmann 2019, p.14f)

$$H(t) := \frac{\dot{a}}{a} \quad H_0 := H(t_0) \quad (1.10)$$

Often cosmological measurements are given in terms of the dimensionless Hubble constant h given by $H_0 = h \, 100 \, \text{km s}^{-1} \text{Mpc}^{-1}$, which characterizes the uncertainty of H_0 . One can also find the parameter $h_{50} = \frac{H_0}{50 \, \text{km s}^{-1} \text{Mpc}^{-1}}$ sometimes. (Schneider 2006, p.11)

By defining density parameters in terms of the critical density

$$\rho_c(t) = \frac{3H^2(t)}{8\pi G} \quad \rho_{c,0} = \frac{3H_0^2}{8\pi G} \quad (1.11)$$

we get

$$\Omega_{r,0} = \frac{8\pi G}{3H_0^2} \rho_{r,0} \quad \Omega_{m,0} = \frac{8\pi G}{3H_0^2} \rho_{m,0} \quad \Omega_{\Lambda,0} = \frac{\Lambda c^2}{3H_0^2} \quad (1.12)$$

and we can rewrite (Eq. 1.9) as

$$H^2(a) = H_0^2 \left(\Omega_{r,0} a^{-4} + \Omega_{m,0} a^{-3} - K c^2 a^{-2} + \Omega_{\Lambda,0} \right) \quad (1.13)$$

Setting $a = 1$ and $H^2(a = 1) = H_0^2$ and solving for the K-dependent term yields

$$-\frac{K c^2}{H_0^2} := \Omega_{K,0} = 1 - \Omega_{r,0} - \Omega_{m,0} - \Omega_{\Lambda,0} \quad (1.14)$$

$\Omega_{b,0}$	$\Omega_{c,0}$	$\Omega_{m,0}$	$\Omega_{\Lambda,0}$	$\Omega_{r,0}$	H_0	t_0
0.0455	0.226	0.272	0.728	$8.5 \cdot 10^{-5}$	$70.4 \text{ km s}^{-1} \text{ Mpc}^{-1}$	13.76 Gyr

Table 1.1: The cosmological parameters (from left to right): Baryon density today, Cold dark matter density today, Matter density today, Dark energy density today, Radiation density today, Hubble constant and the age of the universe today as determined by (Komatsu et al. 2011, Tab. 1, column 2) except for $\Omega_{r,0}$, which was taken from (Bartelmann 2019, p.19). From these values one finds that matter consists of about 16.7% baryons and 83.3% CDM.

which is the definition of the (current) curvature parameter. Measurements show that the other three density parameters almost perfectly add up to one which means $\Omega_{K,0} = K = 0$ and therefore the geometry of the universe is flat.

The final Friedmann equation is

$$H^2(a) = H_0^2 \left(\Omega_{r,0} a^{-4} + \Omega_{m,0} a^{-3} + \Omega_{K,0} a^{-2} + \Omega_{\Lambda,0} \right) =: H_0^2 E^2(a) \quad (1.15)$$

where $E(a)$ is the dimensionless expansion function (Bartelmann 2019, p.16f).

The values of these parameters in the current paradigm of cosmology - the Λ CDM model - are given in (Tab. 1.1) which were determined from measurements by the WMAP² explorer by (Komatsu et al. 2011). These are also the values used in the *Magneticum*³ simulation.

The Λ CDM model has its name from the cosmological constant Λ and *cold dark matter* (CDM) which is assumed to exist.

1.2.3 Distance Measures

First we need to start with the *Hubble time* $t_H \equiv \frac{1}{H_0} = 9.78 \cdot 10^9 h^{-1} \text{ yr}$, which is the simplest appraisal for the age of the universe. From that we can calculate the *Hubble distance* $D_H \equiv \frac{c}{H_0} = 3000 h^{-1} \text{ Mpc}$, which is an approximation for the radius of the observable universe.

The simplest distance, the *proper distance* D_p , is the distance between two objects measured by a ruler at the time at which they are observed. But more importantly is the *comoving distance* δD_c , which remains constant between two objects, that are moving with the Hubble flow, i.e. they have no peculiar velocity. Therefore it is equal to the proper distance, corrected for the expansion of the universe, which is characterized by $a = (1+z)^{-1}$: $\delta D_c = \delta D_p (1+z)$. Integrating over δD_c yields the total line-of-sight comoving distance from an object at redshift z to us (at $z = 0$)

$$D_c = D_H \int_0^z \frac{dz'}{E(z')} \quad (1.16)$$

where $E(z)$ is the expansion function from (Eq. 1.15).

If we want to know the comoving distance between two objects that were observed at the same redshift in the sky (like two galaxy clusters shortly after or before they collide), we need to multiply the angle at which they are separated $\delta\theta$ by their *transverse comoving distance* D_M , which is related to the line-of-sight comoving distance. If $\Omega_K = 0$ they are the same,

²<https://map.gsfc.nasa.gov/>

³<http://magneticum.org/simulations.html>

otherwise they are related via a \sinh ($\Omega_K > 0$) or \sin ($\Omega_K < 0$) function that depend on the Ω_K .

The next important measure is the *angular diameter distance* D_A that is defined as the physical transverse size that is considered divided by its angular size (in radian). If we know this distance we can calculate the proper separation at the source with the angular separation in a telescope. It has a maximum at $z \sim 1$ and therefore an extended object at $z \sim 1$ appears larger than the same object at $z \sim 0.5$ in the sky if their physical size is the same. Without the expansion, like in everyday life, we would expect, that the closer object ($z \sim 0.5$) appears larger. This distance is related to the comoving distances as

$$D_A = \frac{D_M}{1+z} \stackrel{K=0}{=} \frac{D_c}{1+z} \quad (1.17)$$

The physical transverse size of a distance in the universe is d_{phy} whereas its comoving size is $d_{\text{com}} = (1+z) \cdot d_{\text{phy}}$. We see it over an angle $\Phi = d_{\text{com}}/D_c$. If we want to derive the physical size from the observed angle we need to rewrite it as $\Phi = d_{\text{phy}}(1+z)/D_c \equiv d_{\text{phy}}/D_A$ (Hu 2021). We see that the angular diameter distance is the comoving distance divided by $(1+z)$ because the physical distance perpendicular to the line of sight is also effected by the expansion of the universe.

The last distance measure we want to discuss is the *luminosity distance* D_L . It is defined by the bolometric flux S and luminosity L as follows:

$$D_L \equiv \sqrt{\frac{L}{4\pi S}} \quad (1.18)$$

It is also related to the other distances by

$$D_L = (1+z)D_M = (1+z)^2 D_A \stackrel{K=0}{=} (1+z)D_c \quad (1.19)$$

This is because the flux has to be corrected two times with $(1+z)^{-1}$. Once because of the energy loss of the photons due to the cosmological redshift and a second time because the photon emitting source is moving away from us at a relativistic speed and therefore its time is dilated to ours. Therefore the photons emitted per time unit are more than the photons we receive per time unit.

Because redshift is related to the scale factor, which describes the expansion of the universe over time, it can be related to a time measure. The time an observer on earth looks back in time when he is looking at a far away object in an expanding universe is called the *lookback time* t_L . It is given by (Hogg 1999)

$$t_L = t_H \int_0^z \frac{dz'}{(1+z')E(z')} \quad (1.20)$$

1.3 Dynamics of Galaxy Clusters

1.3.1 Formation of Galaxy Clusters

Galaxy clusters form in an hierarchical chain of accretion of subsystems and mergers governed by DM, as DM dominates the gravitational field. Therefore its properties are only dependent on the cosmological initial conditions in an expanding universe. For example, the temperature

of the ICM increases through adiabatic compression and shocks, that are produced by infalling substructures, before the gas settles into a hydrostatic equilibrium (Kravtsov and Borgani 2012, p. 4).

As a measure of structure formation the *density contrast* field $\delta(\mathbf{x}) = (\rho(\mathbf{x}) - \bar{\rho}_m)/\bar{\rho}_m$, where $\bar{\rho}_m$ is the mean mass density of the universe, can be used. An overdensity ($\delta(\mathbf{x}) > 0$) in this field will form an object via gravitational collapse, that will take part in the formation of a galaxy cluster later. The initial conditions of this field are assumed to be a homogeneous and isotropic Gaussian random field (Kravtsov and Borgani 2012, p. 10).

A collapse like this can be described by the *spherical collapse model*, where the evolution of a spherically-symmetric density fluctuation with the initial parameters of physical radius R_i , amplitude $\delta_i > 0$ and mass $M = 4/3\pi(1 + \delta_i)\bar{\rho}R_i^3$, where $\bar{\rho}$ is the initial mean density of the universe, is investigated. Because of its one-dimensionality only the radius $R(t)$ needs to be considered. After an initial increase of the radius and a turnaround at $R_{ta} = R(t_{ta})$ it decreases and reaches the *virial radius* $R_{vir} = R(t_{vir})$, which physically is the radius within which the gas satisfies the *virial theorem* (Kravtsov and Borgani 2012, p. 12) $\langle T \rangle_t = -1/2\langle V \rangle_t$, where T is the total kinetic energy and V is the total potential energy (Bartelmann 2015, p.118).

For $\Omega_\Lambda = 0$ these two radii satisfy $R_{vir} = R_{ta}/2$ and the respective times are $t_{vir} = 2t_{ta}$. Because the overdensity collapses during the time interval $t_{vir} - t_{ta}$ this interval is equal to the free fall time of a uniform sphere:

$$t_{vir} - t_{ta} = t_{ta} = t_{ff} = \sqrt{3\pi/(32G\rho_{ta})} \iff \rho_{ta} = 3\pi/(32Gt_{ta}^2) \quad (1.21)$$

And because $\rho \propto R^{-3}$ we get $\rho_{vir} = 8\rho_{ta} = 3\pi/(4Gt_{ta}^2) = 3\pi/(Gt_{vir}^2)$. The mean mass density in a Einstein-de Sitter Universe ($\Omega_m = 1, \Omega_\Lambda = 0$) evolves as $\bar{\rho}_m(t) = 1/(6\pi Gt^2)$ and therefore the density contrast within a sphere of radius R_{vir} is

$$\Delta_{vir} = \frac{\rho_{vir}}{\bar{\rho}_m(t_{vir})} = 18\pi^2 \approx 180 \quad (1.22)$$

Similar estimates of ρ_{vir} and $\bar{\rho}_m(t_{vir})$ can be made for the Λ CDM model. For values given in (Tab. 1.1) at $z = 0$ this yields $\Delta_{vir} \approx 358$ (Kravtsov and Borgani 2012, p.12).

Even though the spherical density model presents approximations for the virialization time scale and the virial density contrast, it does not describe real collapses of density peaks. As seen in numerical simulations, the boundaries of a cluster are not sharp and therefore different parts of a overdensity collapse at different times and therefore t_{vir} is also not sharp.

Also the density field contains fluctuations within one peak and therefore collapses arise on all spatial scales. At high redshifts many small-mass collapsed objects merge to build up larger substructures until they are virialized and near the center of the overall density peak. Nonlinear effects and mergers lead to relaxation and energy and mass exchange over all these scales (Kravtsov and Borgani 2012).

1.3.2 Mass and Radius Definitions

For the above defined *virial radius* R_{vir} one can define the *virial mass* M_{vir} , which is the mass encompassed within a sphere with radius R_{vir} : $M_{vir} = (4\pi/3)\rho_{vir}R_{vir}^3$. Following the discussion of the density contrast above it can be approximated as a *spherical overdensity mass* (SO mass). For a given cluster the center needs to be chosen as e.g. the density peak, the potential minimum, the position of the most bound particle or the center of mass. The

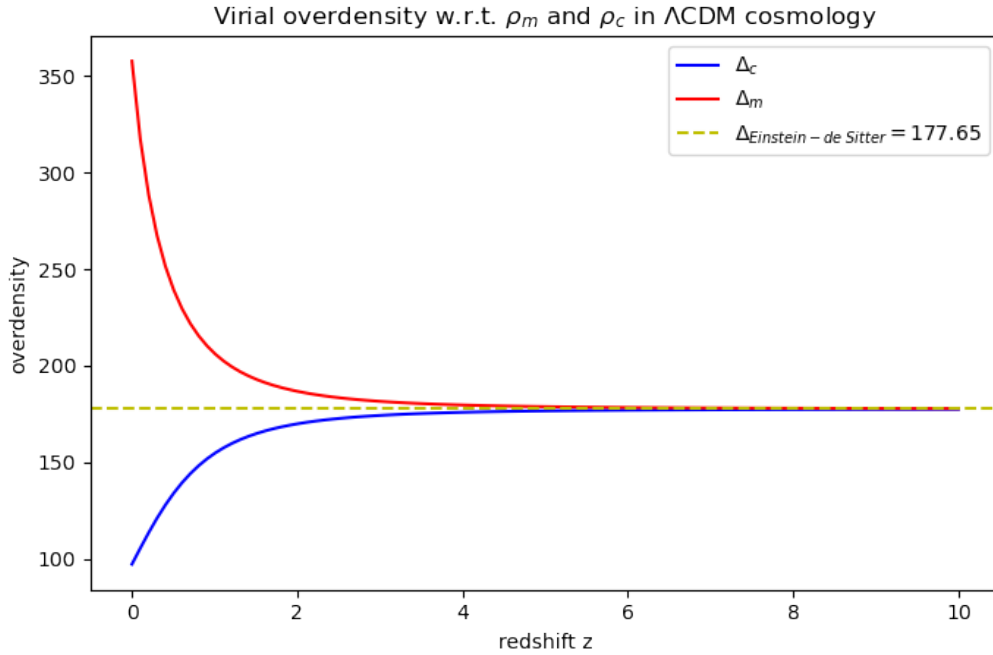


Figure 1.2: Virial overdensities Δ_m and Δ_c for ρ_m and ρ_c as a function of the redshift z in the Λ CDM-model.

SO mass $m_{\Delta_{\text{ref}}}$ is the mass within a sphere of radius $r_{\Delta_{\text{ref}}}$ enclosing a given density contrast Δ with respect to a reference density $\rho_{\text{ref}}(z)$:

$$m_{\Delta_{\text{ref}}} = \frac{4\pi}{3} \Delta \rho(z) r_{\Delta_{\text{ref}}}^3 \quad (1.23)$$

As a reference density the critical density $\rho_c(z)$ (Eq. 1.11) and the mean matter density $\rho_m(z)$ are in use. The density contrast for both are given by $\Delta_m = \Delta_c / \Omega_m(z)$ and $\Omega_m(z) = \Omega_{m,0}(1+z)^3 / E(z)$, where $E(z)$ is given by (Eq. 1.15) (Kravtsov and Borgani 2012). $\Delta_c = 18\pi^2 + 82x - 39x^2$ describes how the critical overdensity changes with $x = \Omega_m(z) - 1$ for $\Omega_r = 0$ (Bryan and Norman 1998). The virial overdensities Δ_m and Δ_c for ρ_m and ρ_c as a function of the redshift z in the Λ CDM-model is shown in (Fig. 1.2). The virial mass M_{vir} and radius R_{vir} are often approximated by m_{200c} and r_{200c} , because Δ_m is close to 200 for $z > 1$, where much of the structure formation takes place. Later in this work we will use the radius r_{500c} .

1.3.3 Accretion of Substructures

The collapsing density peaks discussed in (Sec. 1.3.1) are not alone in the universe but are surrounded by other peaks (Kravtsov and Borgani 2012). The tidal forces of the most massive overdensities disrupt the other peaks. The distance of disruption d can be estimated by approximating a system of close galaxy clusters as a massive body of mass M and a smaller body of mass $m \ll M$ which again is approximated by two even smaller bodies of masses $m/2$ (See. Fig. 1.3):

The attracting gravitational force between the two small spheres is

$$f_{\text{att}} = G \frac{m/2 \cdot m/2}{r^2} = \frac{Gm^2}{4r^2} \quad (1.24)$$

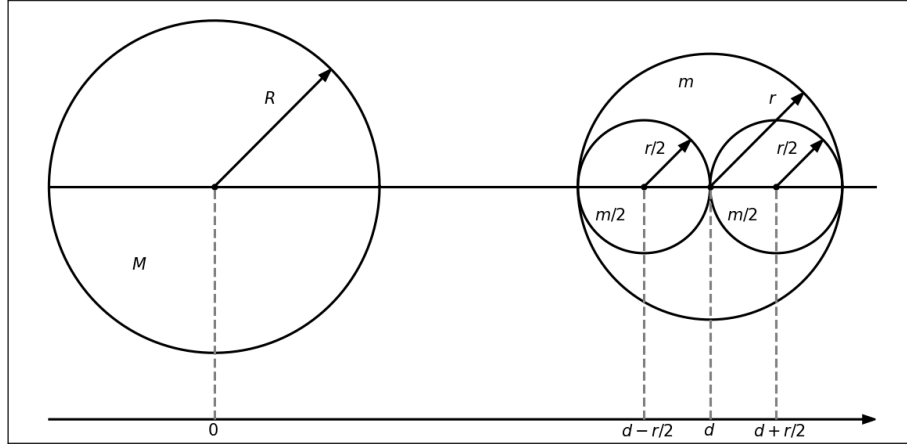


Figure 1.3: Massive body of mass M and smaller body of mass $m \ll M$ approximated as two smaller bodies of masses $m/2$ in order to estimate tidal forces.

while the gravitational force pulling them apart, is the difference in attracting gravitational forces between each of the small bodies and the massive body, which is

$$f_{\text{dis}} = G \frac{M \cdot m/2}{(d - r/2)^2} - G \frac{M \cdot m/2}{(d + r/2)^2} \approx G \frac{Mm}{d^3} r \quad (1.25)$$

where we used a Taylor expansion for the second step. Because the small body is disrupted if $f_{\text{dis}} > f_{\text{att}}$ the so called *Roche limit* can be written as

$$G \frac{Mm}{d^3} r > G \frac{m^2}{r^2} \implies \frac{d^3}{M} \propto \frac{r^3}{m} \quad (1.26)$$

where we can imagine d as the radius of a sphere around the massive body through the smaller one, M is its mass, r is the radius of the small body and m is the respective mass. As $\bar{\rho} \propto M/r^3$ (Eq. 1.26) can be rewritten in terms of the densities of these spheres: $\bar{\rho}_{\text{massive}} \propto \bar{\rho}_{\text{small}}$. If we consider d and r to be SO radii (Eq. 1.23) with the same overdensities Δ this means a galaxy or galaxy group can be disrupted after passing the point where its SO radius touches that of the galaxy cluster it falls into.

The tidally stripped matter is formed into massive cosmological filaments that reach between the most massive galaxy clusters along which most of the accretion of matter onto clusters happens (Kravtsov and Borgani 2012).

1.3.4 Mergers

The accretion discussed in the section above consists of inter cluster gas, individual galaxies and galaxy groups onto a large galaxy cluster. If two galaxy clusters collide with each other the system is called a *merger*. If the masses of both components are comparable it is called a *major merger*, otherwise one would speak of a *minor merger*. (Markevitch and Vikhlinin 2007, p.48)

In any of these events the gas inside of the infalling or colliding structure (inter stellar medium (ISM) for individual galaxies, ICM for galaxy cluster) experiences *ram pressure* given by

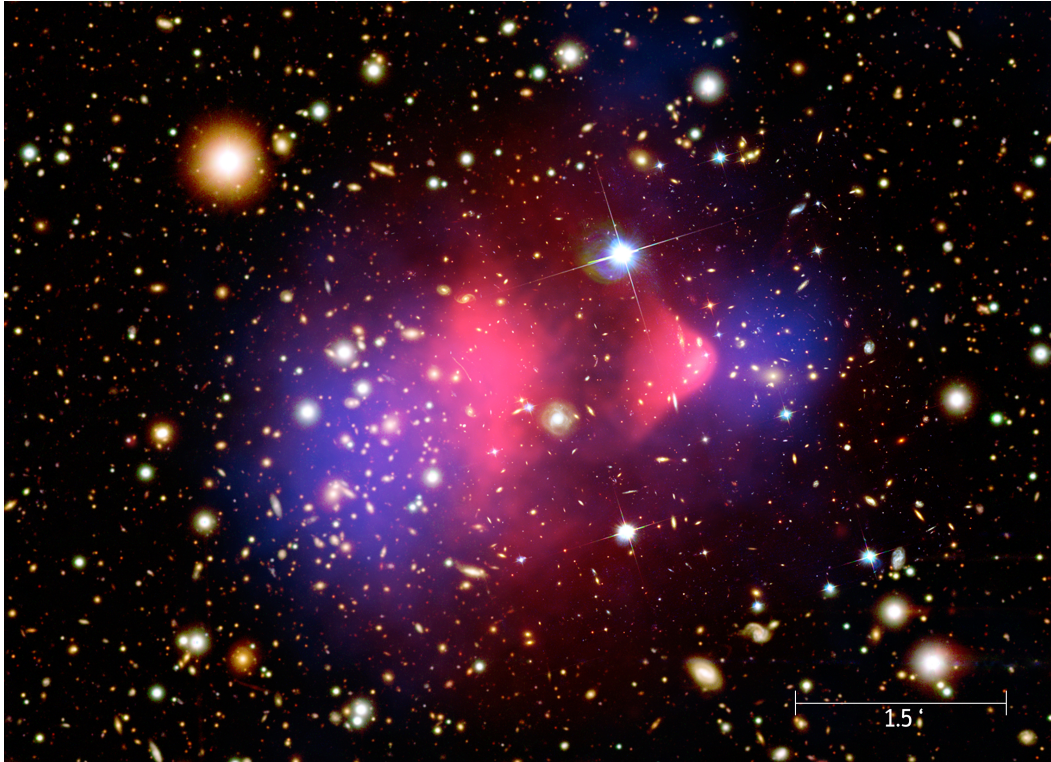


Figure 1.4: Composite image of the Bullet Cluster (1E 0657-56). Optical background image from HST and Magellan; *Chandra* X-ray Observatory image in pink; Projected total mass map obtained from weak lensing in blue (Clowe et al. 2006) (Image created by the *Chandra* press group).

$$P_{\text{ram}} = \rho v^2 \quad (1.27)$$

where ρ is the density of the ICM (of the main cluster) and v is the velocity of a substructure relative to said ICM (ZuHone and Su 2022, p.4). This effect is responsible for a variety of phenomena in galaxy clusters, such as tails of ram-pressure stripped gas behind infalling galaxies ("jellyfish galaxies") (ZuHone and Su 2022, p.14f), cold fronts (ZuHone and Su 2022, Markevitch and Vikhlinin 2007) and shocks that we discuss below, (Markevitch and Vikhlinin 2007). The most prominent example for ram-pressure stripping is the Bullet Cluster as seen in (Fig. 1.4). In this composite image the blue regions correspond to the total mass map obtained by weak lensing and the pink regions show the hot ICM gas (Clowe et al. 2006). One can clearly see, that because ram-pressure only affects the gas, while the galaxies and the mass dominating dark matter pass each other collisionless, the ICM gets pushed behind their respective galaxies and dark matter, creating a gas bridge.

In (Fig. 1.4) one can also see a surface brightness edge in front of the *bullet*-like substructure at the western side. This is a surface of discontinuity. They occur in two different forms in galaxy clusters: Cold fronts and shock fronts. This particular one visible in (Fig. 1.4) is a cold front albeit a shock front is just 100 kpc in front of it (ZuHone and Su 2022).

Cold fronts are *contact discontinuities* (ZuHone and Su 2022), which are a special case of a tangential discontinuity, i.e. pressure and velocities perpendicular to the front are continuous. In a contact discontinuity on top of that, also the tangential velocities are continuous. Only the density can remain discontinuous, but with it also other thermodynamical quantities e.g. temperature (Landau and Lifshitz 1959, §84). Even though cold fronts are always called contact discontinuities in the literature they often have discontinuous tangential velocities (Markevitch and Vikhlinin 2007, p.12). The most striking difference to shock fronts is that,

as the name already implies, the gas behind the front is colder than the ICM in front of it. This is the case because every cold front has its origin in the cold, low entropy gas of a cluster core. These merger cold fronts are most often observed on the inbound part of their trajectory or close to the core, when ram pressure reaches its maximum and the hot ICM of the infalling substructure is pushed behind its cold core, where the temperature and density jump is most pronounced. The contradiction that the pressure is continuous but the densities and temperature are not can be resolved by ram pressure: $p_{thermal,cool} = p_{thermal,ICM} + p_{ram}$. If the cold substructure survives the core passage and enters the lower density region behind the center, ram pressure drops and the "slingshot" stage of the cold fronts sets in. More details on this stage and cold fronts in general can be found in (Markevitch and Vikhlinin 2007) and (ZuHone and Su 2022).

If a merger happens supersonically a cold front can form as well, but now a shock front will propagate in front of it. Its velocity is often encoded by the *Mach number* $\mathbf{M} \equiv v/c_s$, where v is the flow velocity and c_s the sound speed of the medium, given by

$$c_s = \sqrt{\frac{\gamma k_B T}{\mu m_p}} \quad (1.28)$$

where T is the thermal temperature, $\gamma = 5/3$ is adiabatic index of a monatomic gas, k_B the Boltzmann constant and $\mu \approx 0.6$ the mean molecular weight (ZuHone and Su 2022). For merger shocks $M \lesssim 3$, because the temperature of the ICM of the main cluster and therefore its sound speed and the velocity of infalling substructures reflect the same gravitational potential of the main cluster (Markevitch and Vikhlinin 2007). As mergers involve the conversion of up to $\sim 10^{65}$ erg of gravitational potential energy into kinetic energy of dark matter, ICM and galaxies as well as into the thermal and magnetic energy of the ICM, these shock fronts are the primary heating source for the hot cluster gas (ZuHone and Su 2022). Unlike cold fronts shock fronts can have pressure and perpendicular velocity discontinuities. Only the tangential velocities should be continuous (Landau and Lifshitz 1959, §84). Also their temperature jump has the opposite sign of the jump in cold fronts, as the hotter gas is the shocked gas behind the shock front. We know from simulations it is unlikely that they form during the inbound segment of the subcluster's trajectory as they have to climb up the density gradient of the main cluster. Which makes them hard to find, because once they left the center the X-ray brightness becomes too low for us to observe them and they need to propagate nearly in the plane of the sky. Other origins of shock fronts are AGN bubbles in clusters center or *accretion shocks* at the outskirts of clusters. These are hardly observable, because of the bubbles low Mach number $\mathbf{M} \sim 1$ or because they only occur in low X-ray brightness regions, like accretion shocks, where the Mach number would be high enough $\mathbf{M} \sim 10 - 100$ (Markevitch and Vikhlinin 2007).

1.3.5 Rankine-Hugoniot Jump Conditions

In order to examine shock fronts the discontinuities in the fluid properties are described by the the *Rankine-Hugoniot jump conditions*. For a polytropic ideal gas, i.e. the equation of state is $pV = p/\rho = RT/\mu$ with a heat function $w = C_p T = \frac{\gamma pV}{\gamma-1} = \frac{c^2}{\gamma-1}$ the jump ratios can be derived from the conservation of mass, energy and momentum (Landau and Lifshitz 1959, §84)

$$\rho_1 v_{1,x} = \rho_2 v_{2,x} \quad (1.29)$$

$$\rho_1 v_{1,x} \left(\frac{1}{2} v_1^2 + w_1 \right) = \rho_2 v_{2,x} \left(\frac{1}{2} v_2^2 + w_2 \right) \quad (1.30)$$

$$p_1 + \rho_1 v_{1,x}^2 = p_2 + \rho_2 v_{2,x}^2 \quad (1.31)$$

where we omitted the conservation of tangential velocities, because they should be continuous in a shock front and a contact discontinuity. The jump ratios for density, pressure and temperature as a function of the Mach number \mathbf{M} are

$$\frac{\rho_2}{\rho_1} = \frac{v_1}{v_2} = \frac{(\gamma + 1)\mathbf{M}_1^2}{(\gamma - 1)\mathbf{M}_1^2 + 2} \quad (1.32)$$

$$\frac{p_2}{p_1} = \frac{2\gamma\mathbf{M}_1^2}{\gamma + 1} - \frac{\gamma - 1}{\gamma + 1} \quad (1.33)$$

$$\frac{T_2}{T_1} = \frac{(2\gamma\mathbf{M}_1^2 - (\gamma - 1))((\gamma - 1)\mathbf{M}_1^2 + 2)}{(\gamma + 1)^2\mathbf{M}_1^2} \quad (1.34)$$

In all these equations the subscript 1 corresponds to the gas in front of the shock (upstream) and 2 corresponds to the shocked gas behind the shock (downstream). A derivation following (Landau and Lifshitz 1959, §89) can be found in (App. A). (Fig. 1.5) shows these jump ratios as a function of the Mach number for $\gamma = 5/3$ and $\gamma = 4/3$, which represents relativistic gas. For large $\mathbf{M} \gg 1$ the density jump ratio approaches 4 while the temperature and pressure jump ratios can grow infinitely with the Mach number, but for relativistic gas they grow slower. Therefore the velocity jump ratio (which is the reciprocal of the density jump ratio) approaches 1/4 and the jump ratio for the kinetic energy $E_{kin,2}/E_{kin,1} = \rho_2 v_2^2 / \rho_1 v_1^2$ approaches the same value. Typical values for $\gamma = 5/3$ are $\rho_2/\rho_1(\mathbf{M} = 3) = 3$ and $\rho_2/\rho_1(\mathbf{M} = 10) = 3.9$.

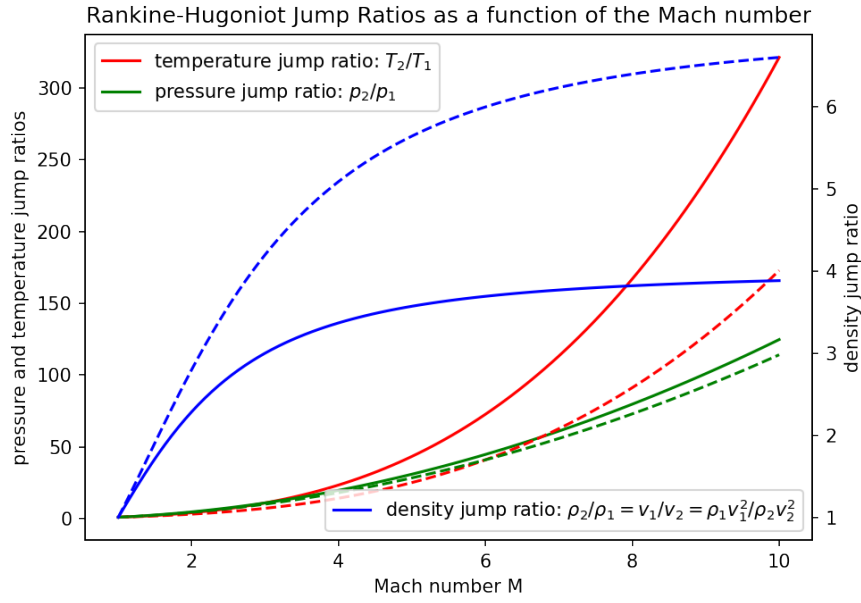


Figure 1.5: The Rankine-Hugoniot jump ratios for density, pressure and temperature. For large $\mathbf{M} \gg 1$ the density jump ratio approaches 4 while the temperature and pressure jump ratios can grow infinitely with the Mach number; The dashed lines represent relativistic gas where $\gamma = 4/3$.

1.4 Properties of the ICM

It was observed from X-ray observations, that galaxy clusters are filled with the so called intracluster medium (ICM), a hot and diffuse plasma at temperatures of $T_e \sim 10^7 - 10^8$ K (kinetic electron temperature) and densities between $n \sim 10^{-2} \text{ cm}^{-3}$ at the center and $\sim 10^{-4} \text{ cm}^{-3}$ in the peripheral regions. It consists of electrons and ions, which are mostly protons, but there is a trace of heavier, ionized elements, like iron, at abundances similar to the content in the sun. A gas like that mainly emits radiation due to the process of thermal bremsstrahlung (free-free) emission. At temperatures and densities which are at play in galaxy clusters, this results in X-ray emission (Markevitch and Vikhlinin 2007, p. 3).

In the following section a few different densities will be used. Number densities are denoted by n and have units cm^{-3} and mass densities are denoted by ρ and have units $g \text{ cm}^{-3}$. We will distinguish between electron and proton densities with the subscripts e and p respectively. Combining both yields the gas density with the subscript g . In a plasma with conditions like the ICM electron and proton densities are connected by (Sarazin 1986)

$$n_e = 1.21n_p \quad (1.35)$$

and the number and mass density is connected via

$$n = \frac{\rho}{\mu m_p} \quad (1.36)$$

where μ is the mean molecular weight, that can be calculated with

$$\mu = \left(\sum_i \frac{X_i(1 + Z_i)}{A_i} \right)^{-1} \quad (1.37)$$

where X_i is the mass fraction, Z_i the charge number and A_i the mass number of the nucleus i . In the ICM the main components are hydrogen and helium with $X_H = 0.75$, $X_{He} = 0.25$, $Z_H = 1$, $Z_{He} = 2$ and $A_H = 1$, $A_{He} = 4$ which yields $\mu \approx 0.6$ (Kippenhahn and Weigert 1990, p.103).

1.4.1 Isothermal Beta Model

In general the ICM can be described as a fluid, because the *collision time scales* for ions and electrons are much shorter than any *dynamical time scales* or temperature changing time scales. A sound wave will take no significant fraction of the age of the cluster to pass it and also the *cooling time* of the thermal bremsstrahlung is greater than the *sound crossing time*, which makes hydrostatic equilibrium possible. The simplest form of a hydrostatic gas distribution is a isothermal one (Sarazin 1986, p.78).

The gas distribution in the isothermal β -model can be described by

$$\frac{\rho_k(r)}{\rho_{k,0}} = \frac{n_k(r)}{n_{k,0}} = \left(1 + \left(\frac{r}{r_c}\right)^2\right)^{-3\beta/2} \quad (1.38)$$

where $k = \{g, e, p\}$ and the subscript 0 indicates the density in the core, r_c is the core radius and β is given by

$$\beta = \frac{\mu m_p \sigma_r^2}{k_B T_g} \quad (1.39)$$

where σ_r is the line-of-sight velocity dispersion. From this model many useful parameters like the total gas mass and the emission integral can be found. (Sarazin 1986, p. 16 and p. 78) (Fig. 1.6) shows the total mass and the total gas mass given by this model and (Fig. 1.7) shows the β -model applied to the Bullet Cluster.

1.4.2 Time Scales and Length Scales

To get a good intuition how processes work in a plasma and to get a quick overview time and length scales can be used, similar to the justification of hydrostatic equilibrium in the previous section.

As particle interaction in the ICM are mediated by the electric force (neglecting magnetic fields), the most basic length scale is the *mean free path*, which is the distance a particle can travel between two so called *Coulomb collisions* (distant or nearby).

$$\lambda_{\text{mfp}} = \frac{3^{3/2} (k_B T)^2}{4\pi^{1/2} n q^4 \ln(\Lambda)} \quad (1.40)$$

where T is either the electron temperature T_e or the ion temperature T_i , q and n are the respective charge and density and Λ is the ratio of largest to smallest impact parameter. $\ln(\Lambda)$ is called the *Coulomb logarithm* and has typical values of $\sim 30 - 40$. Below this length scale hot ionized plasma can not be approximated as a fluid and gradients in the fluid properties are smeared out by particle diffusion (ZuHone and Su 2022, p. 3). The corresponding time scale is the *(self) collision time*:

$$t_{\text{coll}} \equiv \frac{\lambda_{\text{mfp}}}{\langle v \rangle_{\text{rms}}} = \frac{3m^{1/2} (k_B T)^{3/2}}{4\pi^{1/2} n q^4 \ln(\Lambda)} \quad (1.41)$$

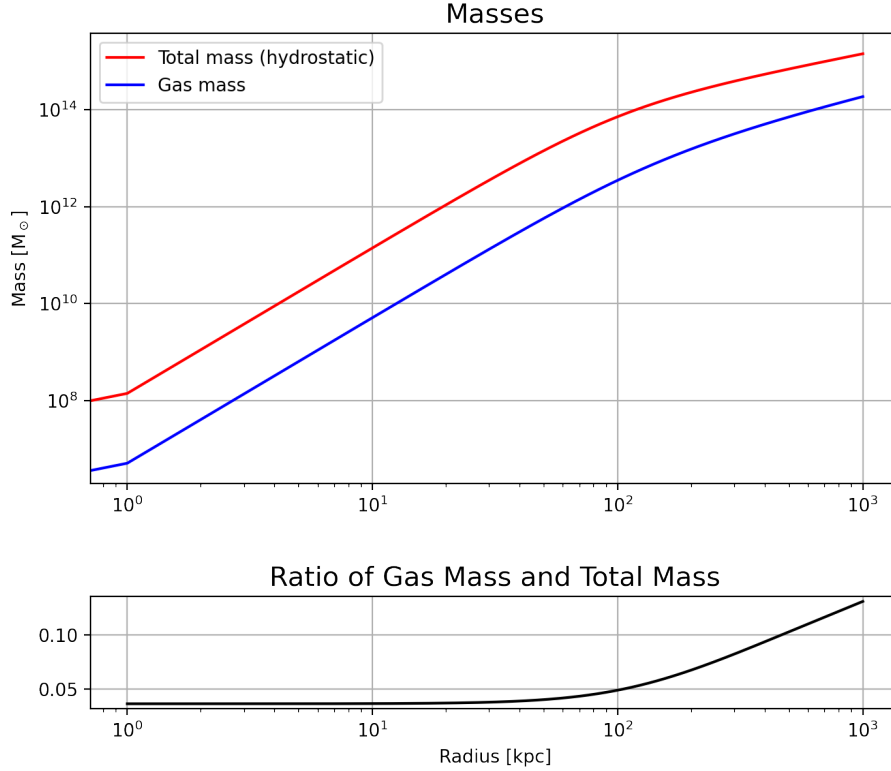


Figure 1.6: Top: Total hydrostatic mass and total gas mass profiles as given by the isothermal β -model (Eq. 1.38); Bottom: Ratio of Gas Mass and Total Mass. It suggests, that the fraction of gas is higher in the outskirts, i.e. there is more DM in the core. The typical values used are $n_g = 0.05 \text{ cm}^{-3}$, $T_g = 4 \text{ keV}$, $r_c = 100 \text{ kpc}$ and $\beta = 0.6$.

where $\langle v \rangle_{\text{rms}} = \sqrt{3k_B T/m}$ is the root mean square velocity and the other quantities are the same as described for the *mean free path* (Spitzer 1962 p.78ff, Sarazin 1986, p.72f). Generally one finds

$$t_{\text{coll}}(p, p) \approx (m_p/m_e)^{1/2} t_{\text{coll}}(e, e) \quad t_{\text{coll}}(p, e) \approx (m_p/m_e) t_{\text{coll}}(e, e) \quad (1.42)$$

This is also the time scale at which a non-Maxwellian particle distribution will relax to a Maxwellian distribution via elastic collisions. This equilibration will be reached by electrons on time scales set by (Eq. 1.41) (with values for electrons) and according to the left hand side of (Eq. 1.42) protons need roughly 43 times longer. To reach equipartition $T_e = T_p$ the time scale is about 1870 times longer, as seen in the right hand side of (Eq. 1.42). The longest time scale will be $t_{\text{coll}}(p, e) \sim 6 \cdot 10^8 \text{ yr}$ and since this is shorter than the age of the cluster it is safe to assume $T_e = T_i = T_g$ in most parts of the galaxy cluster.

Because the factor $m^{1/2}$ in the *collision time* is compensated by a factor of $m^{-1/2}$ in the root mean square velocity $\langle v \rangle_{\text{rms}}$, one can see, that the *mean free path* of electrons and protons is the same (Sarazin 1986, p.72f, Spitzer 1962, p.80f).

Another important time scale is the *cooling time*. Because the primary cooling mechanism of the ICM is thermal bremsstrahlung, the cooling time is given by the rate at which the thermal energy is radiated away by this process. If the gas cools isobarically the time scale is given by

$$t_{\text{cool}} = 8.5 \cdot 10^{10} \text{ yr} \left(\frac{n_p}{10^{-3} \text{ cm}^{-3}} \right)^{-1} \left(\frac{T_g}{10^8 \text{ K}} \right)^{1/2} \quad (1.43)$$

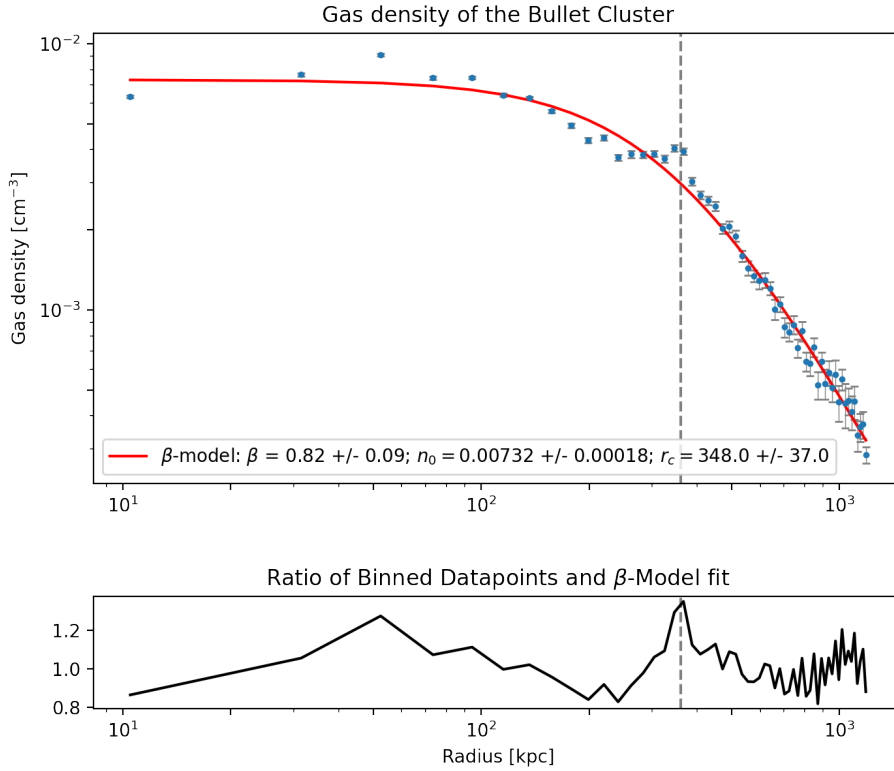


Figure 1.7: Top: Blue dots are radial binned data points taken from the ACCEPT Archive (Cavagnolo et al. 2009); The red line is a least-square fit to the β -model (Eq. 1.38); The dashed line is at the radius 340 kpc which is roughly where the substructure is located; Bottom: Ratio of radial binned data points and the β -model fit showing a peak where the substructure is located.

where n_p is the proton density and T_g the gas temperature. As discussed in the last section this time scale is longer than the *sound crossing time* and therefore hydrostatic equilibrium is justified (Sarazin 1986, p. 69). This also shows, that radiative cooling of the ICM is inefficient and can be neglected (almost everywhere), because this time scale is longer than the average cluster age (Markevitch and Vikhlinin 2007, p. 3).

Further we discuss the *sound crossing time* and the *dynamical time scale*. The former is the time a sound wave in the ICM takes to cross a cluster and the latter is equal to half the orbital period of a (infalling) substructure moving with keplerian speed $v_K = \sqrt{GM(< R)/R}$. They are therefore given by

$$t_{\text{sound}} = \frac{2R}{c_s} \quad t_{\text{dyn}} = \frac{\pi R}{v_K} \quad (1.44)$$

where R is the radius of the cluster and the sound speed c_s is given by (Eq. 1.28). Therefore the *sound crossing time* can be expressed by

$$t_{\text{sound}} = 6.6 \cdot 10^8 \text{yr} \left(\frac{T_g}{10^8 \text{K}} \right)^{-1/2} \left(\frac{2R}{\text{Mpc}} \right) \quad (1.45)$$

where the variable are the same as above (Sarazin 1986, p.77). One implication of this time scale was already discusses above but one can also come to the conclusion that because it is relatively short the cluster would lose a lot of gas and therefore there needs to be a constant flow of gas onto the cluster (Sarazin 1986, p. 83).

The ICM is an example of a so-called *high β_{mag} -plasma*. Here the parameter β_{mag} is not the same as used in the isothermal beta model, but is given by

$$\beta_{\text{mag}} \equiv \frac{p_{\text{gas}}}{p_{\text{mag}}} = \frac{8\pi p_{\text{gas}}}{B^2} \quad (1.46)$$

where B is the magnetic field strength, $p_{\text{gas}} = n_g k_B T_g$ is the thermal pressure of the gas and $p_{\text{mag}} = \frac{B^2}{8\pi}$ is called the magnetic pressure. In a *high β_{mag} -plasma* the thermal pressure dominates the magnetic pressure $\beta_{\text{mag}} \gg 1$ (Kunz et al. 2019).

Now we can turn to the *electric* and *magnetic* length scales. First is the *Debye length* (or *Debye shielding distance*). A charge is shielded by particles of opposite sign at distances greater than λ_{Debye} . It is given by

$$\lambda_{\text{Debye}} = \left(\frac{k_B T}{4\pi n_e e^2} \right)^{1/2} \quad (1.47)$$

where T_g is the gas temperature and n_e is the electron density (Spitzer 1962, p.17). The corresponding *Debye time* is the time it takes the particle to equalize a charge difference. Therefore the Debye scales are not physical but encode a *collective behaviour* of the plasma. Also the above interpretations are only valid if there are enough particles N_{Debye} inside the *Debye sphere*:

$$N_{\text{Debye}} = n_g \frac{4}{3} \pi \lambda_{\text{Debye}}^3 \quad (1.48)$$

For a fully ionized gas to be called a plasma it is required that $N_{\text{Debye}} \gg 1$ in addition to $\lambda_{\text{Debye}} \ll L$, where L are the dimensions of the system (Chen 2016, p.11).

Second is the *Lamor radius* (or *radius of gyration*). If the electric field \mathbf{E} vanishes, the acceleration of a moving, charged particle in a magnetic field \mathbf{B} is always perpendicular to the velocity and a gyrating motion of the particle will occur. The radius of this gyration is the *Lamor radius* given by

$$\lambda_{\text{Lamor}} = \frac{mv_{\perp}}{qB} = \frac{mcv_{\perp}}{eB} \quad (1.49)$$

where m is the mass of the particle, c is the speed of light and v_{\perp} is the component of the particles velocity perpendicular to the magnetic field B . The angular frequency of the gyration is given by the *cyclotron frequency* $\omega_c = qB/m = eB/mc$. The velocity component parallel to the magnetic field won't effect the motion perpendicular to the field and the combined motion will be a helix (Spitzer 1962, p. 2). By comparing this length scale to the *mean free path* and finding, that it is much smaller, one can conclude that the motion perpendicular to the magnetic field caused by other effects is suppressed if a magnetic field is present. Therefore thermal conduction and viscosity in the ICM are supposed to be anisotropic with respect to the magnetic field (ZuHone and Su 2022, p.20).

Typical values for all these scales can be found in (Tab. 1.2) and how they change with the radius of a galaxy cluster is shown in Fig. 1.8.

1.4.3 Entropy in the ICM

When analysing the thermodynamical properties of the ICM entropy is often considered. The thermodynamical entropy of an ideal gas is given by the Sackur-Tetrode equation (Schollwöck

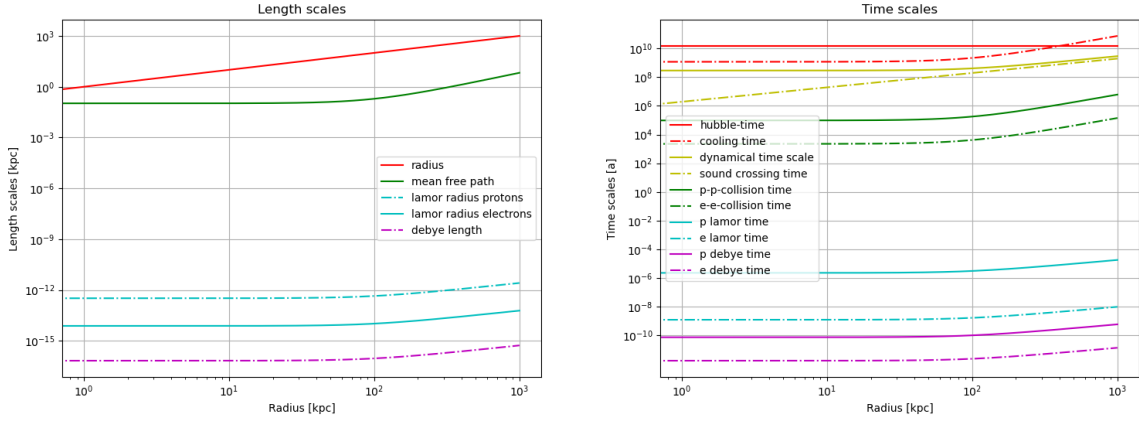


Figure 1.8: Length (left panel) and Time scales (right panel) as predicted by the above equations and the isothermal beta model. The typical values used are $n_{g,0} = 0.05 \text{ cm}^{-3}$, $T_g = 4\text{keV}$, $r_c = 100\text{kpc}$ and $\beta = 0.6$.

	radius	density	temperature	β_{mag}	B	N_{Debye}
electrons	300 kpc	0.006 cm^{-3}	4 keV	100	$3 \mu\text{G}$	$5.5 \cdot 10^{15}$
protons						

	t_{cool}	t_{dyn}	t_{sound}	t_{coll}	t_{Lamor}	t_{Debye}	λ_{mfp}	λ_{Lamor}	λ_{Debye}
electrons	9 Gyr	1 Gyr	1 Gyr	20 kyr	0.1 s	0.2 ms	1 kpc	700 km	6 km
protons				760 kyr	3.4 min	7 ms		29000 km	

Table 1.2: Time and length scales that are of interest in the ICM for electrons and protons; The last two time scales were calculated as $t_{\text{Debye}} = \lambda_{\text{Debye}}/v$ and $t_{\text{Lamor}} = 2\pi\lambda_{\text{Lamor}}/v$, where $v = \sqrt{2k_B T/m}$ is the most probable velocity in a Maxwellian velocity distribution.

2021, p.540):

$$S = Nk_B \left(\ln \left[\frac{V}{N} \left(\frac{E}{N} \right)^{3/2} \right] \right) + \frac{3}{2} \ln \left(\frac{4\pi m}{3h^2} \right) + \frac{5}{2} \quad (1.50)$$

The *specific entropy* is $s = S/N$. Inserting the definition of the number density $n = N/V$, the equation of state for ideal gas $E = \frac{3}{2}Nk_B T \iff E/N \propto T$ and ignoring all the constants yields

$$s \sim \ln \left(\frac{T^{3/2}}{n} \right) \quad (1.51)$$

Multiplying with $2/3$ gives $\frac{2}{3}S \sim \ln(T/n^{2/3})$ and finally we end up at

$$s \sim \frac{3}{2} \ln \left(\frac{T}{n^{2/3}} \right) \equiv \frac{3}{2} \ln(K) \quad (1.52)$$

In the context of galaxy clusters the logarithm is ignored as well and the term K itself is called entropy or specific entropy (Dolag et al. 2004,p.3). Its units usually are keV cm^2 . Calculating this from gas density and temperature can be done with

$$K = \frac{k_B T}{(\rho/\mu m_p)^{2/3}} \quad (1.53)$$

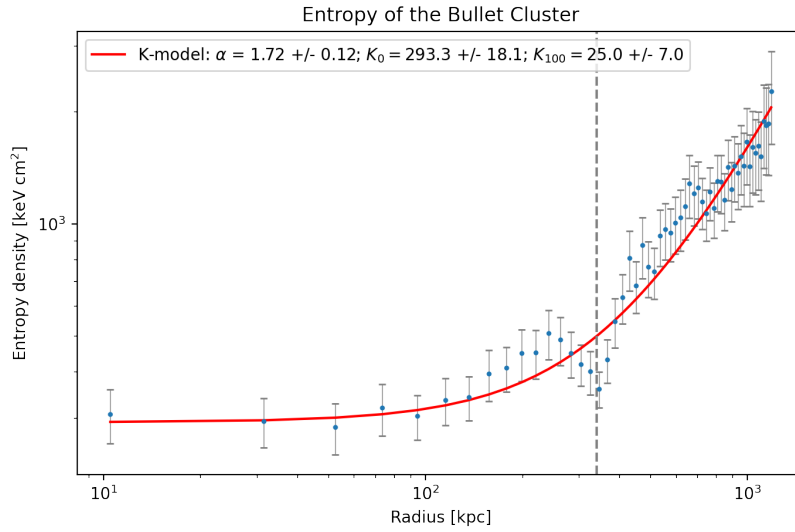


Figure 1.9: The blue dots are radial binned data points taken from the ACCEPT Archive (Cavagnolo et al. 2009); The red line is a least-square fit to the K -model (Eq. 1.54); The dashed line is at the radius 340 kpc which is roughly where the substructure is located.

This is convenient because temperature and density are observable quantities. In galaxy clusters the core is a low-entropy region, whereas the gas in the outskirts has a higher entropy (Markevitch and Vikhlinin 2007, p.8).

A model that can be used to fit entropy profiles is given by

$$K(r) = K_0 + K_{100} \left(\frac{r}{100 \text{kpc}} \right)^\alpha \quad (1.54)$$

where K_0 is called core entropy and K_{100} is a normalization for entropy at 100 kpc (Cavagnolo et al. 2009). The radial entropy profile of the Bullet Cluster can be seen in (Fig. 1.9). It is increasing from a low entropy region in the center of the main cluster and continually increases outwards with a small dip at about $r = 340 \text{kpc}$, which represents the outgoing substructure. This means the small gas cloud used to be the center of a galaxy cluster and therefore has low entropy.

1.4.4 Metallicity in the ICM

In astrophysics all elements heavier than hydrogen and helium are called *metals*, simply because the first two elements are most abundant in the universe and metals are just traces in most astrophysical systems (Schneider 2006, p.46). The *metallicity* Z is a measure for how common metals are within a gas. It is defined as the mass of an element divided by the mass of hydrogen within a system

$$Z_j = \frac{m_j}{m_H} \quad (1.55)$$

The total metallicity is the sum over all metals excluding hydrogen and helium:

$$Z = \sum_j Z_j \quad (1.56)$$

Often this value is given w.r.t. the abundance of metals in the sun, therefore given by

$$Z_{rel} = \frac{Z}{Z_{\odot}} \quad (1.57)$$

Hydrogen and helium were produced shortly after the big bang in what is called primordial nucleosynthesis. This produced hydrogen and helium in mass fraction of approximately 75% and 25% and ^2H , ^3H and Li in trace amounts (Bartelmann 2019). As the universe evolved heavier metals were produced within stars. It is currently considered that there are three main channels in which metals make their way from stars into the interstellar gas: Type II Supernovae (SNII), Type Ia Supernovae (SNIa), and asymptotic giant branch stars (AGBs) (Dolag et al. 2017). A so called core collapse supernovae (SNII) occur if massive ($> 8M_{\odot}$) stars reach the end of their life. Consecutive fusion of hydrogen to heavier elements up to iron produced a *onion-like* shell structure with an iron core after roughly 10^7 years. Under the extreme conditions in the core photodisintegration of iron and electron capture by protons lead to the core losing its pressure support and to the begin of a collapse. This collapse will eventually be stopped by the Pauli exclusion principle and the core will rebound sending a shock wave outwards. Supported by neutrino energy this shock wave then leads to the rapid expansion of the stars material into the interstellar regime. Thermonuclear supernovae of type Ia are the result of the accretion of matter of a gas giant onto a white dwarf within a binary system. If the white dwarf reaches a certain mass threshold nuclear reactions begin in the core, which will destroy the star. AGB stars develop superwinds in the late stages of their evolution, which expel matter at a rapid rate. This process also enriches the interstellar medium (Carroll and Ostlie 2017, p.513, p.588f, p. 751f). These channels are implemented in most models of chemical enrichment in simulations.

It has to be noticed here, that solar metallicity is not well defined. There are different methods to determine the abundances of elements in the solar system. Spectroscopy of the sun can be performed, but also the planets or asteroids (large rocks located in the asteroid belt) can be considered. The first method can only examine the solar photosphere and its corona, whereas value for the latter are determined by analyzing meteorites (asteroids that fell down on earth). Depending on which method was used authors get different results. For this work data from (Anders and Grevesse 1989)⁴ was used. The authors combined meteorite, photosphere and solar corona data.

⁴<https://heasarc.gsfc.nasa.gov/xanadu/xspec/manual/node116.html>

Chapter 2

Methodology

2.1 N-Body Simulations

The gravity dominating CDM can be described by a collisionless, non-relativistic fluid of particles of mass m , positions \mathbf{x} and momentum \mathbf{p} . Because the universe is expanding with the scale factor $a = (1+z)^{-1}$ (Eq. 1.4), \mathbf{x} is the comoving position (Eq. 1.16) and the phase-space distribution function $f(\mathbf{x}, \mathbf{p}, t)$ is described by the collisionless Boltzmann equation

$$\frac{\partial f}{\partial t} + \frac{\mathbf{p}}{ma^2} \nabla f - m \nabla \Phi \frac{\partial f}{\partial \mathbf{p}} = 0 \quad (2.1)$$

and the Poisson equation

$$\nabla^2 \Phi(\mathbf{x}, t) = 4\pi G a^2 [\rho(\mathbf{x}, t) - \bar{\rho}(t)] \quad (2.2)$$

where Φ is the gravitational potential and $\bar{\rho}(t)$ is the background density. These equations are solved by sampling the phase-space density by a finite number N of particles. Said particles do not represent individual dark matter particles, because simulating all DM particles would require way to much computation time. Therefore they only produce collective, statistical properties. The equations of motion (in comoving coordinates) for such a system are

$$\frac{d\mathbf{p}}{dt} = -m \nabla \Phi \quad \frac{d\mathbf{x}}{dt} = \frac{\mathbf{p}}{ma^2} \quad (2.3)$$

By defining the proper peculiar velocity $\mathbf{v} = a\dot{\mathbf{x}}$ these can be combined into

$$\frac{d\mathbf{v}}{dt} + \mathbf{v} \frac{\dot{a}}{a} = -\frac{\nabla \Phi}{a} \quad (2.4)$$

where the derivative of the scale factor is given by $\dot{a} = H_0 E(a)$ with $E(a)$ being the expansion function (Eq. 1.15) (Dolag et al. 2008).

2.1.1 Calculation of the Gravitational Potential

The easiest way to solve the N-body problem by solving the Poisson equation (Eq. 2.2) is to directly sum the contributions of all particles

$$\Phi(\mathbf{r}) = -G \sum_j^N \frac{m_j}{\sqrt{(|\mathbf{r} - \mathbf{r}_j|^2 + \epsilon^2)}} \quad (2.5)$$

where \mathbf{r} is the position where the gravitational potential is evaluated, \mathbf{r}_j are the particle positions, m_j their mass and ϵ is the so-called gravitational softening. The direct-sum produces the most accurate solution for the potential from which the accelerations can be computed, but we need to remember that the particles only have collective meaningfulness. In order to correct some effects that are introduced by this simplification the gravitational force is smoothed by ϵ . The downside to this approach is, that the computation time is $\propto N^2$, which therefore becomes quite large for a small number N of particles (Dolag et al. 2008).

Beneficial to reduce the computational time the so-called *Tree algorithm*, a hierarchical multipole expansion, was introduced. Grouping together distant particles into larger cells and computing their gravity according to a multipole force, the number of force evaluations per particle can be reduced, because these groups are treated as *macro* particles in the sum of (Eq. 2.5). In this way the computation time can be reduced to $\propto N \log(N)$. The manner in which the particles are grouped, and the reason why this algorithm bears the name Tree, is a recursive subdivision of space. The "root" is a cubical node volume that contains all particles. The volume then is divided into 8 daughter nodes of half the side-length each. This is repeated again and again until the algorithm reaches nodes that only encompass single particles. These could be called "leaves". In order to obtain the forces, the tree is "walked", i.e. in every node the algorithm has to decide whether the multipole expansion yields an accurate enough partial force. Answering "yes" to this question cancels the "walk" and the multipole force is used, otherwise the node is "opened" and its daughter nodes are examined. A multipole expansion is accurate enough, if the nodes are sufficiently small and distant. Evidently, this algorithm only approximates the true force, but can be made arbitrarily accurate by using lower levels of the tree (Dolag et al. 2008).

The last method we want to address briefly are *Particle-Mesh* (PM) methods. Here forces are computed on a mesh and then interpolated from this mesh to obtain potentials and forces at the particle positions. This typically is done by assigning densities to the mesh points from the particle positions, transforming this density field into Fourier space, where the solution of the Poisson equation and the potential are acquired and then the derivatives of the potentials are interpolated to the particle positions to produce the individual forces. The advantage of this method is, that the calculations can be done very fast via Fast Fourier Transform ($\propto N \log(N)$). On the flip side its resolution is limited, because the amount of mesh cells typically equals the number of particles in the simulation (Dolag et al. 2008).

The best performance today is obtained by combining the Tree algorithm and a Particle-Mesh method (*tree-PM*). Here the potential in Fourier space is split into a long-range and a short-range part. The long-range part is computed with the mesh method in Fourier space while the short-range part is solved by the Tree algorithm in real space (Dolag et al. 2008).

2.1.2 Time Integration

In the last section we described how the forces acting on the particles can be calculated efficiently in N -body simulations. In order to create a simulation evolving over time these calculations need to be evaluated in many time steps. The important variables in the N -body problem are the positions and the velocities of all particles, which both can be solved by ordinary differential equations $\dot{\mathbf{x}} = \mathbf{v}$ and $\dot{\mathbf{v}} = \mathbf{f}(\mathbf{v})$, where the first ODE can easily be solved after the solution for the second is known. There are several methods to solve these ODEs. We will focus on the *Runge-Kutta method* (RK) and the *leap-frog method*.

The RK scheme achieves its accuracy by splitting the time step Δt from step n to step $n + 1$ into subsets. If the variable that is to be evaluated is \mathbf{y} the subsets for a fourth order accuracy are constructed by

$$\begin{aligned}\mathbf{k}_1 &= \mathbf{f}(\mathbf{y}_n, t_n) \\ \mathbf{k}_2 &= \mathbf{f}(\mathbf{y}_n + \mathbf{k}_1\Delta t/2, t_n + \Delta t/2) \\ \mathbf{k}_3 &= \mathbf{f}(\mathbf{y}_n + \mathbf{k}_2\Delta t/2, t_n + \Delta t/2) \\ \mathbf{k}_4 &= \mathbf{f}(\mathbf{y}_n + \mathbf{k}_3\Delta t/2, t_n + \Delta t)\end{aligned}\tag{2.6}$$

where \mathbf{y}_n is the value of the variable of the current step and the coefficients $\mathbf{k}_{2,3}$ are evaluated at the so called mid-points. The value of the variable for the next step \mathbf{y}_{n+1} then is given by (Dolag et al. 2008, p.10f)

$$\mathbf{y}_{n+1} = \mathbf{y}_n + \left(\frac{\mathbf{k}_1}{6} + \frac{\mathbf{k}_2}{3} + \frac{\mathbf{k}_3}{3} + \frac{\mathbf{k}_4}{6} \right) \Delta t\tag{2.7}$$

If we want to solve the ODEs for the positions and the velocities, we not only have one variable \mathbf{y} , but two: \mathbf{v} and \mathbf{x} . In this case we need to calculate the coefficients in (Eq. 2.6) for both alternately, because the coefficients for the velocities and the positions are accelerations and velocities respectively and we need the velocities to find the positions at which the accelerations are evaluated and in return the accelerations to calculate the velocities. One way to implement this in PYTHON¹ can be found in (App. B.1). This is a part of the code that created (Fig. 2.1).

The *leap-frog method* can directly integrate second order ODEs of the form $\ddot{\mathbf{x}} = \mathbf{f}(\mathbf{x})$, by shifting the evaluations of the forces and positions by half a time step. There are two different schemes that achieve this. One starts with a **drift (D)** of the positions by half a time step, and the other one starts by updating the velocities with the forces at the actual time (**kick, K**). The first one is abbreviated as **DKD**

$$\begin{aligned}\mathbf{x}_{n+1/2} &= \mathbf{x}_n + \mathbf{v}_n\Delta t/2 \\ \mathbf{v}_{n+1} &= \mathbf{v}_n + \mathbf{f}(\mathbf{x}_{n+1/2})\Delta t \\ \mathbf{x}_{n+1} &= \mathbf{x}_{n+1/2} + \mathbf{v}_{n+1}\Delta t/2\end{aligned}\tag{2.8}$$

and the second is the **KDK** version (Dolag et al. 2008, p.11)

$$\begin{aligned}\mathbf{v}_{n+1/2} &= \mathbf{v}_n + \mathbf{f}(\mathbf{x}_n)\Delta t/2 \\ \mathbf{x}_{n+1} &= \mathbf{x}_n + \mathbf{v}_{n+1/2}\Delta t \\ \mathbf{v}_{n+1} &= \mathbf{v}_{n+1/2} + \mathbf{f}(\mathbf{x}_{n+1})\Delta t/2\end{aligned}\tag{2.9}$$

An illustration of how these schemes integrate an orbit of a point mass around a fixed massive center and how the specific orbital energy evolves over time is shown in (Fig. 2.1). In the upper left panel it can be seen, that a second order RK scheme has a huge drift in the orbital energy even for a few orbits. The **KDK** leap-frog integration (lower panel) is also second order accurate and shows only a precession of the elliptical orbit while conserving the energy. Even the computationally more expensive fourth order RK scheme (upper right panel) shows a drift of the orbital energy (for illustrative reasons a bigger time step is used in this panel).

¹<https://www.python.org/>

A linear and exponential fit to the orbital energies of the fourth and second order RK scheme results in a decay of 70% after $20a$ for the fourth order RK scheme and a gain of 70% for the second order RK scheme. (Dolag et al. 2008) give the decay and gain as $\sim 40\%$ over 200 orbits and $\sim 30\%$ over 50 orbits, respectively. Because the orbital energy is not conserved in these schemes the leap frog integration is the preferred method of integration.

The phenomenon, that the leap-frog method conserves energy and the RK method doesn't can be explained by checking if they are time reversible. As stated by the Noether theorem, a symmetry of the equations of motion leads to a conserved quantity. Invariance under time translation (time reversibility) leads to the conservation of energy (Bartelmann 2015, p.198). This is not the case for the RK integration. We can see this by inserting (Eq. 2.6) into (Eq. 2.7). The second summand in (Eq. 2.7) then is proportional to $(\Delta t)^2$.

Only after introducing a variable time step, most often based on $\Delta t \propto 1/\sqrt{|\mathbf{a}|}$, the leap-frog integration schemes time reversibility is lost. In this case a small error develops, which grows four times faster in the **DKD** variant. Nevertheless a variable time step is needed for cosmological simulations because many regions have different densities and therefore require different time steps. Because of the smaller error the **KDK** scheme is the preferred method in cosmological simulations (Dolag et al. 2008).

2.2 Hydrodynamical Simulations

We explained how DM is simulated in the above section and now we will turn to baryonic particles. From these we can also derive properties like temperature, entropy or metallicity. In order to do so we have to solve four equations that describe the evolution of fluid. The *Euler equation*

$$\frac{d\mathbf{v}}{dt} = -\frac{\nabla\mathbf{P}}{\rho} - \nabla\Phi \quad (2.10)$$

the *continuity equation*

$$\frac{d\rho}{dt} + \rho\nabla\mathbf{v} = 0 \quad (2.11)$$

and the *first law of thermodynamics*

$$\frac{du}{dt} = -\frac{P}{\rho}\nabla\cdot\mathbf{v} - \frac{\Lambda(u,\rho)}{\rho} \quad (2.12)$$

where \mathbf{v} and \mathbf{P} are the velocity and pressure for all particles, Φ is the gravitational potential, ρ the fluid density, u the internal energy of the gas and $\Lambda(u,\rho)$ the cooling function. Φ was already determined with the methods from (Sec. 2.1.1) and $\Lambda(u,\rho)$ is neglected. If we assume an ideal, monatomic gas ($\gamma = 5/3$), the last equation we need is the *equation of state*

$$P = (\gamma - 1)\rho u \quad (2.13)$$

By using these sets of equations the highly non-linear gravitational clustering in the universe can be studied in great detail. Two main features emerge in cosmological hydrodynamical flows: 1) Supersonic velocities that develop shock discontinuities which can be described by the Rankine–Hugoniot jump conditions (Sec. 1.3.5). 2) Vast dynamical range in space and

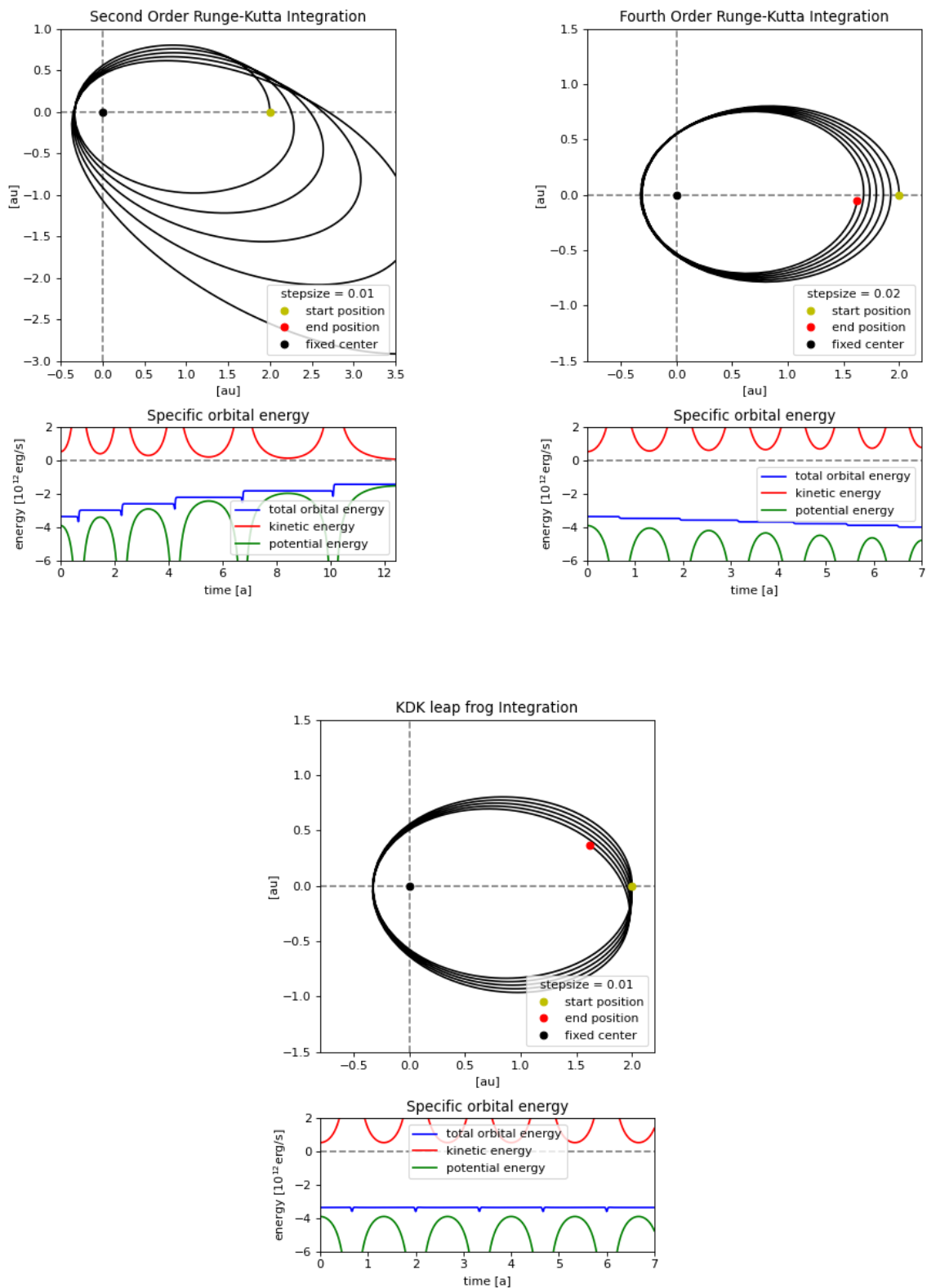


Figure 2.1: Evolution of an orbit of a point mass around a fixed massive center and the evolution of the specific orbital energy computed with different integration schemes: Second Order Runge-Kutta (upper left panel), fourth order Runge-Kutta (upper right panel) and KDK leap-frog integration (lower panel). The energy evolution shows, that the Runge-Kutta integration schemes don't conserve energy while the leap-frog integration does. In the fourth order Runge-Kutta integration a longer time step was used for illustrative reasons.

time, e.g. hierarchical structure formation includes scales of single galaxies to the largest interconnected structures.

Again there is a range of possible solving schemes for these equations. We will focus on a particle method, i.e. discretizing mass (Dolag et al. 2008).

2.2.1 SPH

SPH stands for *smoothed particle hydrodynamics*, which already suggests one key point of this method, namely that fluid quantities of a particle are *smoothed* out over a certain region in space, to produce continuous distributions. This is the reason why it performs good in high density regions but poorly in low density regions. It solves the Lagrangian form of the Euler equation. Other weaknesses lie in shocks and dynamical instabilities, because a sizeable artificial viscosity and spurious pressure forces on particles in regions with high density gradients are introduced. Yet, the adaptive nature of SPH makes it the most common method in numerical hydrodynamical simulations.

Because of the discretization of mass it is clear that particles in collapsed structures are closer together than in low density regions, which makes SPH adaptive in spatial resolution whilst the mass resolution stays constant. The fluid quantities will be smoothed according to the *smoothing kernel*. This function can be Gaussian in the easiest implementation², but the most used variant is called the *B₂-spline*, which is given by

$$W(x, h) = \frac{\sigma}{h^\nu} \begin{cases} 1 - 6\left(\frac{x}{h}\right)^2 + 6\left(\frac{x}{h}\right)^3, & 0 \leq \frac{x}{h} < 0.5, \\ 2\left(1 - \frac{x}{h}\right)^3, & 0.5 \leq \frac{x}{h} < 1, \\ 0, & 1 \leq \frac{x}{h} \end{cases} \quad (2.14)$$

where ν is the dimensionality, i.e. 1,2 or 3, h is the *smoothing length* and the normalisation σ is given by

$$\sigma = \begin{cases} \frac{16}{3}, & \nu = 1 \\ \frac{80}{7\pi}, & \nu = 2 \\ \frac{8}{\pi}, & \nu = 3 \end{cases} \quad (2.15)$$

therefore $4\pi \int x^{\nu-1} W(x, h) dx = 1$ holds. Another important property the kernel needs to satisfy is, that it collapses to a delta function if the smoothing length approaches zero: $W(x, h) \rightarrow \delta(x)$ for $h \rightarrow 0$. This property is required because if the smoothing length would be zero the property should not be smoothed out over a volume around the particle, but all of it should be concentrated on the particle. Also the *B₂-spline* is favoured over the Gaussian kernel (comparison in App. B.2), because it has compact support (i.e. $W(\mathbf{x}, h) = 0$ for $|\mathbf{x}| > h$) and therefore only the particles within a sphere of radius h instead of all the particles have to be considered in the summation below. Using the number of particles in this sphere N_{sph} a variable smoothing length can be defined by fixing it to a constant value. Then h changes with density $h^3 = 3N_{\text{sph}}/4\pi n_g$. Usually this is done with $N_{\text{sph}} = 32$ to 80, but a symmetric kernel $W(\mathbf{x}_i - \mathbf{x}_j, h_i, h_j) = \bar{W}_{ij}$ has to be constructed and correction terms of $\partial W/\partial h$ are ignored, which leads to a difficulty to conserve entropy and internal energy at the same time. This kernel can now be used to create continuous fluid quantities as follows

²<https://philip-mocz.medium.com/create-your-own-smoothed-particle-hydrodynamics-simulation-with-python-76e1cec505f1>

$$\langle A(\mathbf{x}) \rangle = \int W(\mathbf{x} - \mathbf{x}', h) A(\mathbf{x}') d\mathbf{x}' \quad (2.16)$$

The continuous fluid quantity then can be found, if one knows the discretized values A_j and the positions \mathbf{x}_j and their masses m_j , as

$$\langle A_i \rangle = \langle A(\mathbf{x}_i) \rangle = \sum_j \frac{m_j}{\rho_j} A_j W(\mathbf{x}_i - \mathbf{x}_j, h) \quad (2.17)$$

where the volume element $d\mathbf{x} = dx^3$ was replaced by the ratio of mass and density $m_j/\rho_j = V_j$ of the particles and it is assumed, that $W(\mathbf{x}_i - \mathbf{x}_j, h) = W(|\mathbf{x}_i - \mathbf{x}_j|, h)$. Considering the density $A_i = \rho_i$ in (Eq. 2.17), it becomes

$$\langle \rho_i \rangle = \sum_j m_j W(\mathbf{x}_i - \mathbf{x}_j, h) \quad (2.18)$$

which is the density of the fluid element represented by particle i . Also derivatives of the fluid properties can be calculated by

$$\nabla \langle A_i \rangle = \sum_j \frac{m_j}{\rho_j} A_j \nabla_i W(\mathbf{x}_i - \mathbf{x}_j, h) \quad (2.19)$$

where ∇_i is the derivative with respect to \mathbf{x}_i . One way to achieve a symmetric formulation of the derivatives in SPH is to use the identity

$$\nabla \left(\frac{A}{\rho} \right) = \frac{\nabla A}{\rho} - \frac{A}{\rho^2} \nabla \rho \iff \frac{\nabla A}{\rho} = \nabla \left(\frac{A}{\rho} \right) + \frac{A}{\rho^2} \nabla \rho \quad (2.20)$$

which leads to the derivative

$$\begin{aligned} \nabla \langle A_i \rangle &\stackrel{(2.20)}{=} \rho_i \nabla \left(\left\langle \frac{A_i}{\rho_i} \right\rangle \right) + \rho_i \frac{A_i}{\rho_i^2} \nabla \langle \rho_i \rangle \stackrel{(2.18), (2.19)}{=} \\ &= \rho_i \sum_j \frac{m_j}{\rho_j} \cdot \frac{A_j}{\rho_j} \nabla_j W(\mathbf{x}_i - \mathbf{x}_j, h) + \rho_i \frac{A_i}{\rho_i^2} \sum_j \nabla_j W(\mathbf{x}_i - \mathbf{x}_j, h) = \\ &= \rho_i \sum_j m_j \left(\frac{A_j}{\rho_j^2} + \frac{A_i}{\rho_i^2} \right) \nabla_i W(\mathbf{x}_i - \mathbf{x}_j, h) \end{aligned} \quad (2.21)$$

With these identities the hydrodynamic equations can be written in their SPH variation. The Euler equation (Eq. 2.10), where Φ is already determined and therefore is omitted, becomes

$$\frac{d\mathbf{v}_i}{dt} = -\frac{1}{\rho_i} \nabla P_i \stackrel{(2.21)}{=} - \sum_j m_j \left(\frac{P_j}{\rho_j^2} + \frac{P_i}{\rho_i^2} \right) \nabla_i W(\mathbf{x}_i - \mathbf{x}_j, h) \quad (2.22)$$

An identity similar to (Eq. 2.20) can be derived from $\nabla(\rho \cdot A)$, used with (Eq. 2.20) and averaged over for the first law of thermodynamics (Eq. 2.12) where $\Lambda(u, \rho)$ is omitted, which yields

$$\frac{du_i}{dt} = \frac{1}{2} \sum_j m_j \left(\frac{P_j}{\rho_j^2} + \frac{P_i}{\rho_i^2} \right) (\mathbf{v}_j - \mathbf{v}_i) \nabla_i W(\mathbf{x}_i - \mathbf{x}_j, h) \quad (2.23)$$

Simulation	Box0	Box1	Box2b	Box2	Box3	Box4	Box5
Size [Mpc]	3818	1273	909	500	182	68	26
mr	$2 \cdot 4536^3$	$2 \cdot 1512^3$	—	$2 \cdot 594^3$	$2 \cdot 216^3$	$2 \cdot 81^3$	—
hr	—	—	$2 \cdot 2880^3$	$2 \cdot 1584^3$	$2 \cdot 576^3$	$2 \cdot 216^3$	$2 \cdot 81^3$
uhr	—	—	—	—	$2 \cdot 1536^3$	$2 \cdot 576^3$	$2 \cdot 216^3$
xhr	—	—	—	—	—	$2 \cdot 1536^3$	$2 \cdot 576^3$

Table 2.1: Specifications of the simulation boxes: row 2 lists the volumes of the boxes and rows 3 to 6 list the numbers of particles for each resolution level mr (medium resolution), hr (high resolution), uhr (ultra high resolution), xhr (extra high resolution). Box3/uhr and Box5/xhr were stopped at about $z \sim 2$; Box4/xhr is planned for the future and Box2b/hr was stopped at around $z \sim 0.25$. These values were taken from the *Magneticum Website* and verified in (Dolag et al. 2017).

In both these equation inside the big brackets usually the so-called *artificial viscosity* Π_{ij} is included. It adds the capability to account for shocks. The last hydrodynamical equation, the *continuity equation* (Eq. 2.11) is automatically solved by this particles based method, as density can be calculated at any time from the particle positions (Eq. 2.18) (Dolag et al. 2008).

2.3 Magneticum

The *Magneticum Simulation*³ (Dolag et al. 2016) is based on the cosmological simulation code P-GADGET 3⁴ (Springel 2005a). It utilises the TreePM algorithm described in (Sec. 2.1.1) to compute gravitational forces and for the ideal gas the smoothed particle hydrodynamics (SPH) method is used (Sec. 2.2.1); here in a specific entropy conserving formulation (also internal energy is conserved). The time integration is done by a variant of the leap-frog integration presented in (Sec. 2.1.2). The specifics of the implementation of other physical features, e.g. thermal conduction, can be found in the already cited of following papers that discuss results of the *Magneticum Simulation*. As already mentioned (Sec. 1.2.2) the cosmological parameters of a Λ CDM model are adopted as measured by (Komatsu et al. 2011) and are given in (Tab. 1.1). Their results for the initial power spectrum were $n = 0.963$ and $\sigma_8 = 0.809$.

In order to reach high resolutions and high cosmological volumes, the simulations consists of several boxes with varying sizes and resolutions, as given in Tab. (Tab. 2.1). The cluster examined in this work was taken from Box2b with a high resolution (hr) (Hirschmann et al. 2014).

2.3.1 Snapshot File

The output of the simulation is written into so called *snapshot* files, which is the output format of the P-GADGET 3 Code. These files simply contain the state of the whole system at certain times. For large simulations they can be distributed into several files (i.e. SNAPSHOT_026.0 to SNAPSHOT_026.15). Each of these files contain a variable number of particles. Within one snapshot file the data is organised in blocks. There is a block for coordinates, one for velocities, one or temperature, etc. A list for these blocks in *Magneticum* can be found in (App. C.1). The first block acts as a header. Similar to a header in a FITS file⁵, it contains general information about the snapshot, like the number of particles per type in the snapshot,

³<http://magneticum.org>

⁴<https://wwwmpa.mpa-garching.mpg.de/gadget/>

⁵<https://fits.gsfc.nasa.gov/>

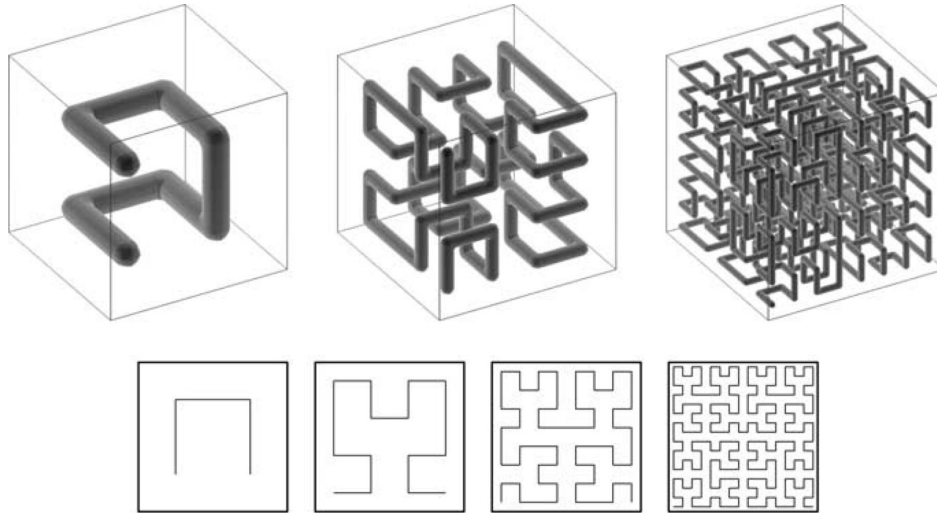


Figure 2.2: Peano-Hilbert curves in 3D (top row) and 2D (bottom row). Image taken from (Springel 2005a).

the redshift of the snapshot or flags informing about enabled code features like cooling. In (App. C.2) there is also a table listing the headers content. For each block the particles are sorted by six particle types. For our simulation these types are gas (ptype = 0), dark matter (ptype = 1) and stars (ptype = 4). Types 2, 3 and 5 (black holes) are not relevant for this work. Because the array of particles changes from snapshot to snapshot, or a given particle is stored in a different (sub-) snapshot file, a block that contains particle IDs is implemented in each snapshot file (Springel 2005b). Also, by cutting out a specific box within a snapshot file the sequence of particles changes, as particles can move in or out of that box. Therefore the particle IDs are important for tracing a particle between subsequent snapshots. *Magneticum* specifically writes to the Format 2 variant of the snapshot file. Here an identifier, a 4-character string, leads every block. For example the position and the mass block are preceded by the strings "POS " and "MASS" respectively. The other identifiers are listed in the table in (App. C.1) (Springel 2005b). Using these identifiers the data can easily be read into a PYTHON script using the g3read module by Antonio Ragagnin⁶.

The sequence in which the particles are stored in the snapshot files is oriented along so called *Peano-Hilbert curves*. This is a space-filling fractal, which maps a 3D $2^n \times 2^n \times 2^n$ grid onto a 1D curve. Such a curve can be described by a one-to-one mapping $p_n(i, j, k)$, where the value $p_n \in [0, \dots, n^3 - 1]$ is the position of the cell i, j, k on the curve. In (Fig. 2.2) examples for the Peano-Hilbert curve in two and three dimensions are shown. The original idea behind this mapping was to decompose the computation volume into a set of domains, which are each assigned to one processor in parallel computing systems. Particles are mapped onto the 1D curve which then is simply split into pieces that define the individual domains (Springel 2005a, p.13f). That this also defines the sequence in the output array is just a byproduct, which can be useful or disadvantageous.

2.3.2 Services and CosmoWebPortal

The Cosmological Web Portal⁷ (Ragagnin et al. 2017) can currently be used to explore Box2hr and Box2bhr. There are several services available. For example: PHOX creates virtual X-ray observations (Biffi et al. 2012), SMAC creates maps of physical quantities (e.g. baryonic

⁶<https://github.com/aragagnin/g3read>

⁷<https://c2pacosmosim.uc.lrz.de/>

density, bolometric X-ray luminosity etc.) as a fits file, ClusterFind creates data tables and scaling relations, where the global properties of the clusters can be specified. The service SimCut extracts a snapshot file which contains all original particle data in a region centered on a galaxy cluster. The size in the x-y-plane can be specified as a multiple of r_{500c} and the z-size adjusted arbitrarily. In order to use the service more independently the SimCut IDL routine of Klaus Dolag was executed by Ildar Khabibullin on the LRZ: Linux Cluster⁸. The data is stored there, because the simulation was run on the LRZ supercomputer SuperMUC⁹.

2.3.3 Units

The positions and velocities are given in comoving units. That means to convert to physical coordinates and velocities one has to divide positions "POS " by $(z + 1)$ and h and velocities "VEL " by $\sqrt{z + 1}$. The resulting units are kpc and km/s. Masses of each of the three particle types are given in units of $10^{10} M_{\odot}/h$. Dark matter particles have a constant mass of $m_{dm} \approx 6.9 \cdot 10^8 M_{\odot}/h$ at the hr resolution level. Gas and star particle masses are variable and their mean masses are $m_{gas} \approx 1.4 \cdot 10^8 M_{\odot}/h$ and $m_{stars} \approx 2.6 \cdot 10^7 M_{\odot}/h$. In the next sections positions will stay in comoving units. Everything else will be converted to physical units. Further we will look at gas density and entropy. Entropy will be calculated from temperature and gas density. Therefore we also need to convert gas density to physical units:

$$\rho_{\text{phy}} = \rho_{\text{code}} \cdot (1 + z)^3 \cdot \frac{m_{\text{unit}}}{l_{\text{unit}}^3} \cdot h^2 \quad (2.24)$$

where $m_{\text{unit}} = 1.989 \cdot 10^{43}$ and $l_{\text{unit}} = 3.085678 \cdot 10^{21}$. The resulting units are g cm^{-3} (Springel 2005b).

2.4 Center of Mass

We want to explore the motion of the particles of an infalling cluster with respect to the main cluster. For the focus to be fixed onto the region between them it is best to look at the center of mass (COM) of the particles. The center of mass is defined as

$$\text{COM} = \frac{1}{M} \sum_i m_i \mathbf{x}_i \quad (2.25)$$

where $M = \sum_i m_i$ is the total mass of the system, m_i and \mathbf{x}_i are the mass and the coordinate of the i -th particle. If the sum of all external forces acting on the system vanishes the COM moves with the velocity

$$\mathbf{v}_{\text{COM}} = \frac{1}{M} \sum_i m_i \mathbf{v}_i \quad (2.26)$$

where \mathbf{v}_i is the velocity of the i -th particle (Bartelmann 2015, p. 89). Converting the positions and velocities into the center of mass frame requires subtracting the COM from the positions and the velocity of the COM from the velocities.

$$\mathbf{x}_{\text{COM},i} = \mathbf{x}_i - \text{COM} \quad \mathbf{v}_{\text{COM},i} = \mathbf{v}_i - \mathbf{v}_{\text{COM}} \quad (2.27)$$

⁸<https://doku.lrz.de/display/PUBLIC/Linux+Cluster>

⁹<https://doku.lrz.de/display/PUBLIC/SuperMUC-NG>

The COM in the COM frame has the coordinates $(0, 0, 0)$, the positions have smaller values, namely just the distances from the COM, and the velocities are also corrected.

2.5 Calculating Radial Velocities

In the center of mass frame the velocities at each position can easily be decomposed into its radial and tangential fraction. The subscript COM is omitted in the further sections. The radial velocity v_r of a particle is the part of the velocity \mathbf{v} that is parallel or antiparallel to the radial unit vector $\hat{\mathbf{r}}$, which points from the center $(0, 0, 0)$ to its position \mathbf{x} . It can be calculated with the scalar product:

$$v_r = \mathbf{v} \circ \hat{\mathbf{r}} = \mathbf{v} \circ \frac{\mathbf{x}}{|\mathbf{x}|} \quad (2.28)$$

As tangential, radial and total velocity constitute a right triangle (Fig. 2.3), the tangential velocity can be calculated from the other two by the Pythagorean Theorem:

$$v_t = \sqrt{v^2 - v_r^2} \quad (2.29)$$

where v is the absolute value of the total velocity \mathbf{v} . Since every particle has a different velocity it is important to normalize them in order to analyze if a particles velocity is predominantly radial or tangential. The normalized values are the radial velocity fraction and tangential velocity fraction:

$$f_r = \frac{v_r}{v} \quad f_t = \frac{v_t}{v} \quad (2.30)$$

Determining these fractions and coloring the particles of a galaxy cluster w.r.t. to f_r reveals which particles are infalling, outgoing or mostly tangential.

2.6 Phase Diagrams

After obtaining the radial velocities one can create a *phase diagram* to further identify substructures and infalling particles. The x-axis represents the radii while the y-axis represents the radial velocities. Infalling particles will have high negative radial velocities and high radii and therefore be located in the bottom right corner. Outgoing particles will have moderate positive radial velocities at moderate radii and will be located in the top left corner. After one core passage infalling particles will become outgoing and eventually turn around at high radii, while their radial velocities are decreasing and become negative again. This will continue in a loop. The exact evolution depends on how the velocities change during a core passage and therefore depend on the particle type. The idealized phase-space distribution of DM particles and the radial velocity profile of gas is shown in (Fig. 2.4). In reality gas particles will not suddenly stop after a certain radius as shown in this graphic, but follow a similar path then the DM particles but stop after about one core passage in the contrary to DM which can pass several times.

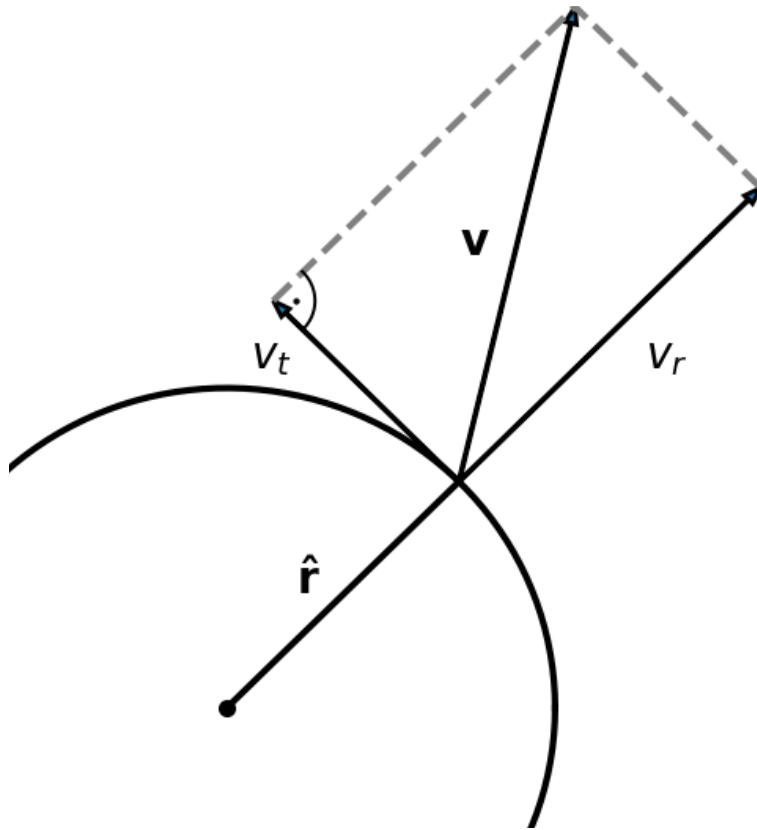


Figure 2.3: Decomposition of the velocity \mathbf{v} into radial velocity v_r and tangential velocity v_t .

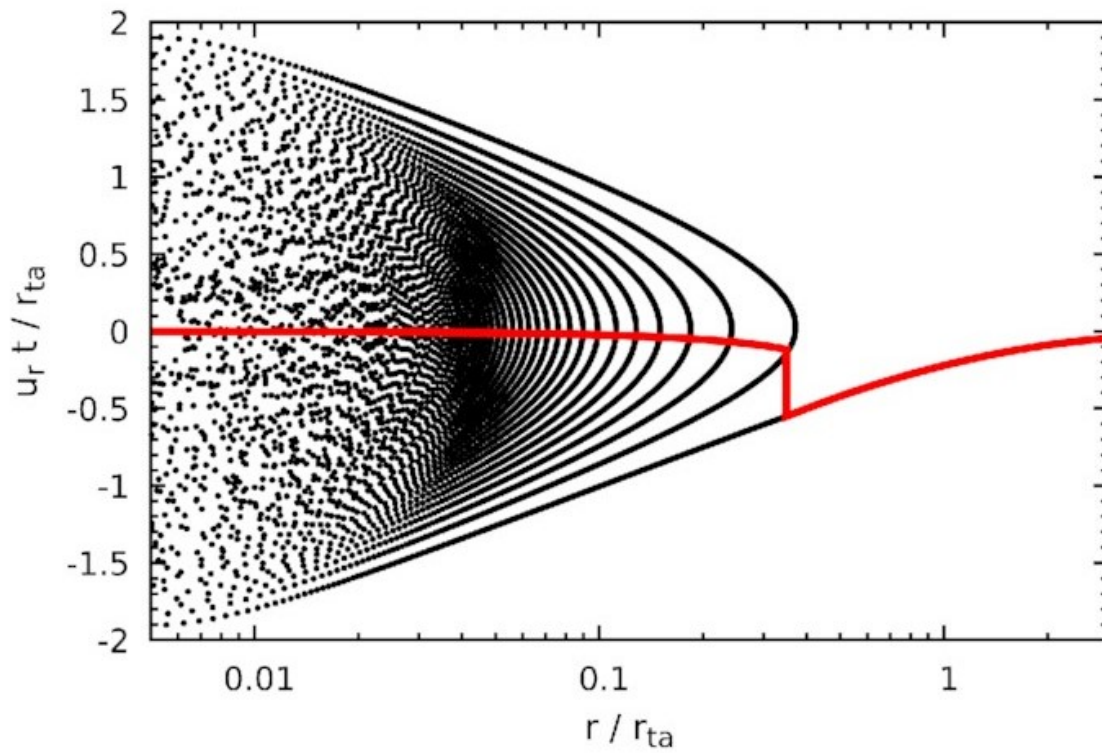


Figure 2.4: Idealized phase-space distribution of DM particles (black) and radial velocity profile of gas; taken from (Zhang et al. 2021).

Chapter 3

Analysis

A cluster with a very high $m500c$ mass was chosen for this work (as found in the `cluster.txt` file accessed from the *Magneticum* Website¹), because usually the bigger the mass is, the more merger activity is present in a cluster. As the evolution of its state is to be examined, six snapshots at different times corresponding to different redshifts were accessed. SimCut was used to create snapshots of a box with comoving side lengths of 20 Mpc centered on the position of the cluster for each snapshot. A Table listing all properties for each snapshot can be found in (App. D). (Fig. 3.1) shows the X-ray emission map of snapshot `s027`² created from a photon list extracted by Stephan Vladutescu-Zopp using PHOX and translated into the maps by Ildar Khabibullin.

The positions and velocities in these snapshots were converted into the center of mass frame as described in (Sec. 2.4). Because we want to focus on a smaller region, the COM was calculated for the particles within a box with half a side length of $r500c$ for each snapshot. All particle type were considered, because each particle regardless of its type moves according to the combined gravitational potential. As dark matter dominates the mass and therefore gravity, it is very important to include it when calculating the COM, even if we just want to look at e.g. how the gas particles behave. Next, all particles in the 20 Mpc box were translated into the center of mass frame of this COM.

As already stated, we want to focus on a small region around the center. Therefore only particles within a cube centered on the COM in each snapshot were considered. The side length of this cube in each snapshot is the same, namely the mean value of $r500c$ for each time step (~ 1240 kpc). In addition, the particle number has to be reduced again, firstly to reduce the computation time needed for the analysis. The second, more significant reason is that if we look at those particle along one projection axis, and produce a scatter plot the particles that are stored at the end of the array are plotted last. This can have the effect, that the center of the cluster is covered by particles in the outskirts. For these reasons only 6% of the particles, that means every 17th entry in the arrays is used for most of the analysis. This way the considered particles are randomly selected and therefore can still represent the simulation data accurately. This leaves e.g. about 50000 gas particles to analyze.

3.1 Projected Scatter Plots

Before we can create scatter plots projected along one axis, we have to solve one last problem. If we create scatter plots with the arrays that we obtained now, the Peano-Hilbert curve (Sec.

¹http://magneticum.org/data.html#FULL_CATALOGUES

²A short video showing the evolution can be found here <https://johannesstoiber.de/resources.html>

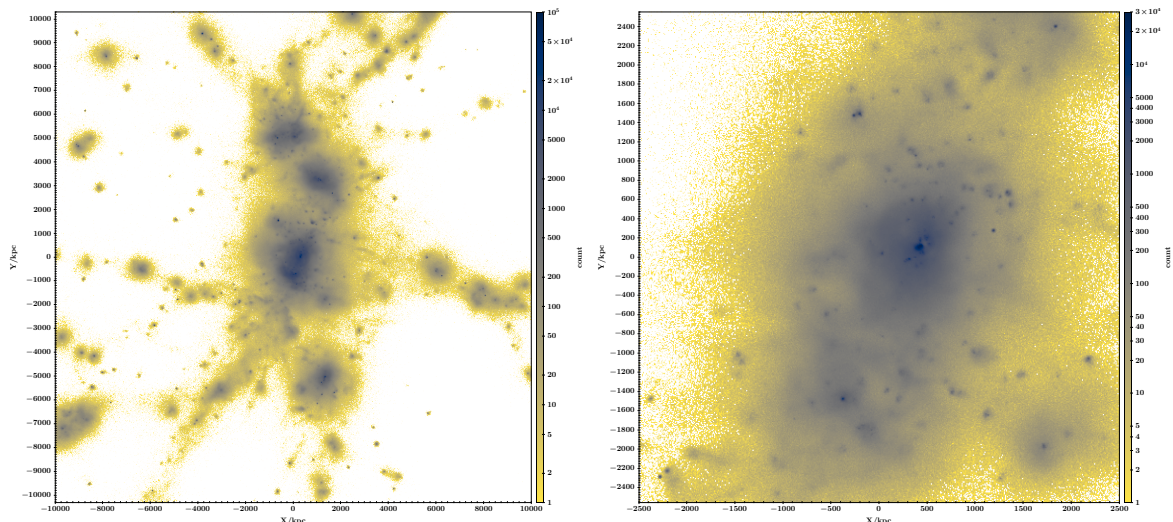


Figure 3.1: X-ray emission map of the UID 1 cluster in s027; the colorbar shows the total number of counts for a virtual observation with $t_{\text{obs}} = 10^7$ s and an effective area of $A_{\text{eff}} = 10^3$ cm 2 ; left panel: 20×20 Mpc/h box; right panel: zoomed in 5×5 Mpc/h box.

2.3.1) is visible, because the particles in the array follow the same sequence in which they were stored in the snapshot file. In order to counteract this the arrays were shuffled right after reading them into the analysis code.

Now we can look at several properties. The positions are scatter plotted and colored according to suitable color scales. The radial velocity fraction was calculated according to (Sec. 2.5) and plotted this way. The result is shown in (Fig. 3.2) for gas, (Fig. 3.3) for DM and (3.4) for stars. In the top two and the middle left panels of (3.2) a lot of infalling (red) particles can be seen in the bottom left corner. They represent the gas of an infalling substructure. They hit the center of the main cluster in the middle right panel. Afterwards (bottom two panels) a lot of particles are outgoing (green) in the top right corner. The exact movement of these particles is more complex and will be investigated in (Sec. 3.3). Similar motion can be seen in (Fig. 3.3) and (Fig. 3.4) with the difference that bulk of outgoing particles already leave the frame in the bottom left panel. This suggests, that DM and stars pass through the cluster much faster.

The motion of the gas can also be investigated by analyzing temperature (Fig. 3.5), gas density (Fig. 3.6) and entropy (Fig. 3.7). In the following temperature will be given in keV calculated from the "TEMP" block from the snapshot file, gas density is calculated from the "RHO" block with (Eq. 2.24) and entropy is calculated from the former two with (Eq. 1.53). Metallicity as defined by (Eq. 1.57), i.e. relative to the suns metallicity, will be used in (Sec. 3.3.2). In (3.5) one can see, that the center of the main cluster is hotter than its surroundings. On top of that, one can see how the gas is heated by the infalling gas in the top right and the middle left panel. The middle right panel shows the highest temperature as the infalling gas reaches the main core. After this the gas in the top right corner is heated as seen in the bottom left panel. This is an outgoing shock that was initiated by the infalling gas. It passes through the core undisturbed and continues to travel outward. Snapshot s028 (middle left panel) will be further investigated in (Sec. 3.5). The heating is due to adiabatic compression of the gas and shocks that develop as the infalling gas is slowed down by the main clusters gas.

In (Fig. 3.6) the substructure is best seen in snapshot s028 (middle left panel). The density is increased there, because the infalling gas is compressed as it encounters the gas particles of the cluster at the center. This will also be analyzed in more detail in (Sec. 3.5).

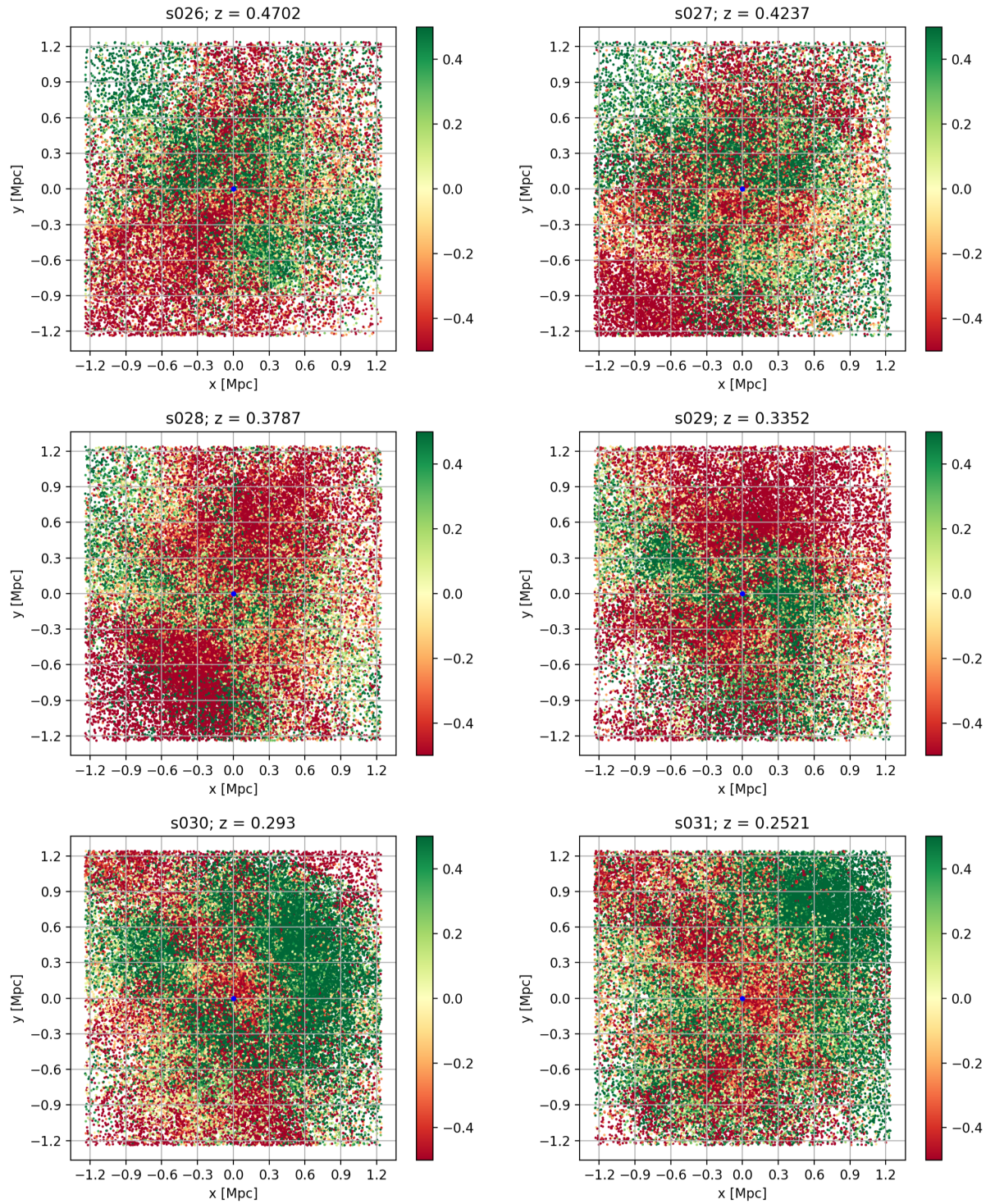


Figure 3.2: Scatter plot of gas particles colored according to their radial velocity fractions in the reference frame of the COM; green: negative (infalling); red: positive (outgoing); yellow: close to zero (mostly tangential).

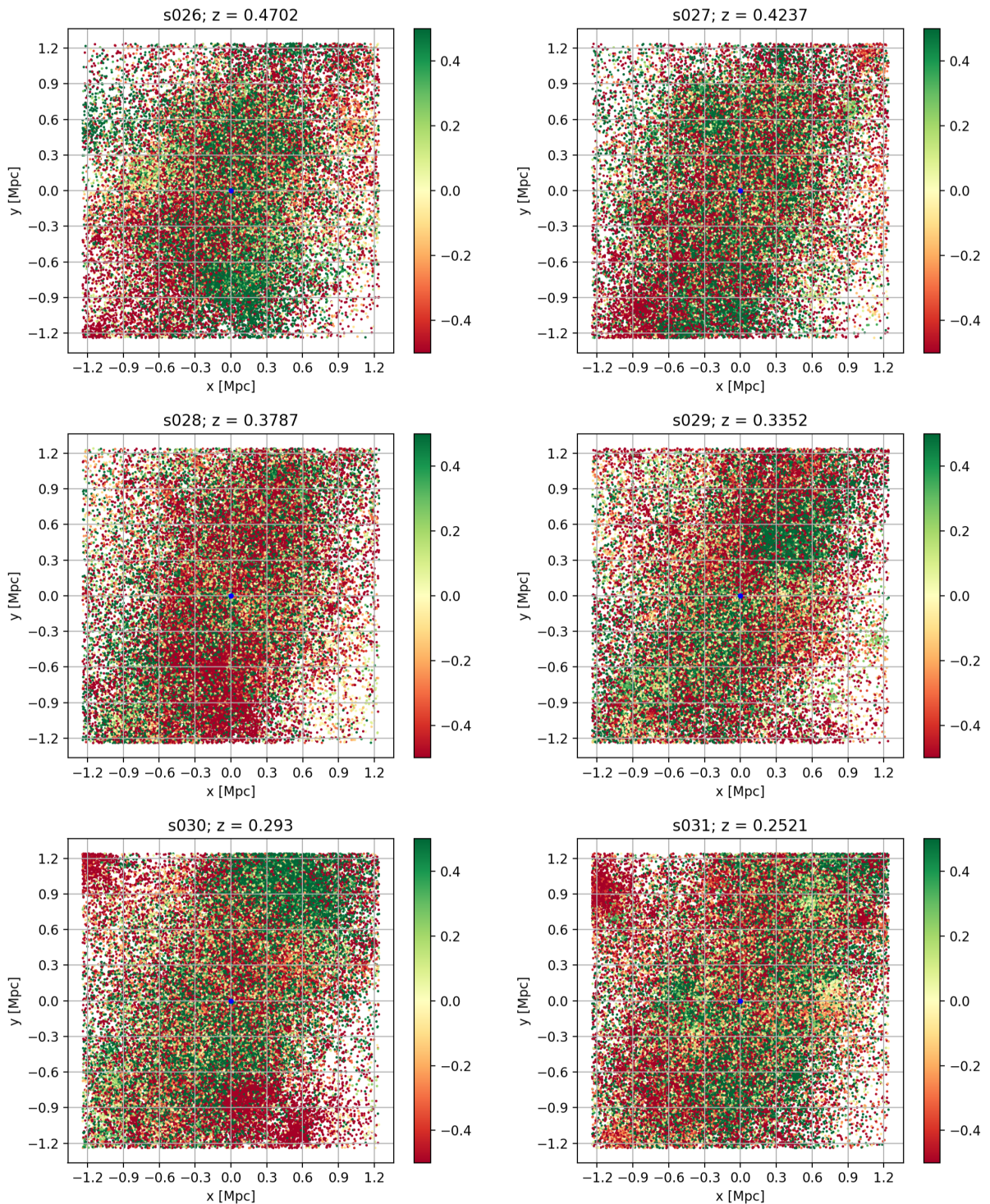


Figure 3.3: Scatter plot of DM particles colored according to their radial velocity fractions in the reference frame of the COM; green: negative (infalling); red: positive (outgoing); yellow: close to zero (mostly tangential).

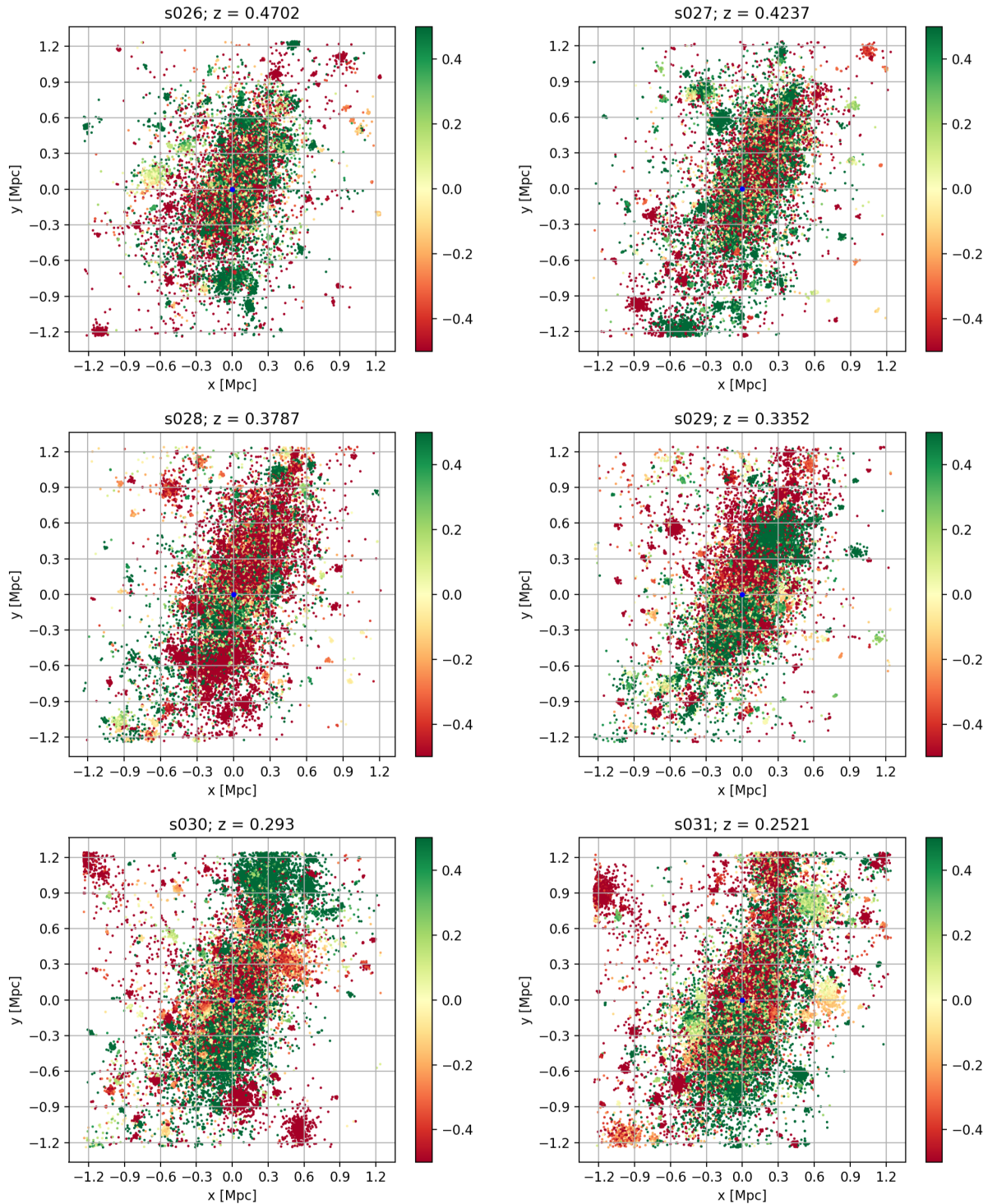


Figure 3.4: Scatter plot of star particles colored according to their radial velocity fractions in the reference frame of the COM; green: negative (infalling); red: positive (outgoing); yellow: close to zero (mostly tangential).

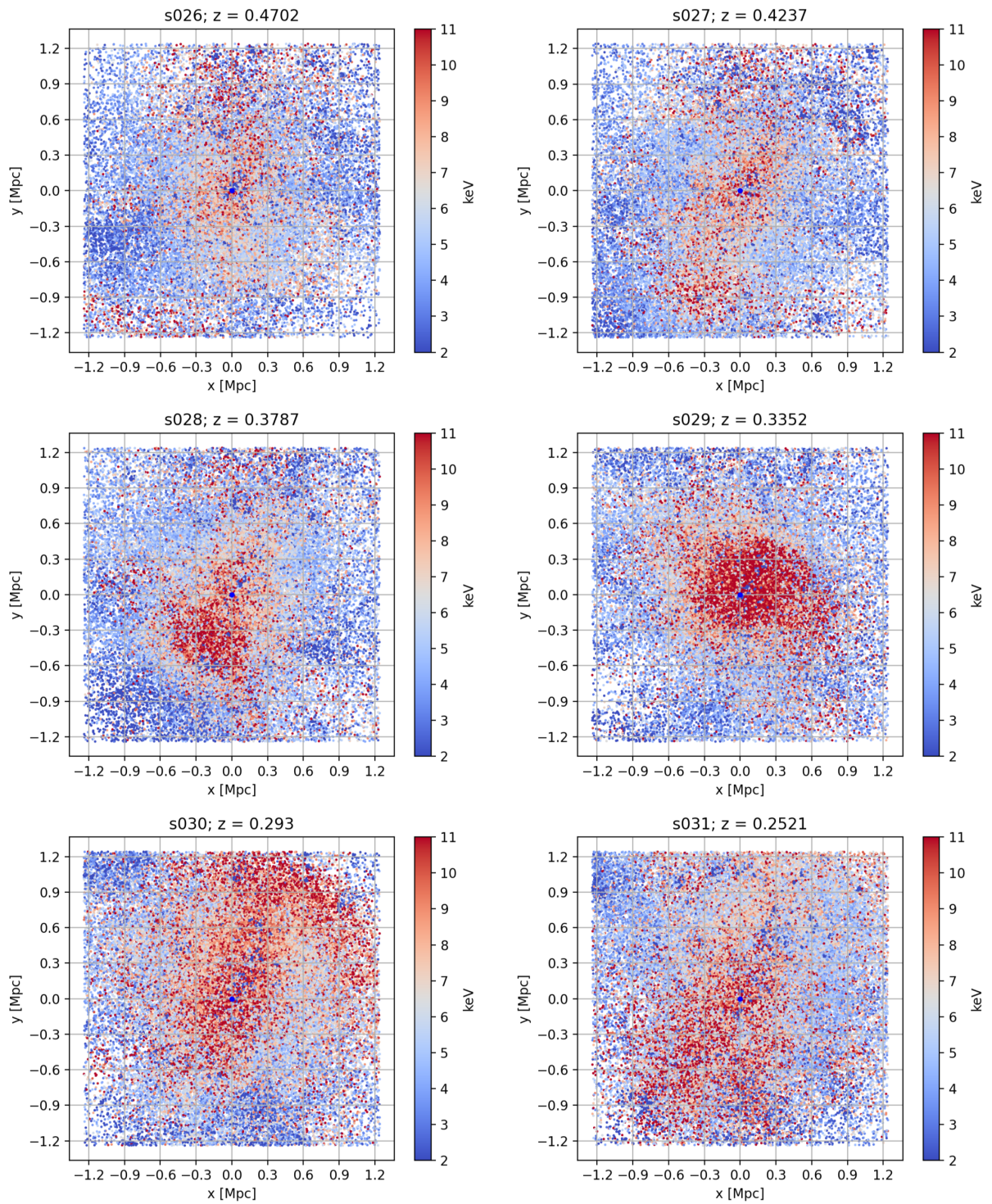


Figure 3.5: Scatter plot of gas particles colored according to their temperature.

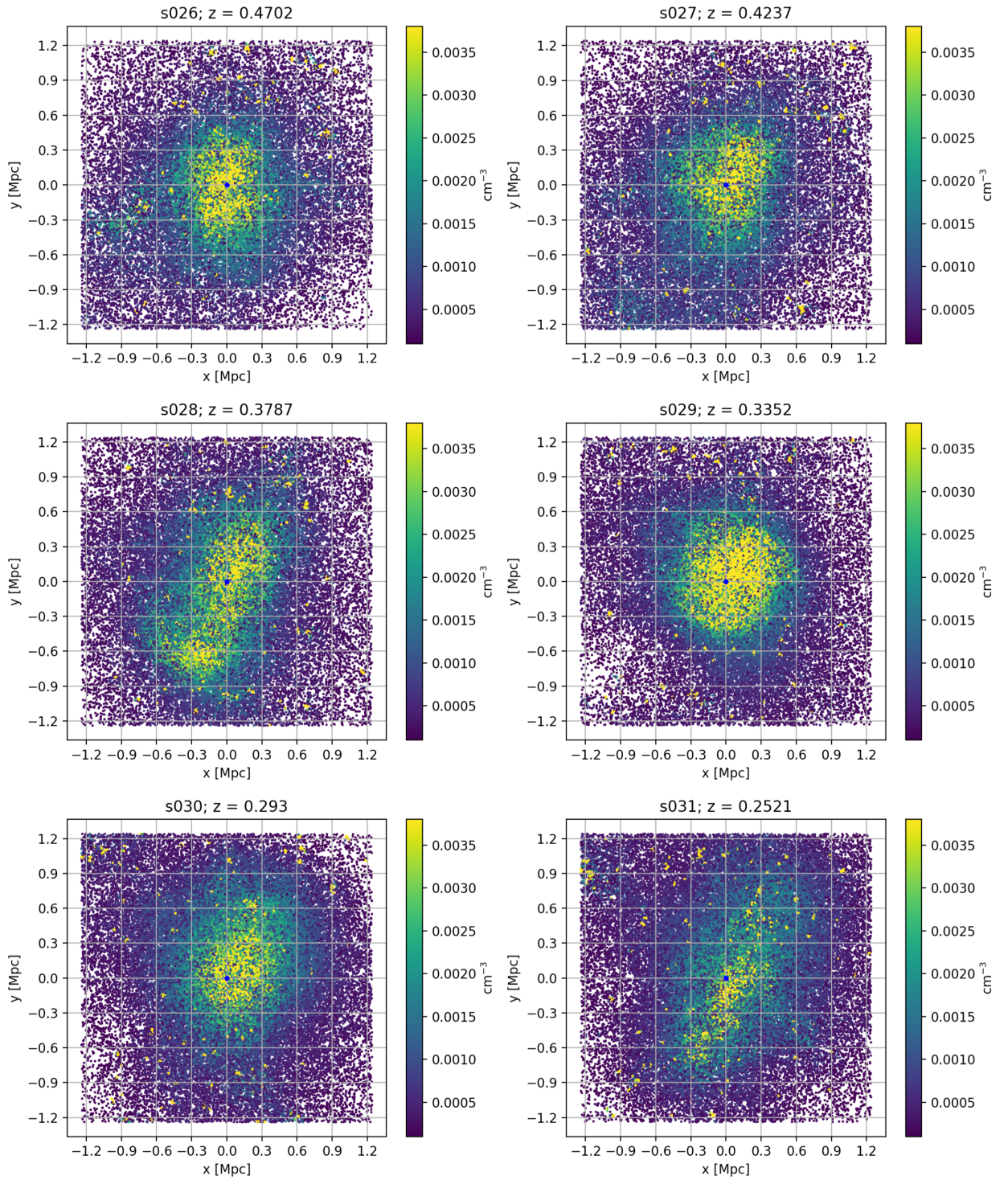


Figure 3.6: Scatter plot of gas particles colored according to their gas density.

The low entropy core of the main cluster is the most prominent feature in (Fig 3.7) (every panel). The infalling substructure also has low entropy as seen in the middle left panel. Again there is a eye catching high entropy region visible in the top right corner of the bottom left panel attributed to a shock. The entropy profile in snapshot s028 (top right panel) will also be determined in (Sec. 3.5).

3.2 Phase Diagrams

Supplementary to the above view of the radial velocity fraction phase diagrams (Sec. 2.6) were produced for gas, DM and stars. They are shown in (Fig. 3.8 - 3.10).

Again the motion of each particle type can be seen. There is a branch from $r = 1000$ kpc to $r = 1800$ kpc and $v_r = -800$ km/s to $v_r = -200$ km/s in the top middle panel in (Fig. 3.8) which represents the infalling gas. The bulk of the particles (yellow) has negative radial velocities, which then become positive and finally settle roughly at zero again in the next panels (top right, and the bottom three). It can also be noticed, that the center of the bulk reaches almost $r = 400$ kpc in the bottom left panel before it move to almost $r = 1000$ kpc. (Fig. 3.9) presents a similar development for the DM particles. The bulk is more concentrated for DM and therefore the movement looks sharper. In comparison to the gas particles, DM achieves higher magnitudes of radial velocities. The bulk of the star particle in (Fig. 3.10) stays at a low radius, where the BCG (Brightest cluster galaxy) is located. But its radial velocity also slightly oscillates around zero. The individual infalling galaxies and groups can be distinguished from each other best in this plot as they are concentrated in little blobs. The motion of all the particles is similar to the flow described in (Sec. 2.6). In order to better understand the dynamics of individual particles their path is traced in the next section.

3.3 Tracing Particles

3.3.1 Sub Sample

As mention in (Sec. 2.3.1) the particles can be traced by their unique IDs. But before this can be done a sub sample of particles needs to be selected. We want the chosen particles to belong to the same structure, which means their position and also their velocities are comparable. In order to ensure this it is best to select particles within a six dimensional sphere in phase space. The condition a particle needs to fulfill can be written as

$$\sum_{i=1}^3 \frac{(x_i - \bar{x}_i)^2}{r_x^2} + \sum_{i=1}^3 \frac{(v_i - \bar{v}_i)^2}{r_v^2} < 1 \quad (3.1)$$

where i stands for the three spatial dimensions, x and v are position and velocity and \bar{x} and \bar{v} are the mean position and velocities of particles within a preselected rectangle in phase space. r_x and r_v take on the role of a radius for the six dimensional sphere. The preselection rectangle corresponds to the branch of infalling particles described in the last section and is also restricted to only include particles within the octant in with the infalling substructure is located. r_x and r_v are 800 kpc and 1800 km/s for each particle type. The sub sample consists of ~ 2500 particles for gas, ~ 1500 for DM and ~ 1600 for stars. Now the positions and velocities for stars and DM and additionally temperature, gas density, entropy and metallicity for gas were traced. This sub sample is shown on top of the phase diagrams in (Fig. 3.11) to (Fig. 3.13).

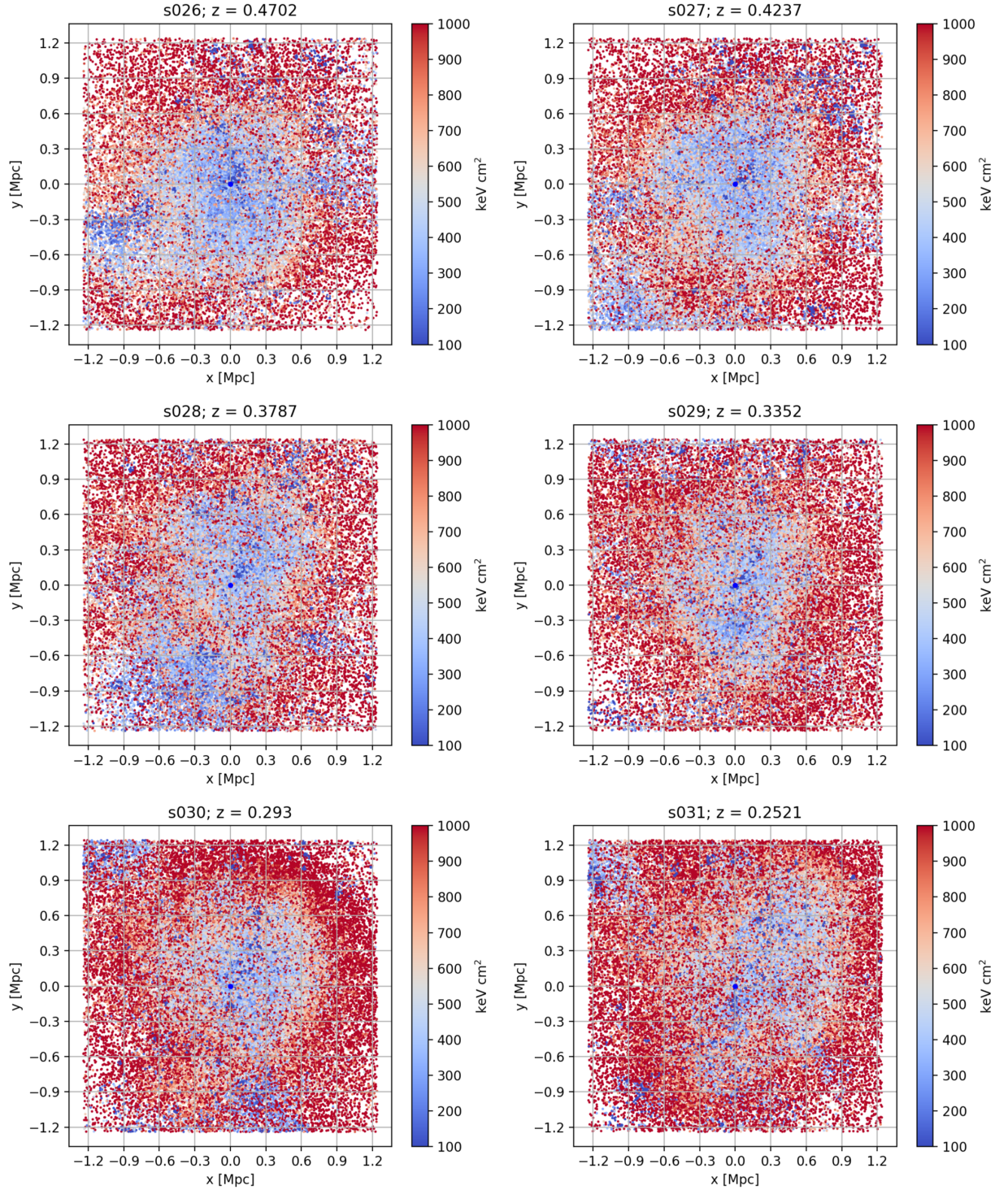


Figure 3.7: Scatter plot of gas particles colored according to their entropy.

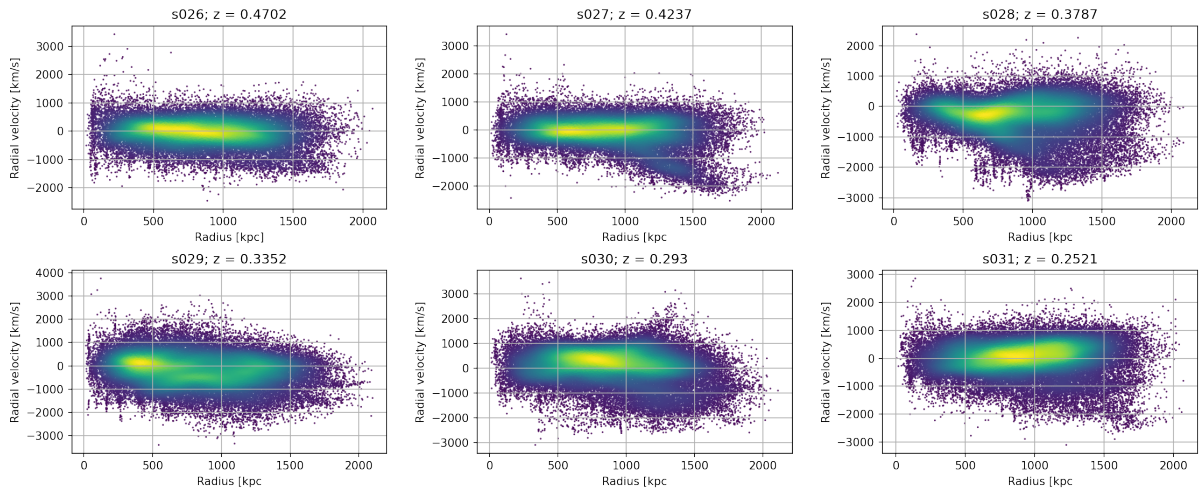


Figure 3.8: Phase diagrams for gas particles.

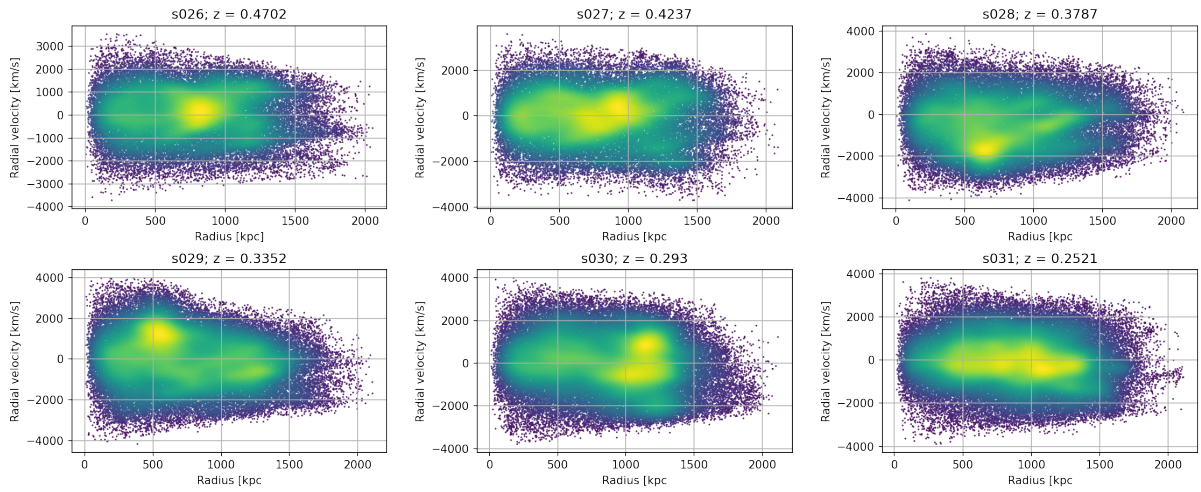


Figure 3.9: Phase diagrams for DM particles.

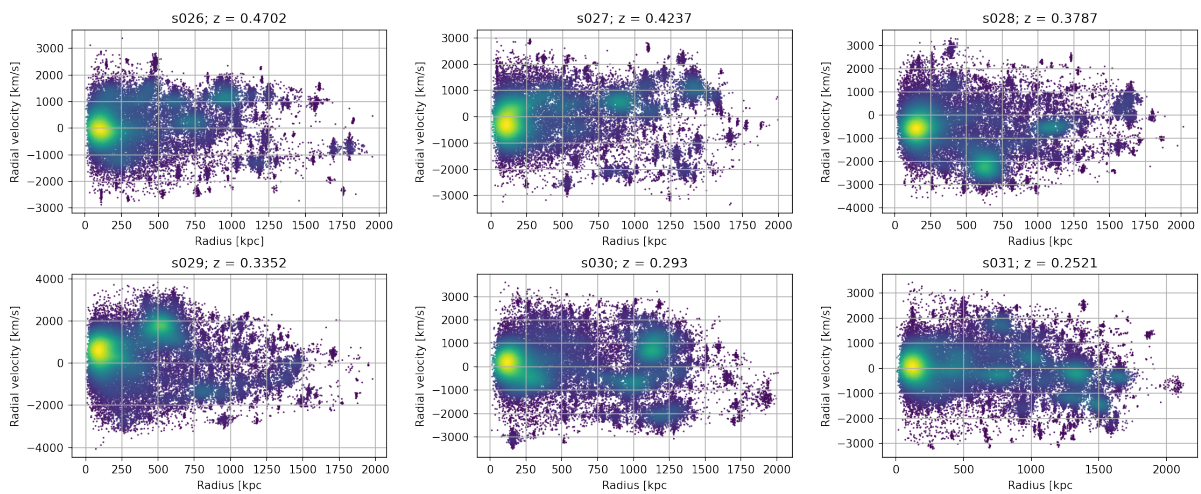


Figure 3.10: Phase diagrams for star particles.

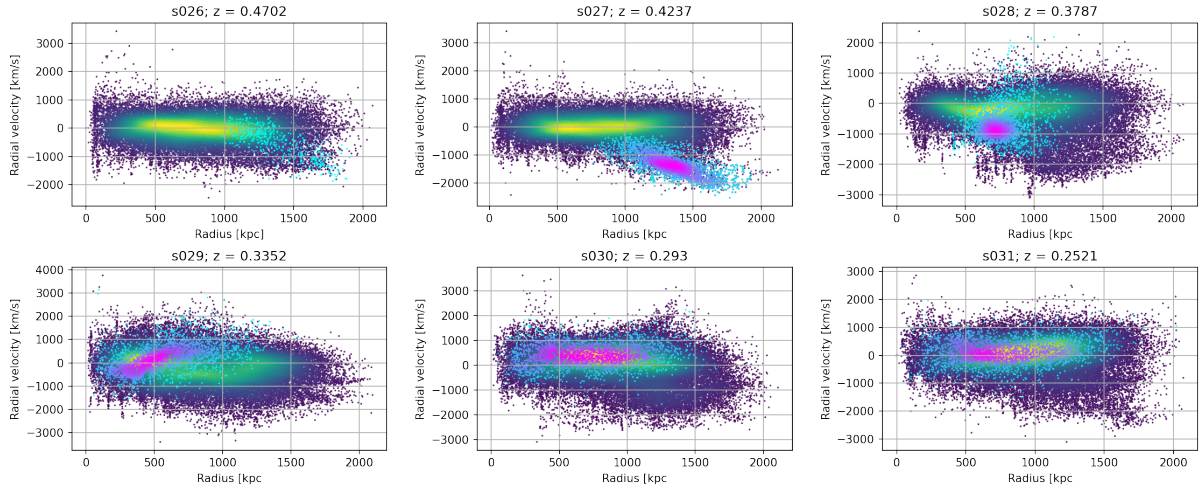


Figure 3.11: Phase diagrams for gas particles and traced gas particles.

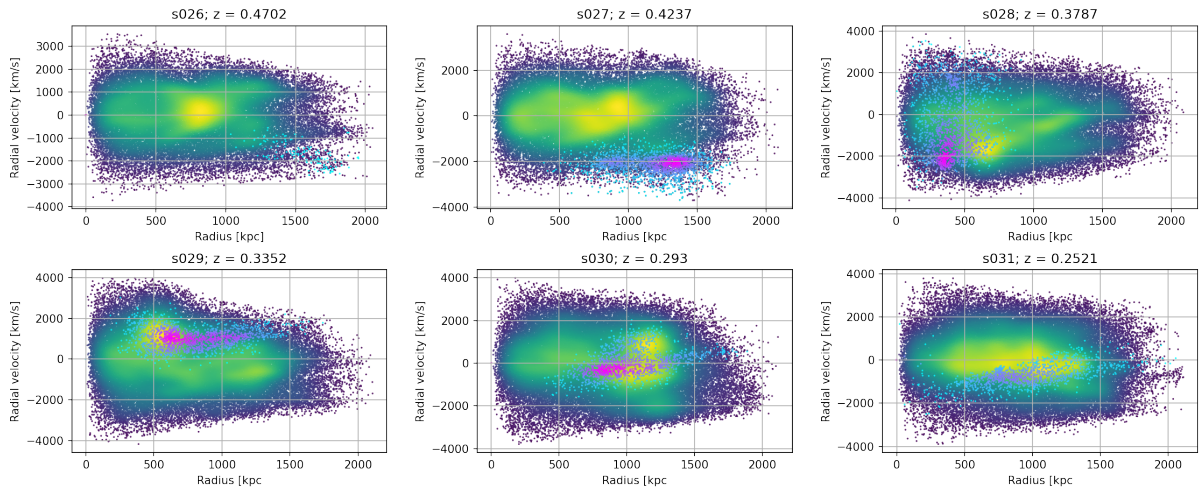


Figure 3.12: Phase diagrams for DM particles and traced DM particles.

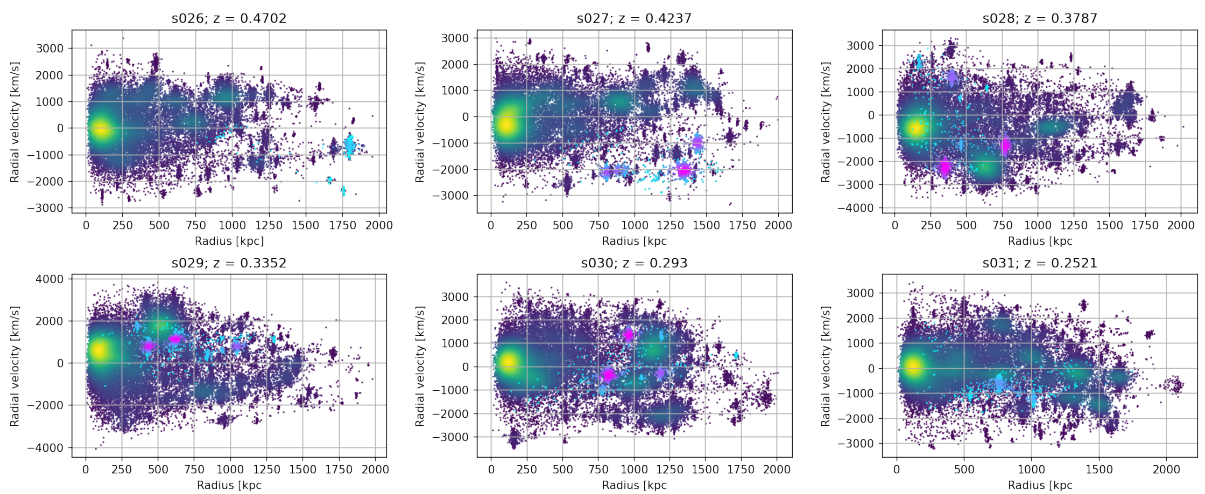


Figure 3.13: Phase diagrams for star particles and traced star particles.

The traced gas particles in (Fig. 3.11) have large radii with large negative radial velocities in the top left and middle panel, then move inwards as the radial velocities and radii become smaller (top right panel) and finally pass through the center as the velocities transition from negative to positive in the bottom left panel. Afterwards the gas has small positive radial velocities but settles around zero (last two panels) over a large section of radii. Traced DM behaves the same in (Fig. 3.12) in the top three panels but reaches higher magnitudes of radial velocities. The bottom left panel shows that the DM particles are outgoing with higher velocities than gas and they don't settle in the next snapshots, but turn around in the bottom middle panel as their radial velocities become negative again and are infalling in the last panel. The picture for stars (Fig. 3.13) is analogical to the DM except, that the particles are concentrated in clumps. The top left panel shows the first traced infalling clump which is followed by another two in the top middle panel. The first one passes through the center in between s027 and s028 whereas the other two follow in between s028 and s029. In the bottom middle panel one can see that the two clumps already turned around and fall towards the center again (negative radial velocities) and the last galaxy follows in the bottom right panel. The movement of these particles was also traced in real space as shown in (Fig. 3.14) - (Fig. 3.16).

(Fig. 3.15) shows that infalling DM particles just pass through the center from the bottom right corner to the top right corner. One can not really tell, that they turn around and fall back to the center in the bottom right panel, but this was seen clearly in phase diagram (Fig. 3.12). The same is true for the traced star particles (Fig. 3.13).

A more interesting result is seen by tracing the gas particles (Fig. 3.14). The top two panels show the same behaviour - gas particles fall towards the center. But already in the middle left panel one can see that the gas is stopped and moved slightly to the left of the center as seen in the middle right panel. The bottom two panels show the gas wrapping around the center on both sides and the observed outgoing particles in the bottom middle panel of the phase diagram (Fig. 3.11) are not just attributed to particles that manage to pass around and leave the center in direction of the top right corner, but also because particles bounce off the center and move radially to the left or to the bottom.

It was expected that the DM and stars behave differently than gas. DM was implemented as collisionless and the distances between stars and galaxies are so large, that the probability of a collision is rather small. Gas on the other hand interacts with itself and experiences ram pressure and thermal pressure, which slows it down and eventually stops it.

In order to really see what happens to these gas particles not just their positions and velocities were traced but also their physical properties. In order to be able to compare this to the rest of the cluster the properties of the bulk of the particles in the center were also traced as a background.

3.3.2 Tracing of Gas Properties of the Sub Sample

For the temperature, gas density and entropy of the sub sample particles the median was calculated and to estimate the range of the properties the 32-quantile and 68-quantile was used. The resulting evolution is shown in (Fig. 3.17).

The top left panel shows that the temperature of the sample increases from ~ 3 keV up to ~ 8 keV in snapshot s029 and decreases afterwards to ~ 6 keV. The bulk of the cluster particles is hotter than the sub sample but also rises at the same time to ~ 10 keV. The sub sample temperature only surpasses the bulk temperature in s028. This gain coincides temporally with the stopping of the infalling particles as seen in (Fig. 3.14). In the last snapshot the

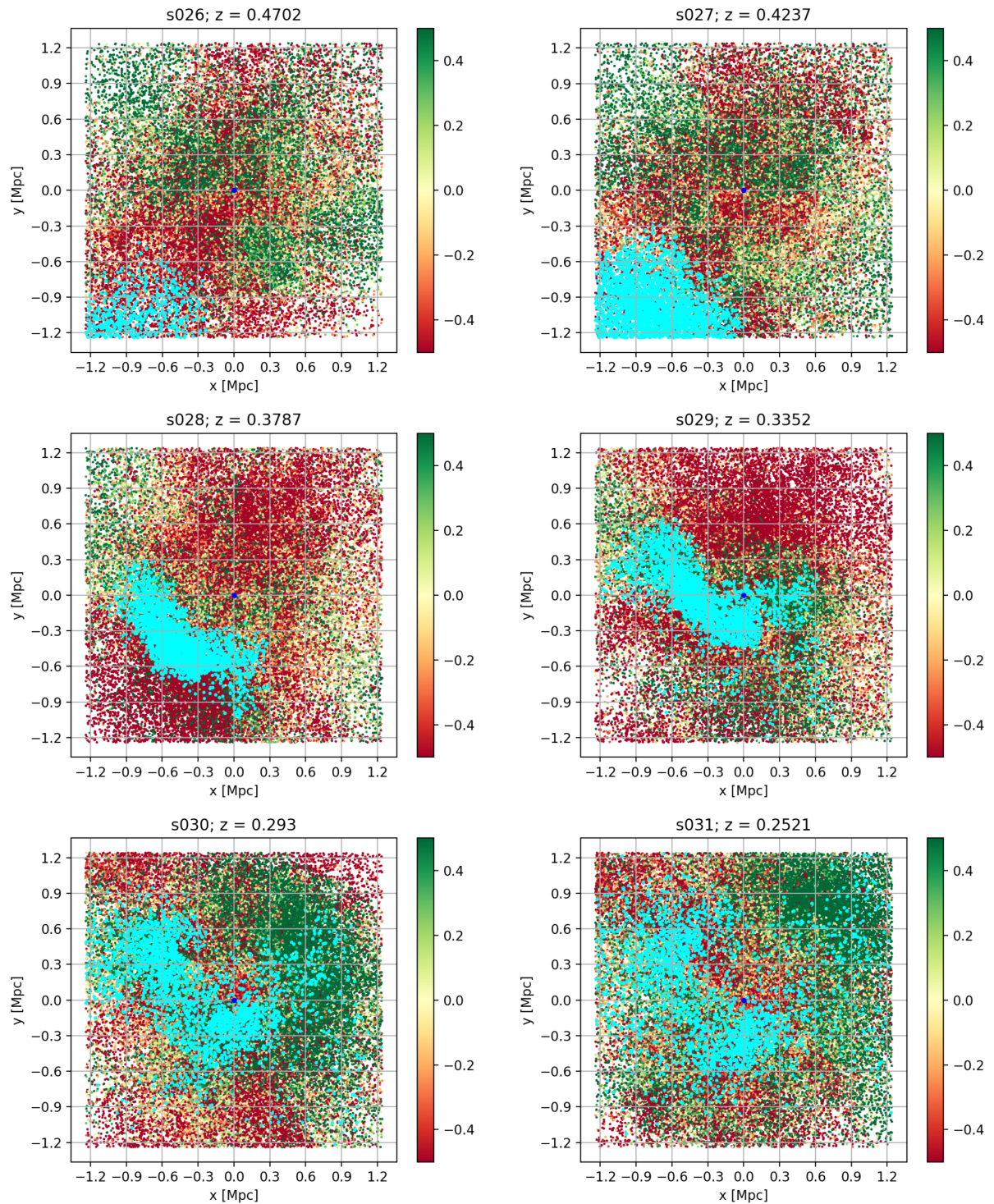


Figure 3.14: Scatter plot of gas particles colored according to their radial velocity fractions and traced gas particles in cyan.

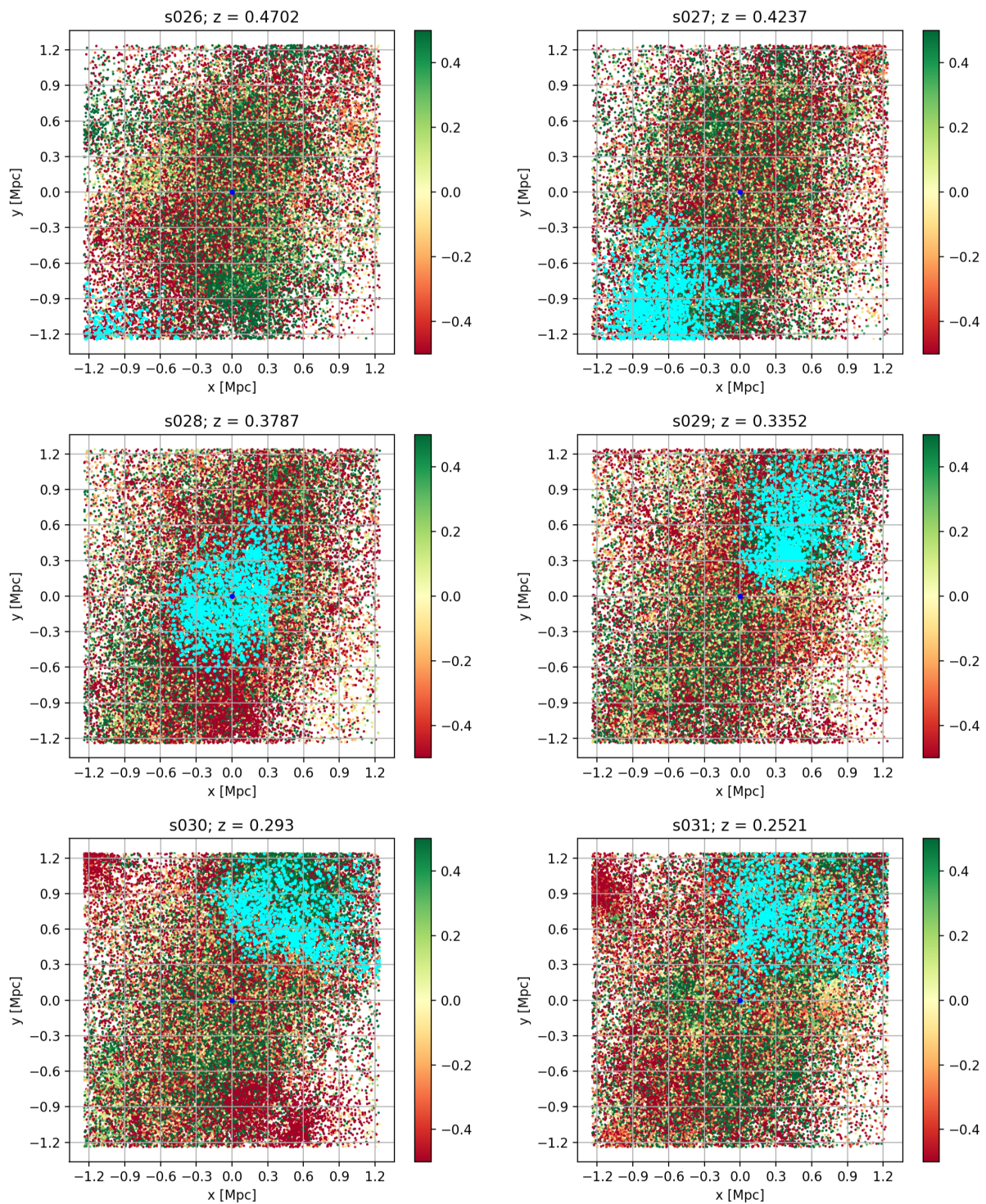


Figure 3.15: Scatter plot of DM particles colored according to their radial velocity fractions and traced DM particles in cyan.

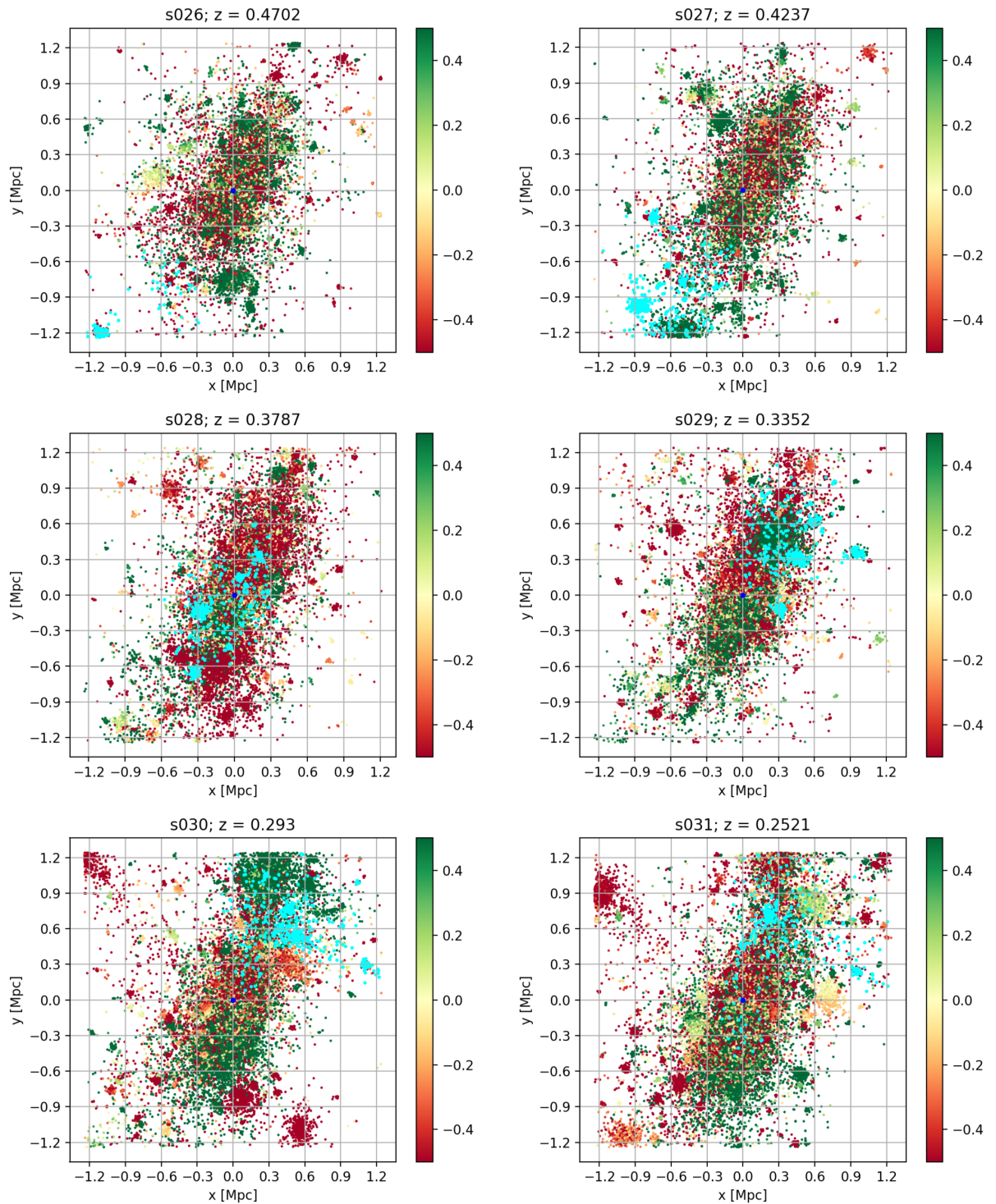


Figure 3.16: Scatter plot of star particles colored according to their radial velocity fractions and traced star particles in cyan.

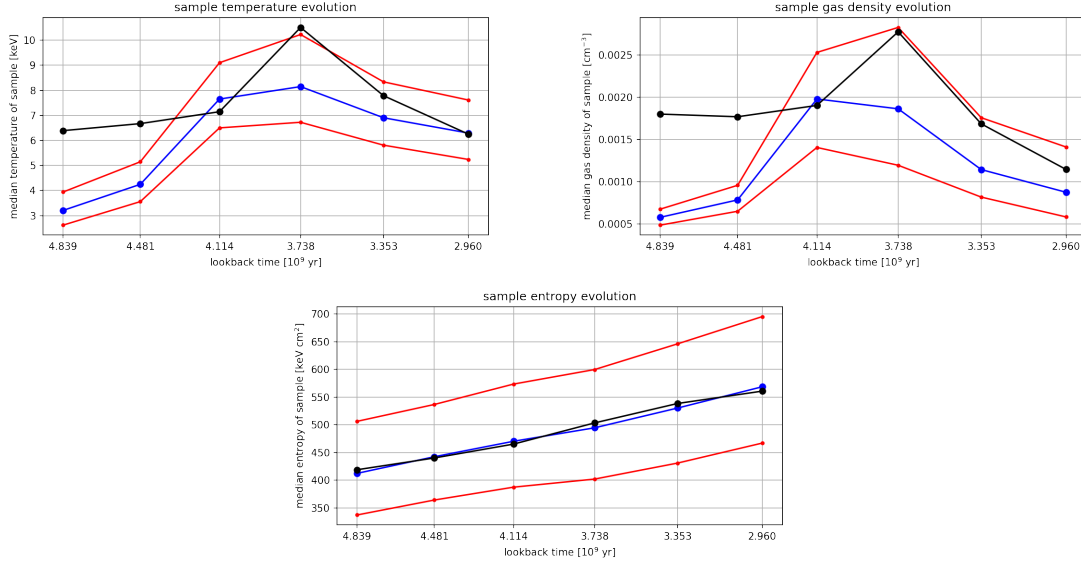


Figure 3.17: From top left to the bottom: temperature, gas density and entropy; the blue line is the median of each property, the red lines are the 32- and 68-quantile and the black line is the median of the background particles (bulk of cluster).

temperatures of the bulk particles is the same as the temperature of the sample particles. In the top right panel the gas density exhibits a corresponding evolution from $5 \cdot 10^{-4} \text{ cm}^{-3}$ up to $2 \cdot 10^{-3} \text{ cm}^{-3}$ and down to $8 \cdot 10^{-3} \text{ cm}^{-3}$. This is clear because stopping moving particles at a front increases the density. Similar to temperature the bulk gas density is also higher and is only surpassed by the sub sample in s028. In the bottom left panel one can see that the entropy of the sub sample is steadily increasing almost identical to the entropy of the bulk particles from 420 keV cm^2 to 570 keV cm^2 . The increase of temperature and density is due to compression that happens to the infalling gas as it enters the gas cloud of the main cluster. Depending on how high the infall velocity is, also a shock could develop and contribute to the rise of temperature and pressure behind it as discussed in (Sec. 1.3.5).

In order to analyze the chemical enrichment of the ICM the metallicity of the particles in the sub sample was traced. For comparison also the metallicity of background particles was considered in the same way as for the other properties. The results are shown in (Fig. 3.18). The top left panel shows the mean total metallicity evolution. The sub sample metallicity is about 0.2 whereas the background metallicity is about 0.4. They both are slightly increasing which is better represented by the bottom left panel. There the normalized metallicities are shown, i.e. the metallicities divided by the mean over all snapshots. Indeed both are increasing at roughly the same rate ($\sim 5 \%$ over 2 Gyr). In the top right panel one can see the ratio of the mean iron abundance to the mean oxygen abundance. The sub samples values lie roughly in between 1.38 and 1.45 and are increasing for the last five snapshots. The background ratio starts at about 1.2 and rises steadily to 1.27. In both components the iron content relative to the sun is higher than the oxygen content relative to the sun. Apparently more iron compared to oxygen is present in the sub sample. Again in the bottom right panel the normalized values are shown, depicting that the background and sub sample increase their iron content (relative to the oxygen content) at the same rate. The initial (and lasting) difference in total metallicity between the main cluster and the sub sample is due to the fact that the main cluster is older, therefore has a higher mass and stellar content, which had more time to enrich the ISM and ICM. This difference can in principle also be observed by X-ray observatories, because the spectrum of hot gas with a higher metallicity shows stronger iron emission lines (Spitzer 1962). X-ray missions might be able to distinguish between the main

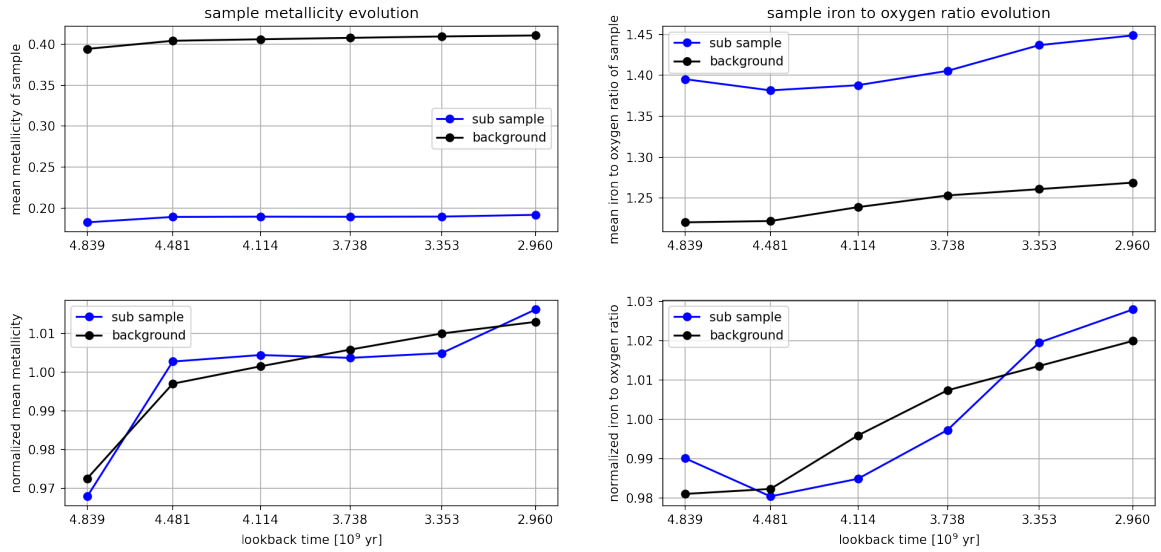


Figure 3.18: Top left: Mean of the total metallicity of the sub sample (blue) and mean of the total metallicity of the main cluster (black) in solar units; bottom left: Same as above but normalized (divided by the mean of all snapshots); top right: Mean of the ratio of the iron abundance to the oxygen abundance for the sub sample (blue) and the main cluster (black) in solar units; bottom left: Same as above but normalized.

cluster and infalling structures by using this result.

3.3.3 Particles Tracks

Another view of this situation can be gained by creating tracks of a few particles so that it can be seen which way an individual particle takes. This was done for DM and gas particles. The same selection algorithm as described above (Eq. 3.1) was used with smaller r_v and r_x . 50 tracks were produced for both particles types. The results are shown in (Fig. 3.19) and (Fig. 3.20).

In the top two panels of (Fig. 3.20) the start position and the first step of the gas particles is shown. They start to spread out but most of the tracks still go straight towards the center in the middle left panel. Already in the middle right panel there are at least two particles that now move radially outward in the center of the left hand side, but still a large portion moves towards the center. This slight change in directions becomes radical in the bottom row. Now all directions are present and the infalling gas starts to wrap around the core of the main cluster which continues in the last panel.

This flow is radically different for DM as seen in (Fig. 3.19). The top row looks similar to the top row of (Fig. 3.20). But in the middle row it is already clear, that the DM particles stay close together and head straight for a point near the center of mass. The bottom row shows how they then continue on a their orbit, that means the tracks have a kink and the particles leave the frame at the top.

3.3.4 Tracing the Radial Velocities of the Tracks

For these individual tracks the radial velocity fraction of gas and DM were traced. On the contrary to above no median was calculated but just the individual values are shown in (Fig.

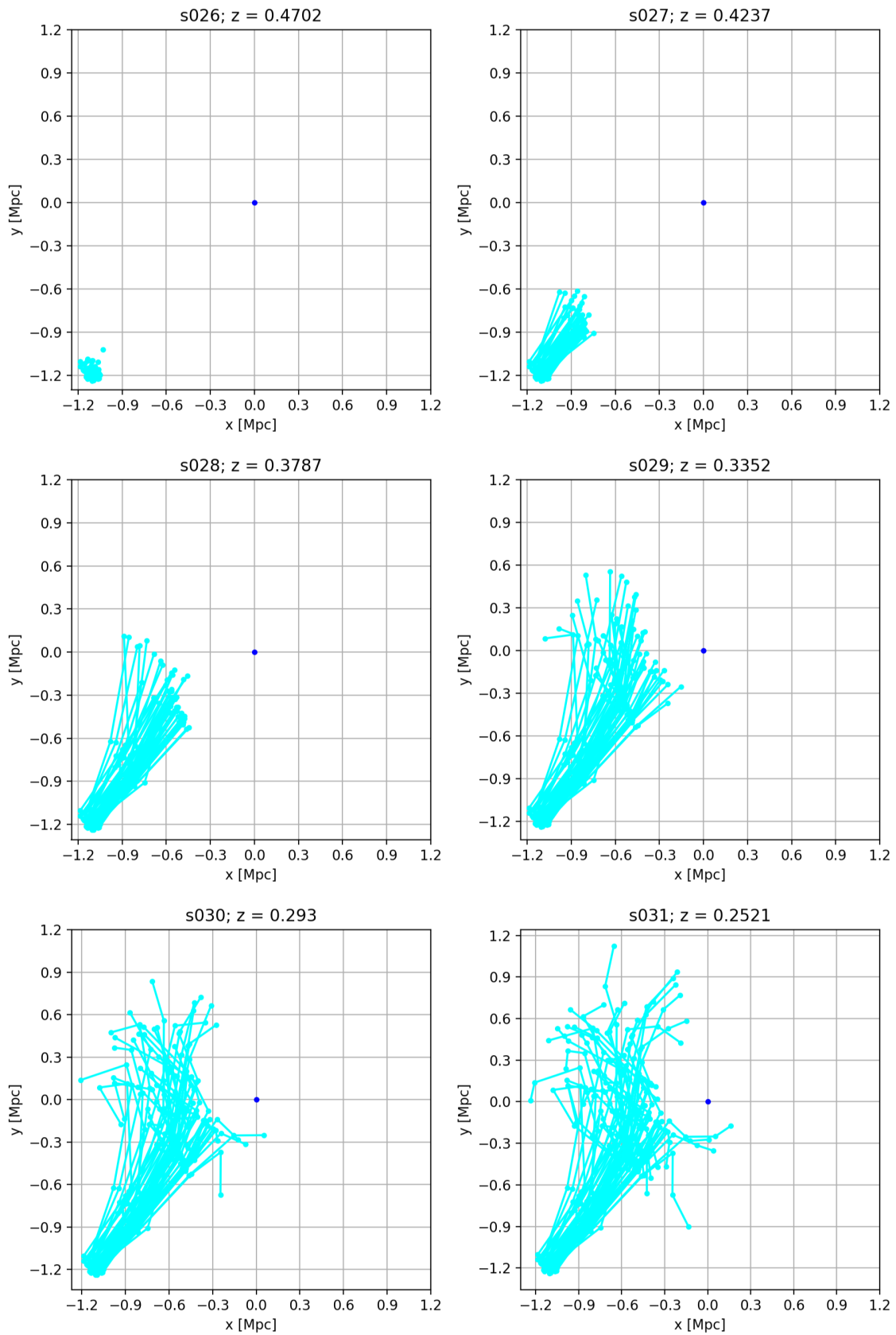


Figure 3.19: Tracks of 50 gas particles.

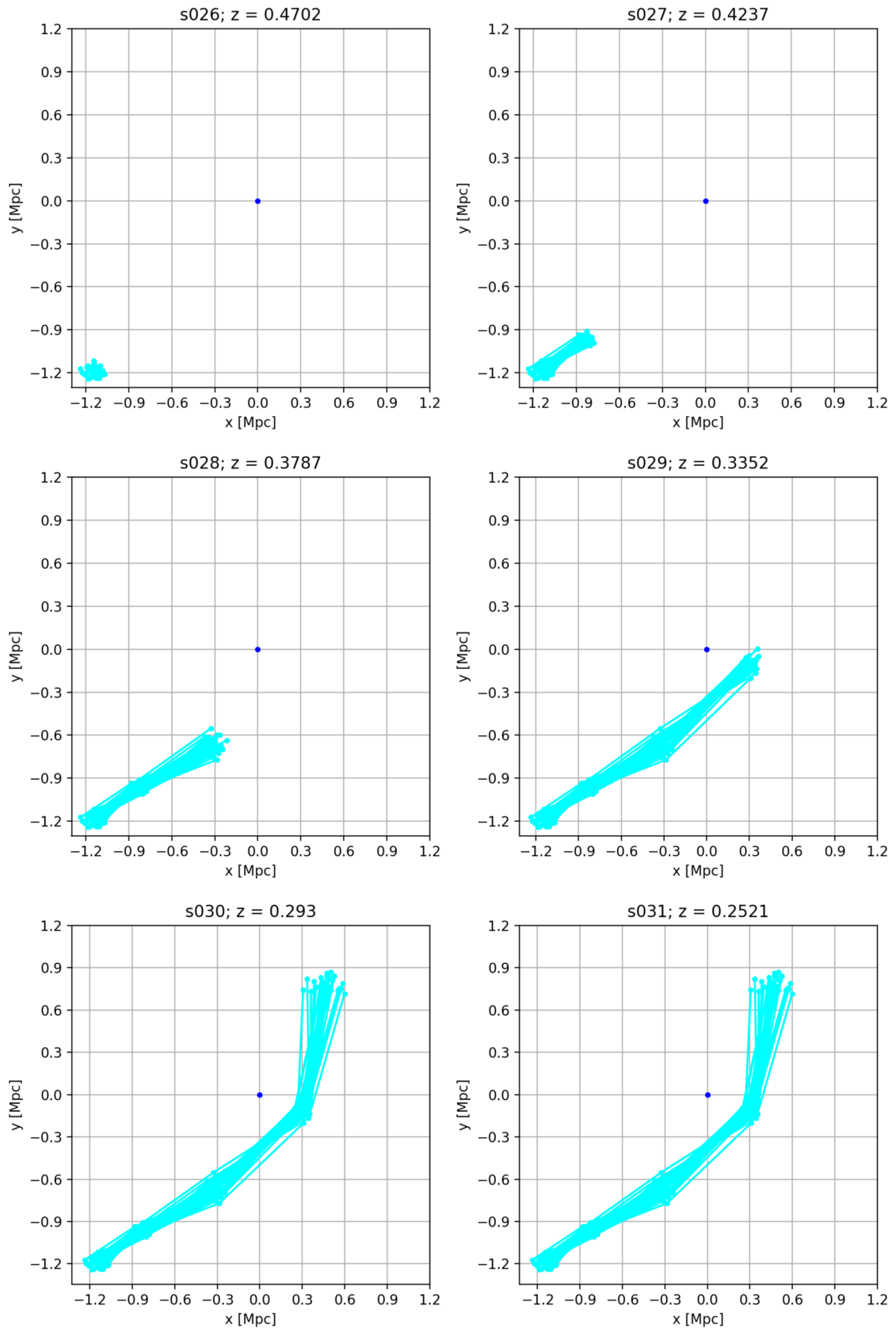


Figure 3.20: Tracks of 50 DM particles; the bottom two panels are the same because the DM particles left the shown frame.

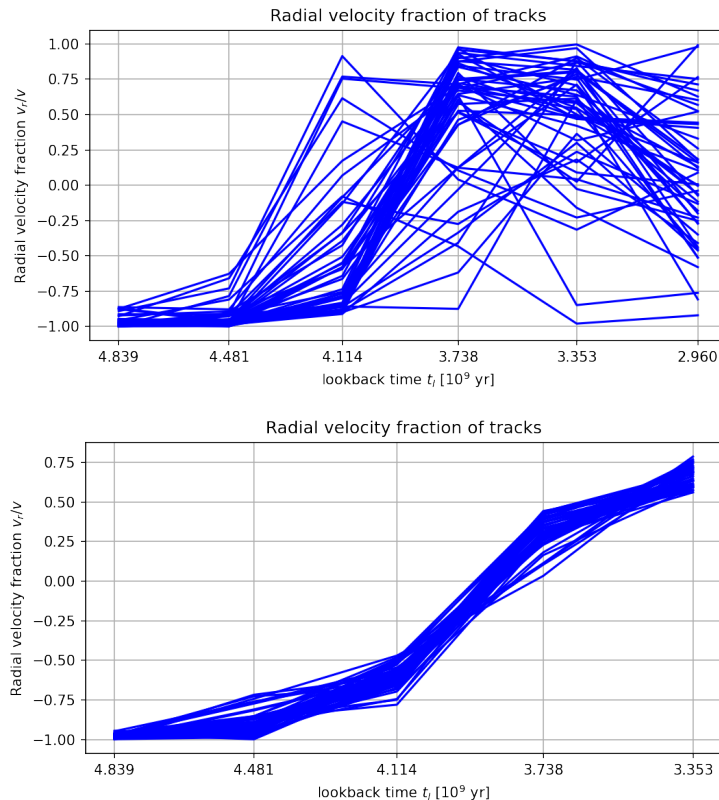


Figure 3.21: Top: Radial velocities of the gas particles; Bottom: Radial velocities of the DM particles.

3.21).

On top the radial velocity fraction of gas is shown, which is almost -1 for all 50 tracks at the beginning. The first velocities become outgoing (radial velocity fraction of almost 1) at s028 and almost all follow at s029. In the end (s031) the radial velocity fraction is randomly distributed over all radial velocity fractions, meaning there are velocities that are mostly radial and other that are mostly tangential. The directions are randomized by Coulomb collisions with the undisturbed gas of the main cluster.

On the other hand the bottom panel shows the radial velocity fraction of DM. All 50 particles have a fraction of almost -1 in the beginning, as well. On the contrary to the gas velocities they change continuous from -1 to about 0.75. Here just 5 snapshots are shown, because the DM particles leave the considered frame before s031. It is likely that they become even closer to 1 in the next snapshot. The radial velocity fractions are roughly the same for all particles in one snapshot, as they change together from snapshot to snapshot.

3.4 Temperature and Gas Density Jump Ratios and Image Arithmetic

We want to asses of which nature the temperature and density changes are. They could be adiabatic, isobaric or isothermal (no temperature change). At first the temperature and density jump from snapshot to snapshot is calculated for each particle

$$T_{j,\text{jump}} = \frac{T_j}{T_{j-1}} \quad \rho_{j,\text{jump}} = \frac{\rho_j}{\rho_{j-1}} \quad (3.2)$$

where j represents the current snapshot. This was done for each snapshot just for particles that are included in the set box in the current snapshot and the former one. Because only s026 to s031 were analysed there is no temperature jump plot for s026 as the data for s025 was not included. Scatter plots colored according to the particles temperature jump and density jump are shown in (Fig. 3.22) and (Fig. 3.23).

The difference between these scatter plots is only minimal. Particles that are heated up or are compressed have a ratio greater than one and are shown in red. Decreasing jumps (< 1) are colored blue. In both figures (Fig. 3.22, Fig. 3.23) one can see in the top right panel, that the infalling particles are slightly heated up and compressed and proceed to do so even more in the middle left panel. As they hit the center in the middle right panel this process is continued. Afterwards there is a heating and compressing bow shaped region in the top right corner of the bottom left panel. The temperature and gas density jump can be positive or negative correlated. The correlation is characterized by

$$\frac{\log(T_{j,\text{jump}})}{\log(\rho_{j,\text{jump}})} \equiv \alpha_j \quad (3.3)$$

If α_j is positive, temperature and gas density change in the same way, e.g. if temperature increases also gas density increases. If it is negative, the properties change in the opposite way, e.g. if temperature increases gas density decreases. In a more detailed analysis one would find the following values for the individual types of processes

$$\alpha = \begin{cases} 2/3 & \text{adiabatic,} & \gamma = 5/3 \\ -1 & \text{isobaric,} & \gamma = 0 \\ 0 & \text{isothermal,} & \gamma = 1 \end{cases} \quad (3.4)$$

In galaxy clusters, adiabatic changes can be attributed to (weak) shocks that propagate through the gas, isobaric variations to slow and gentle displacements of fluid from their equilibrium due to gravity and isothermal perturbations to the expansion of bubbles of relativistic gas (ejected by AGNs). This discussion follows (Churazov et al. 2016) who presented this arithmetic for X-ray images. A scatter plot colored according to α for particles with $T_{j,\text{jump}} > 1.2$ is shown in (Fig. 3.24).

In the top right panel, the middle panels and the bottom left panel in (Fig. 3.24) one can see that the heated particles of the infalling gas, the following heated particles in the center and the heated particles in the bow shaped region have $\alpha \approx 0.72$ to $\alpha \approx 1$, which can be attributed to adiabatic changes ($\alpha \approx 0.66$) like shocks or less extreme adiabatic compression and heating. Interestingly there are some particles with $\alpha \lesssim 0$ located near the center. This is investigated in (Fig. 3.25), which shows a scatter plot colored according to $\alpha < 0.1$ for particles with $t_{j,\text{jump}} > 0.95$.

There, most particles have $\alpha \approx -0.5$ to $\alpha < 0.1$, which would correspond to bubbles of relativistic gas ($\alpha \approx 0$). This matches with the fact that there are many of these particles close to the center, e.g. in the top right or middle left panel to the top right of the COM. But many of these particles probably don't belong to a bubble but are just unheated particles within the cluster farther away from the center. There are also a lot of particles close to the center with $\alpha \approx -2$ to $\alpha \approx -3$, e.g. in the top right and both middle panels. They are also visible in (Fig. 3.24). These would rather correspond to isobaric gravity displacements ($\alpha \approx -1$). But the discussion of (Churazov et al. 2016) for relativistic gas bubbles refers to cavities where the ambient pressure is in equilibrium with the gas within, which can be seen in X-ray as a drop of the thermal pressure without apparent changes in temperature. As our data does not come from X-ray images but directly from the simulation, particles within such

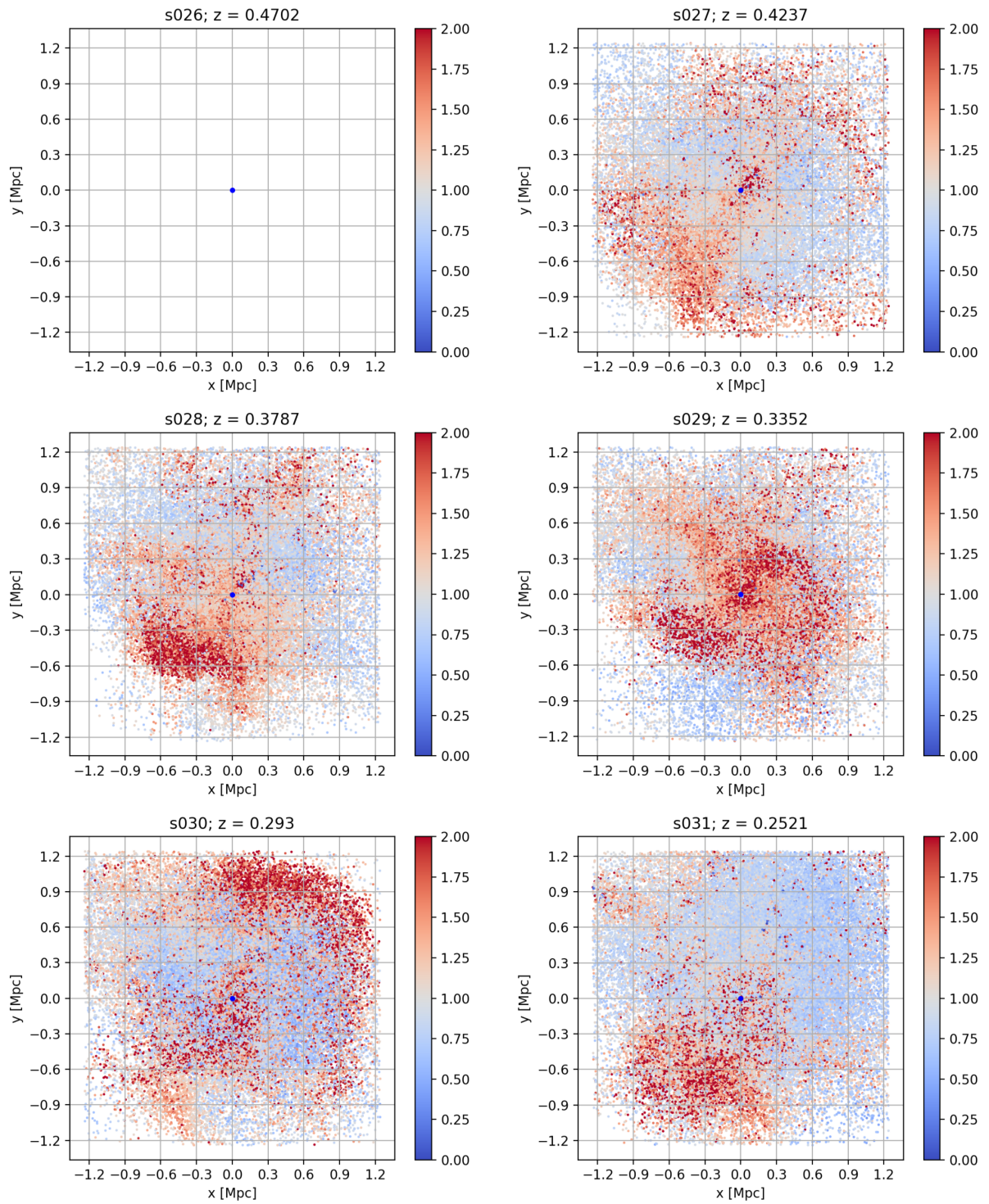


Figure 3.22: Scatter plot colored according to the temperature jump.

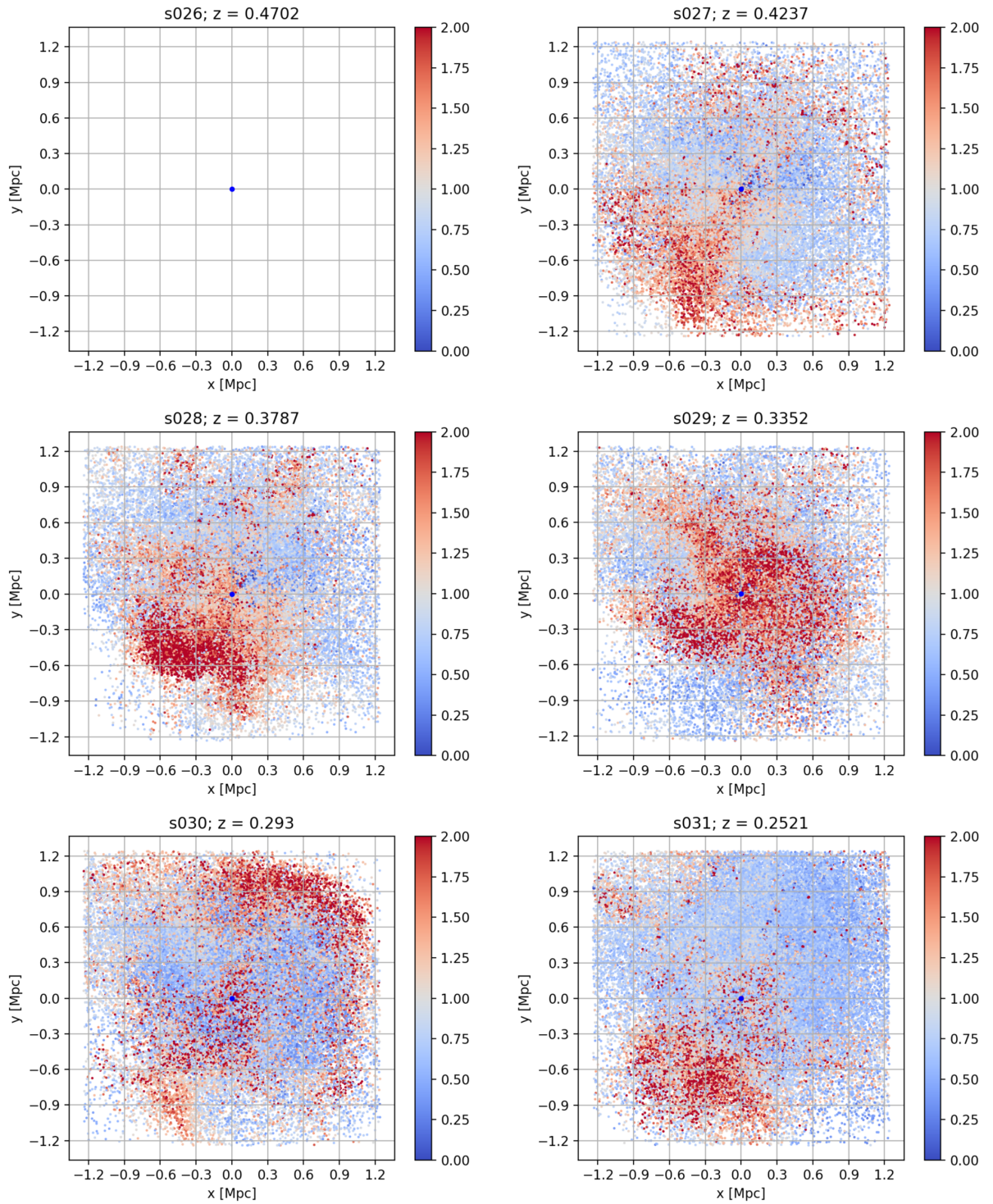


Figure 3.23: Scatter plot colored according to the gas density jump.

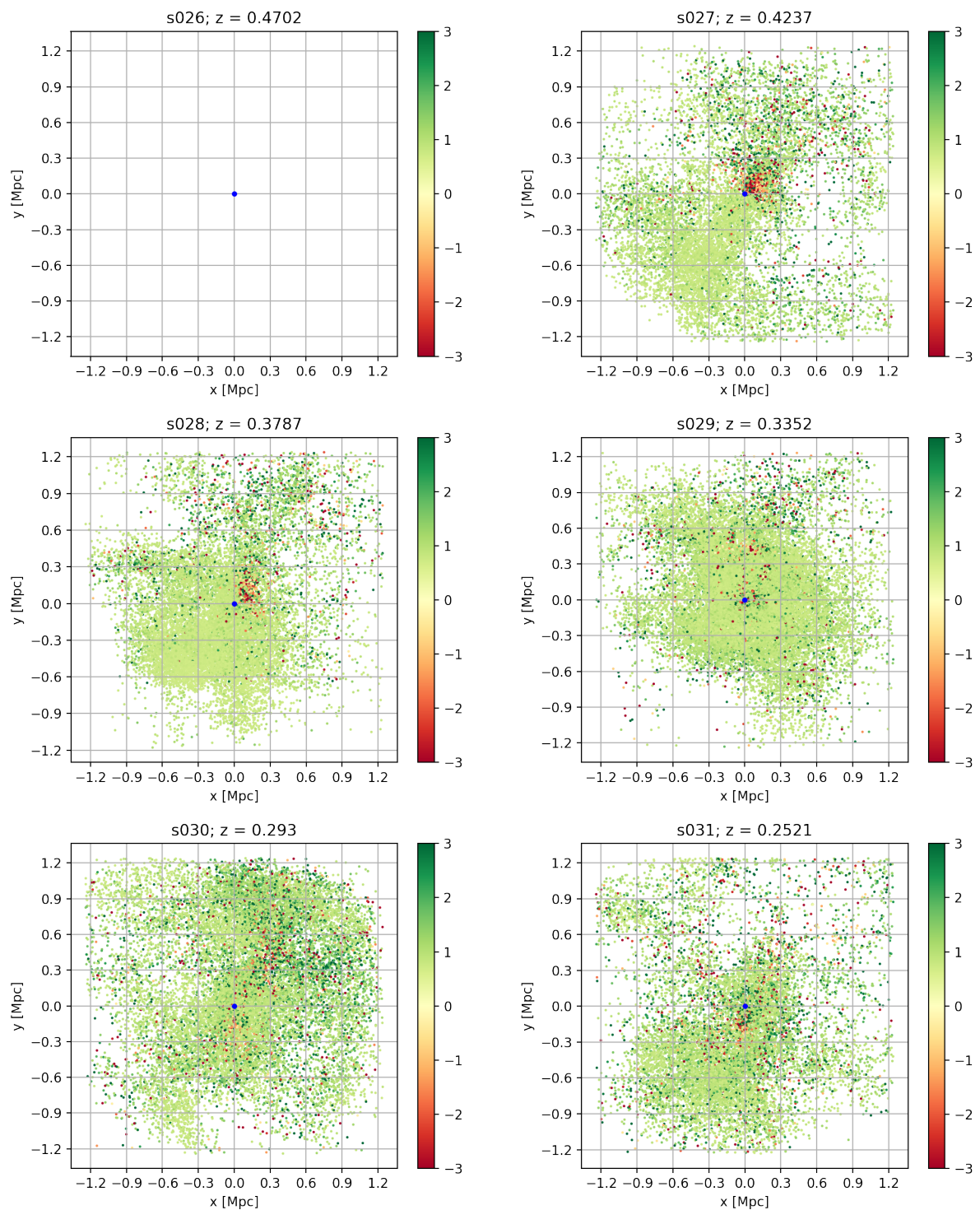


Figure 3.24: Scatter plot colored according to α for $T_{\text{jump}} > 1.2$.

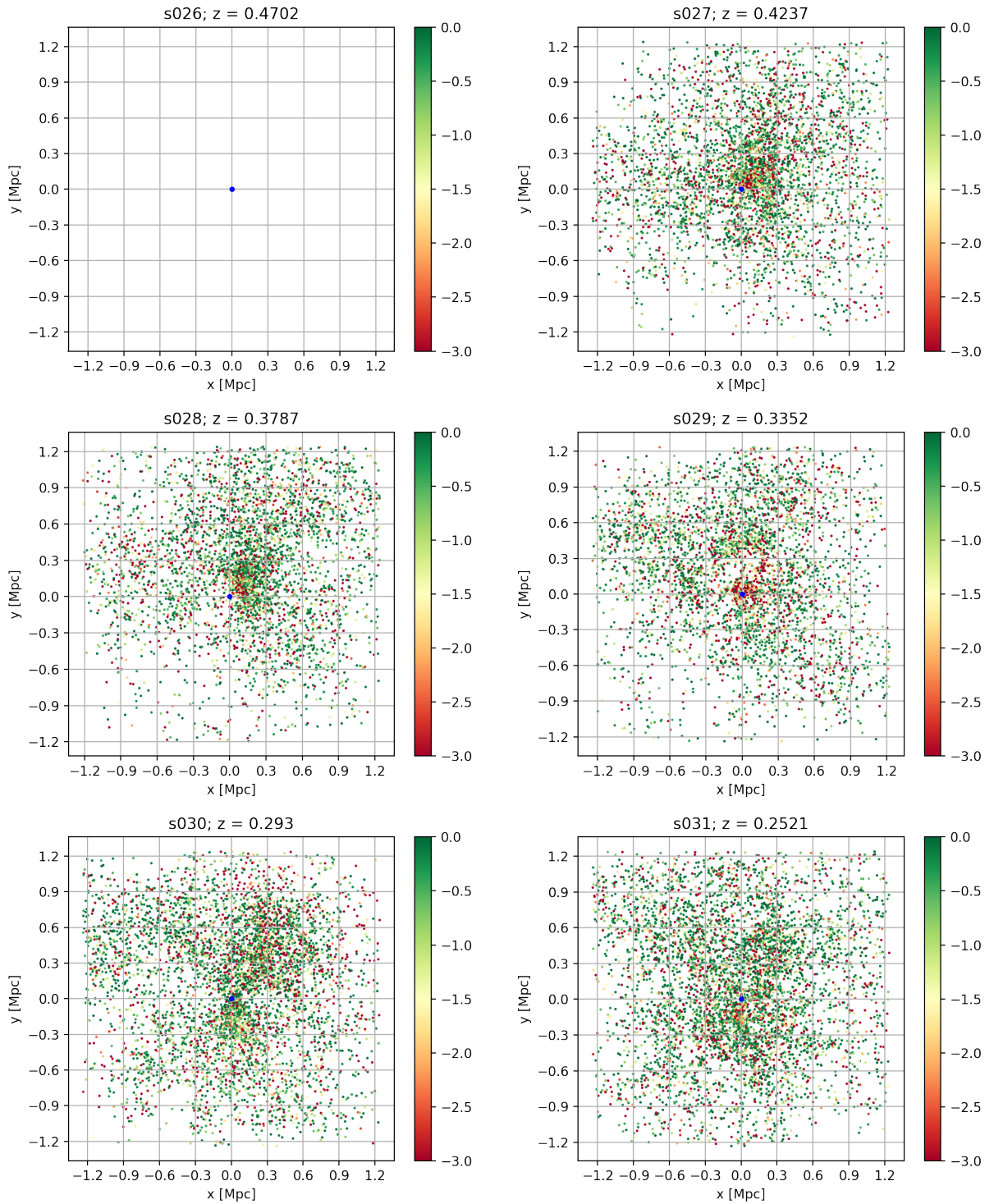


Figure 3.25: Scatter plot colored according to $\alpha < 0.1$ for $T_{\text{jump}} > 0.95$.

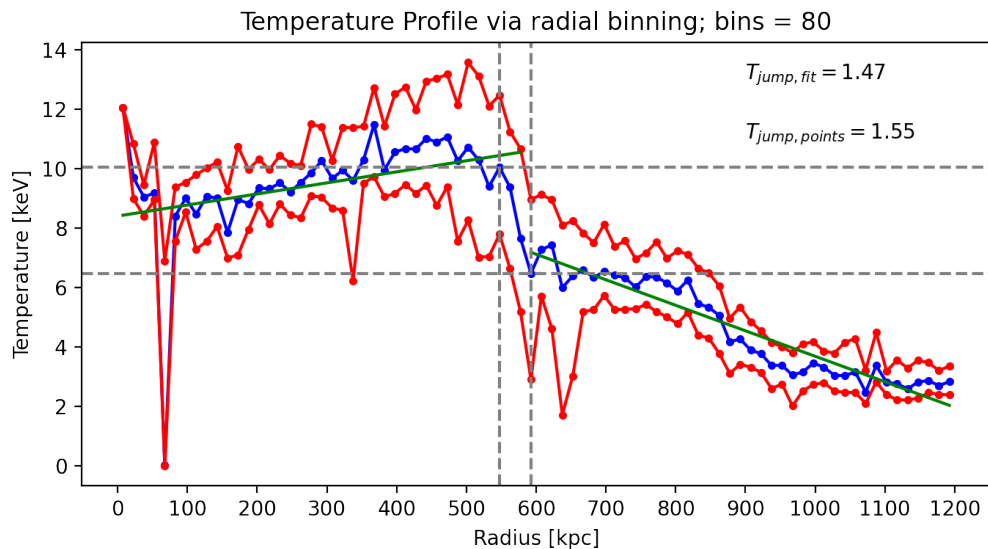


Figure 3.26: Temperature radial profile in direction of substructure; blue line: median; red lines: 32- and 68-quantiles; green: linear fit; $T_{\text{jump, points}}$ is calculated from the points where the dashed lines cross; $T_{\text{jump, fit}}$ is calculated from the maximum of the left fit over the maximum of the right fit.

a bubble are also heated by the AGN feedback and therefore α will be more negative for them. In conclusion the particles close to the center shown in (Fig. 3.25) can also represent such a bubble.

3.5 Radial Profiles via Radial Binning

Another way in which the substructure discussed in the last section can be seen are radial profiles for temperature or density. Radial profiles for such a huge number of data points can be smoothed by collecting several points close to each other in bins and calculating the median for each bin. The bins used here are spherical shells of width 15 kpc, i.e. the first shell goes from the COM to $r = 15$ kpc, the second one from $r = 15$ kpc to $r = 30$ kpc, etc. In the following snapshot s028 was further investigated. In addition to the shells the bins are also restricted to the octant in which the substructure is located. This was done for temperature (Fig. 3.26), gas density (Fig. 3.28) and entropy (Fig. 3.29). Where it is suited a linear least square fit was performed.

3.5.1 Profiles over the Infalling Substructure

In (Fig. 3.26) the temperature is high in the center, increases up to about $r = 470$ kpc, then there is a sharp decrease from $r \approx 550$ kpc to $r \approx 590$ kpc after which the temperature is steadily decreasing. As seen in (Fig. 1.1) in the situation where two gas spheres collide, two shocks will occur. One propagating in the same direction as the infalling cluster through the gas of the main cluster and one in the opposite direction though the gas of the infalling cluster. As the first shock has to move through the denser gas it is weaker and therefore not visible in the temperature profile. The detectable discontinuity represents the second shock. The temperature jump was calculated from the bins before and after the discontinuity and from a linear fit before and after the same. The results are $T_{\text{jump, points}} \approx 1.47$ and $T_{\text{jump, fit}} \approx 1.55$. From the temperature jump the Mach number of the infalling gas can be calculated using (ZuHone and Su 2022)

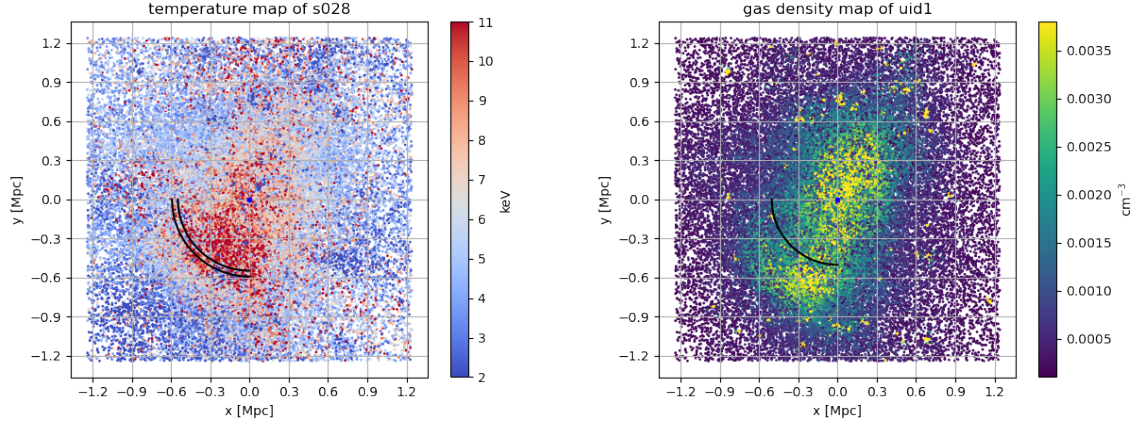


Figure 3.27: Left: Geometry of s028 in temperature and the vertical dotted lines from (Fig. 3.26); Right: Geometry of s028 in gas density and the vertical dotted line from (Fig. 3.28).

$$M = \left(\frac{(\gamma + 1)^2 (T_2/T_1 - 1)}{2\gamma(\gamma - 1)} \right)^{1/2} \quad (3.5)$$

which can be derived from the Rankine-Hugoniot jump conditions (Sec. 1.3.5). The resulting Mach number is $M_{\text{points}} \approx 1.32$ and $M_{\text{fit}} \approx 1.22$ for $\gamma = 5/3$. This velocity is not the velocity of the infalling substructure but it is close to it. The geometry of the cluster in snapshot s028 and the radii at the vertical dotted lines is shown in (Fig. 3.27).

The density profile (Fig. 3.28) doesn't show a sharp discontinuity around the same radii as the temperature profile. But it follows a similar course as it is highest in the center, declines fluctuating, reaches a local minimum at $r \approx 500$ kpc before it rises again up to $r \approx 650$ kpc before it decreases as the normal density profile does. The Mach number can not be calculated from the density profile. The lack of a discontinuity can be explained, because the density jump is smaller than the temperature jump (see Fig. 1.5). The shock is also weaker because it has to climb up the density gradient of the main cluster. Again the geometry is shown in (Fig. 3.27).

The low entropy region of the substructure can easily be seen in (Fig. 3.29). The entropy grows from the center outwards as expected (Sec. 1.4.3) until a sharp decline at $r \approx 580$ kpc. It starts to increase again after about $r \approx 980$ kpc. The geometry is shown in (Fig. 3.30).

In order to find the velocity at which the structure is infalling the radial velocity profile was produced as well. It is shown in (Fig. 3.31). The velocity difference between $r = 440$ kpc and $r = 635$ kpc is $\Delta v_{\text{rad}} \approx 1200$ km/s. The speed of sound derived from the temperature profile is $c_s \approx 1300$ km/s. This yields a Mach number (Sec. 1.3.4) of $M \approx 0.95$. It is slightly smaller than the Mach number derived from the temperature jump. In conclusion the velocity of the infalling structure can be characterized by $M \approx 1$.

3.5.2 Profile over the Whole Cluster

The radial density profile of the whole cluster obtained in the same manner (Fig. 3.32), i.e. no restriction of the spherical bins to one octant, can be compared to the observed profile of the Bullet Cluster (Fig. 1.7). They both show a bump where their substructure is located. In the simulation data at $r \approx 635$ kpc and in the Bullet cluster at $r \approx 360$ kpc. One difference

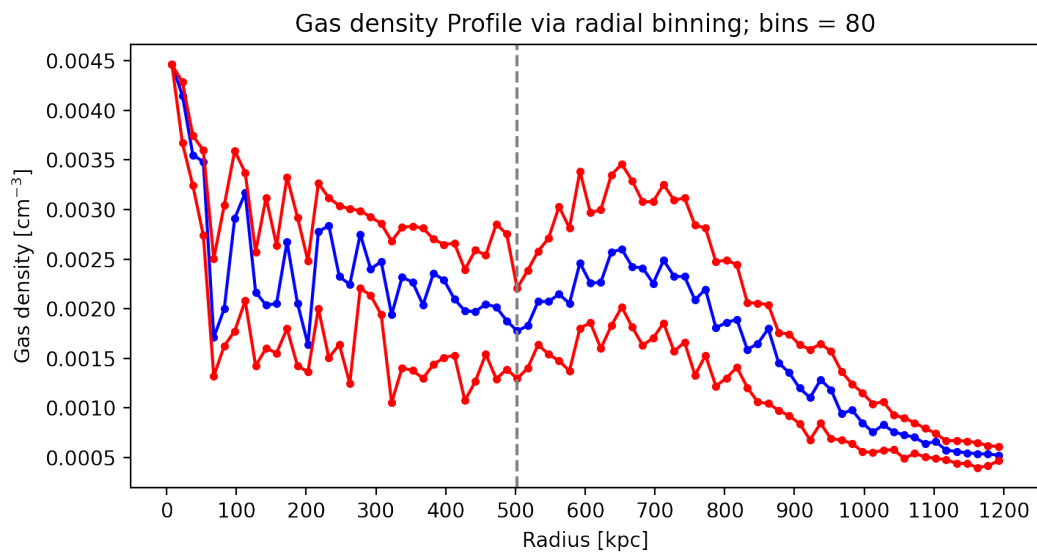


Figure 3.28: Gas density radial profile in direction of substructure; blue line: median; red lines: 32- and 68-quantiles; there is no discontinuity as in the temperature profile.

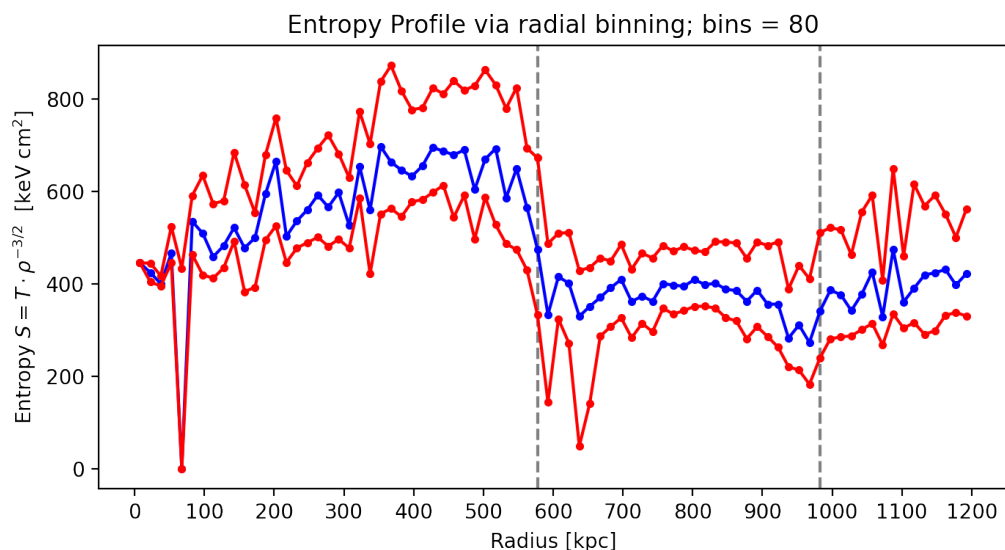


Figure 3.29: Gas density radial profile in direction of substructure; blue line: median; red lines: 32- and 68-quantiles; There is a sharp discontinuity at $r = 580$ kpc and a small one at $r = 980$ kpc.

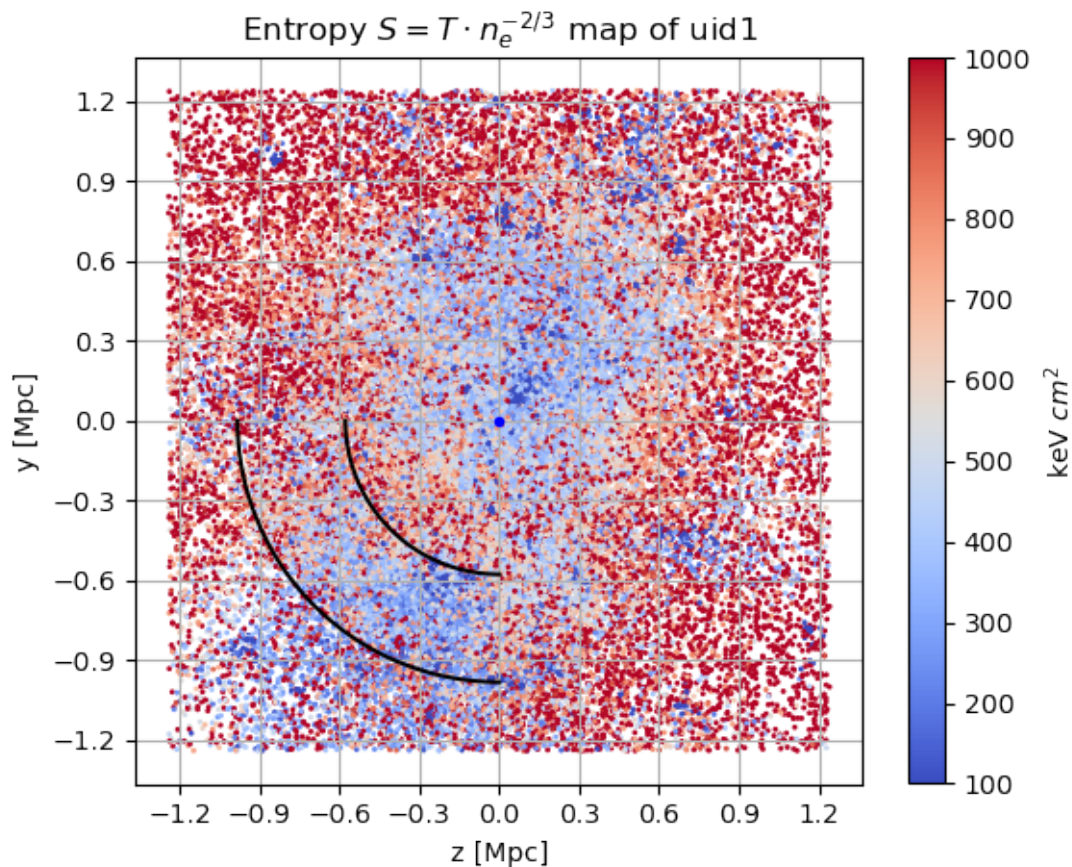


Figure 3.30: Geometry of s028 in entropy and the vertical dotted line from Fig. 3.29.

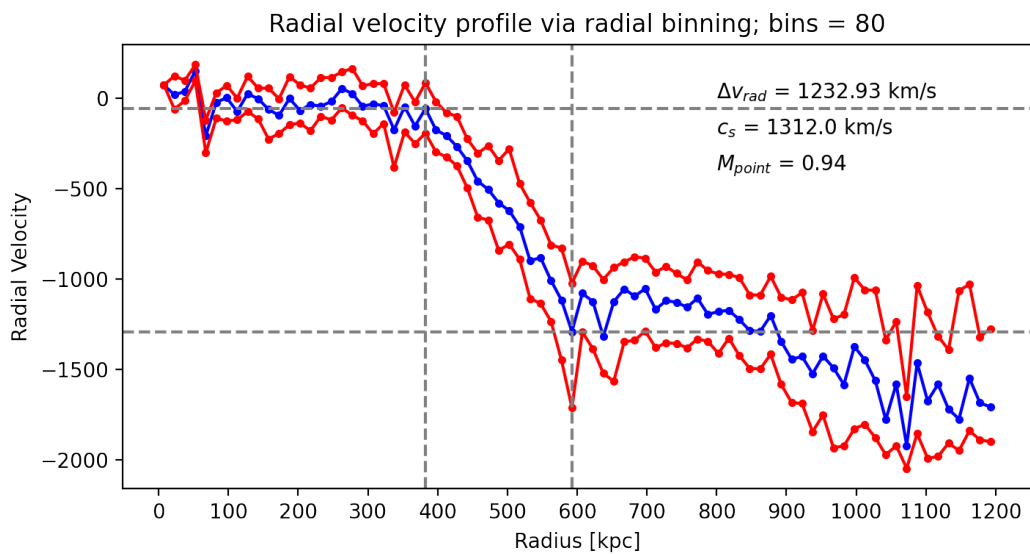


Figure 3.31: Radial velocity radial profile in the direction of the substructure; blue line: median; red lines: 32- and 68-quantiles; the velocity difference $\Delta v_{rad} \approx 1200$ km/s is calculated from the points where the dashed lines cross; $c_s \approx 1300$ km/s is calculated from the temperature in the bin at the dashed line at $r = 590$ kpc.

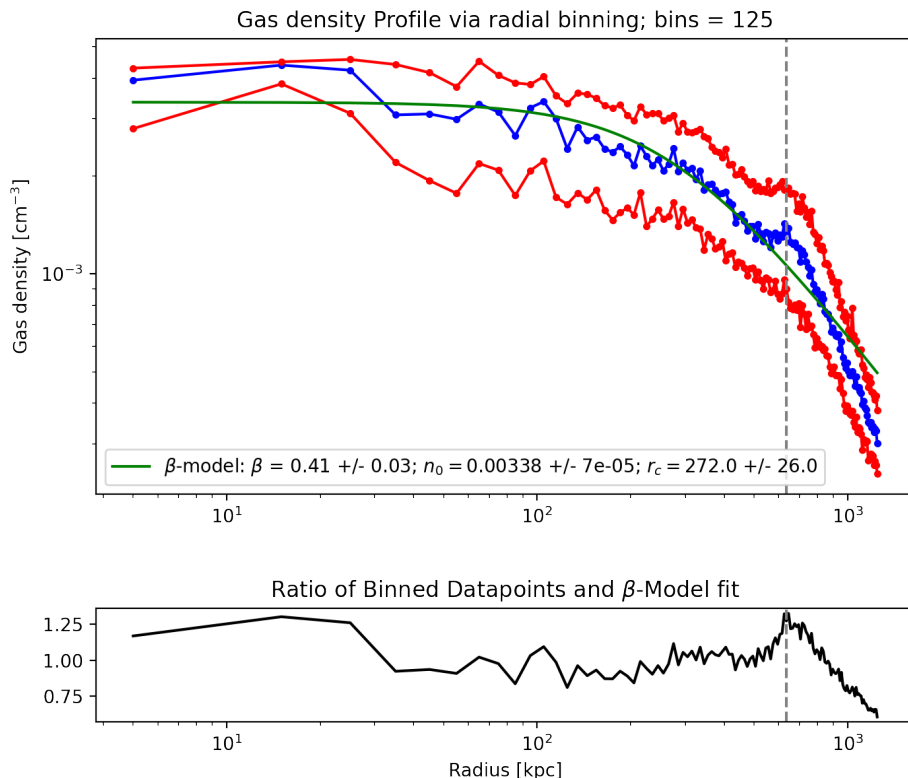


Figure 3.32: Top: Gas density radial profile for the whole cluster; blue line: median; red lines: 32- and 68-quantiles; green: fitted β -profile (Eq. 1.38); Bottom: Ratio of radial binned data points and the β -model fit; There is a peak at $r \approx 635$ kpc which is where the substructure is located.

that can not be derived from the density profile is that the substructure in the simulation is infalling and the one in the Bullet Cluster is outgoing.

3.5.3 Profile over the Outgoing Shock

At last the outgoing shock visible in the top right corner of the bottom left panel in the above scatter plots is investigated. In order to capture it completely the boundaries of the zoomed in box are increased. The temperature profile in the direction of the shock is shown in (Fig. 3.33).

There the typical profile for a shock can be observed. The temperature is almost isothermal at low radii and slightly increases up to $r \approx 1375$ kpc after which the profile shows a discontinuity and decline. The temperature jump again was calculated as for the infalling substructure. $T_{\text{jump, points}} \approx 1.67$ translates to a Mach number of $\mathbf{M}_{\text{points}} \approx 1.47$ and $T_{\text{jump, fit}} \approx 1.47$ to $\mathbf{M}_{\text{fits}} \approx 1.23$. This velocity is also comparable to the Mach number derived from the shock at the infall and the Mach number derived from the radial velocity profile. This is because the outgoing shock was caused by the infalling gas. The geometry is shown in (Fig. 3.34).

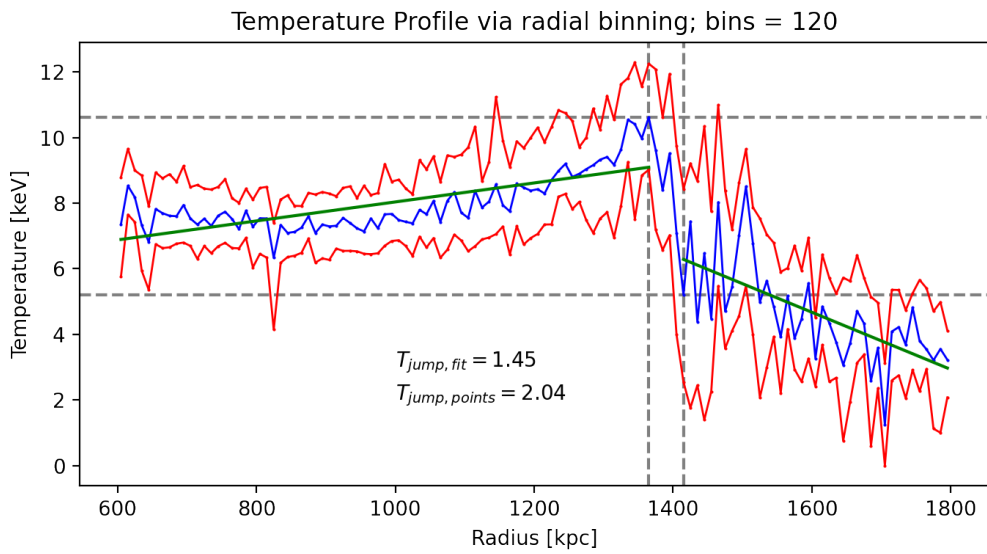


Figure 3.33: Temperature radial profile in direction of substructure; blue line: median; red lines: 32- and 68-quantiles; green: linear fit; $T_{jump, points}$ is calculated from the points where the dashed lines cross; $T_{jump, fit}$ is calculated from the maximum of the left fit over the maximum of the right fit.

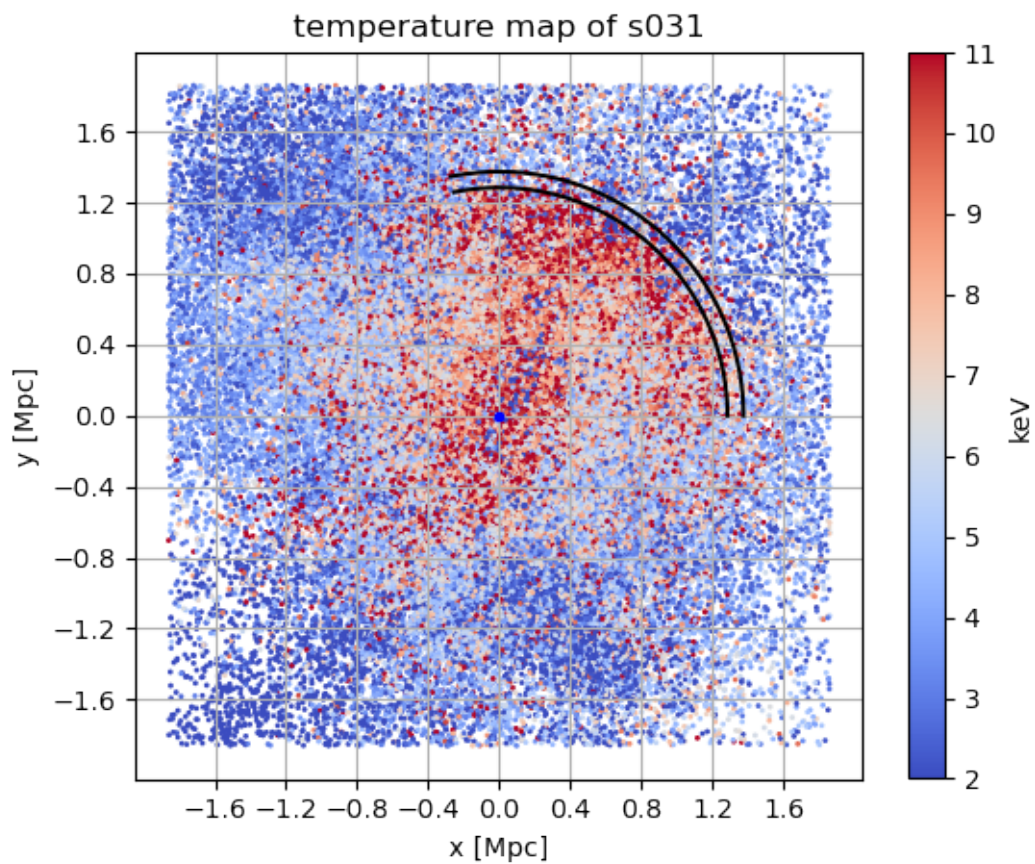


Figure 3.34: Geometry of s030 in temperature and the vertical dotted lines from (Fig. 3.33).

Chapter 4

Summary and Conclusion

4.1 Summary

Different behavior of Dark Matter and Gas

The different behavior of DM and stars to gas during a merger was confirmed in the cosmological simulation. Gas is slowed down and stopped by ram pressure and thermal pressure, while the velocity directions are randomized. DM and stars pass through the cluster collisionless and their velocity directions stay about the same all the time. Phase diagrams and real space visualisations (tracing and tracks) were used to produce this result. This is expected as DM was implemented as being collisionless and the distances between stars and galaxies is large enough, that collisions are not probable. This behaviour is observed in the Bullet cluster in the real universe.

Also the mixing of the infalling gas with the main gas cloud and the mixing of the infalling DM particles with the main DM component is different as seen in the phase diagrams. Gas is completely mixed after one core passage whereas the DM spirals around more often.

Infalling substructure and outgoing shock

Infalling (i.e. negative radial velocities) gas, DM and star particles were found. The increase of the temperature and gas density of the gas was seen in scatter plots for temperature, gas density and their jumps, evolution plots (tracing sub sample gas properties) and radial profiles. That the changes were due to adiabatic processes could be confirmed by looking at the correlation of the density and temperature changes. That means the gas is heated and compressed by adiabatic compression and shock fronts. It could also be seen that their entropy is lower than the entropy of the surrounding gas, but is steadily increasing. The increase in temperature and gas density was further investigated in radial profiles. Entropy and radial velocity profiles were produced as well. From a discontinuity in the temperature profile, the Mach number could be calculated and compared to the velocity difference in the radial velocity profile. Combining the results, the Mach number is approximately unity ($\mathbf{M} \approx 1$).

In the same manner the Mach number of the outgoing shock behind the core caused by the infalling gas was calculated to be approximately $\mathbf{M} \approx 1.3$ which is comparable to the Mach number of the infalling gas.

Metallicity evolution

Both the total metallicity and the iron to oxygen ratio for the main cluster and the infalling sub sample are increasing. No difference in the rate of the gain is visible. They both are still increasing their iron enrichment. The difference of metallicity between the sub sample and the main cluster could be used to distinguish them in X-ray observations.

AGN bubble

As a sidenote the existence of a AGN feedback bubble near the center of mass could be discussed. The gas there is heated while being diluted.

4.2 Problems

It should be noted, that structures with only a few particles could have been missed completely because only 6% of the particles were plotted. The histograms for some properties of the traced particles or the particles within one bin have large (asymmetric) wings with high values. Because of this the median was used to calculate a value for the properties as it is not as strongly effected by these wings as the mean, except for metallicity where the mean was used. All the scatter plots show a projection along the z-axis but projections along the other axes are also available. In all projections the same structures are visible. This effect also is not important for the radial profiles and the traced properties as the three dimensional data was used for the results.

4.3 Conclusion

In conclusion this work sums up a few phenomena that take place within galaxy clusters and gives an introduction to hydrodynamic simulations and how they are analyzed.

The possibility to have access to all the three dimensional information gives great insights in the physical nature but the results are not comparable to what observers see. Therefore analyses with virtual observatories like PHOX, that were neglected in this work, are important for future studies.

Since many different aspects and analysis methods were included, in the future one of these aspects could be studied in more detail and the sample of investigated clusters could be increased. By studying the steady increase of metallicity and entropy in more detail, the evolutionary stage of the merger could be estimated. The offset in metallicity between main cluster and infalling substructure could help X-ray missions to distinguish between them, as well. Especially future X-ray observatories might profit from this result.

Bibliography

- E. Anders and N. Grevesse. Abundances of the elements: Meteoritic and solar. *Geochimica et Cosmochimica Acta*, 53(1):197–214, Jan. 1989. doi: 10.1016/0016-7037(89)90286-X.
- M. Bartelmann. *Theoretische Physik*. 2015. doi: 10.1007/978-3-642-54618-1.
- M. Bartelmann. *Das kosmologische Standardmodell*. 2019. doi: 10.1007/978-3-662-59627-2.
- V. Biffi, K. Dolag, H. Böhringer, and G. Lemson. Observing simulated galaxy clusters with PHOX: a novel X-ray photon simulator. *Monthly Notices of the Royal Astronomical Society*, 420(4):3545–3556, Mar. 2012. doi: 10.1111/j.1365-2966.2011.20278.x.
- G. L. Bryan and M. L. Norman. Statistical Properties of X-Ray Clusters: Analytic and Numerical Comparisons. *The Astrophysical Journal*, 495(1):80–99, Mar. 1998. doi: 10.1086/305262.
- B. W. Carroll and D. A. Ostlie. *An Introduction to Modern Astrophysics*. 2017. doi: 10.1017/9781108380980.
- K. W. Cavagnolo, M. Donahue, G. M. Voit, and M. Sun. Intracluster Medium Entropy Profiles for a Chandra Archival Sample of Galaxy Clusters. *The Astrophysical Journal Supplement Series*, 182(1):12–32, May 2009. doi: 10.1088/0067-0049/182/1/12.
- F. F. Chen. *Introduction to Plasma Physics and Controlled Fusion*. 2016. doi: 10.1007/978-3-319-22309-4.
- E. Churazov, P. Arevalo, W. Forman, C. Jones, A. Schekochihin, A. Vikhlinin, and I. Zhuravleva. Arithmetic with X-ray images of galaxy clusters: effective equation of state for small-scale perturbations in the ICM. *Monthly Notices of the Royal Astronomical Society*, 463(1):1057–1067, Nov. 2016. doi: 10.1093/mnras/stw2044.
- D. Clowe, M. Bradač, A. H. Gonzalez, M. Markevitch, S. W. Randall, C. Jones, and D. Zaritsky. A Direct Empirical Proof of the Existence of Dark Matter. *The Astrophysical Journal*, 648(2):L109–L113, Sept. 2006. doi: 10.1086/508162.
- K. Dolag, M. Jubelgas, V. Springel, S. Borgani, and E. Rasia. Thermal Conduction in Simulated Galaxy Clusters. *The Astrophysical Journal*, 606(2):L97–L100, May 2004. doi: 10.1086/420966.
- K. Dolag, S. Borgani, S. Schindler, A. Diaferio, and A. M. Bykov. Simulation Techniques for Cosmological Simulations. *Space Science Reviews*, 134(1-4):229–268, Feb. 2008. doi: 10.1007/s11214-008-9316-5.
- K. Dolag, E. Komatsu, and R. Sunyaev. SZ effects in the Magneticum Pathfinder simulation: comparison with the Planck, SPT, and ACT results. *Monthly Notices of the Royal Astronomical Society*, 463(2):1797–1811, Dec. 2016. doi: 10.1093/mnras/stw2035.

- K. Dolag, E. Mevius, and R.-S. Remus. Distribution and Evolution of Metals in the Magneticum Simulations. *Galaxies*, 5(3):35, Aug. 2017. doi: 10.3390/galaxies5030035.
- M. Hirschmann, K. Dolag, A. Saro, L. Bachmann, S. Borgani, and A. Burkert. Cosmological simulations of black hole growth: AGN luminosities and downsizing. *Monthly Notices of the Royal Astronomical Society*, 442(3):2304–2324, Aug. 2014. doi: 10.1093/mnras/stu1023.
- D. W. Hogg. Distance measures in cosmology. *arXiv e-prints*, art. astro-ph/9905116, May 1999.
- W. Hu. Lecture Notes on Introduction to Cosmology. *University of Chicago*, 2021.
- R. Kippenhahn and A. Weigert. *Stellar Structure and Evolution*. 1990.
- E. Komatsu, K. M. Smith, J. Dunkley, C. L. Bennett, B. Gold, G. Hinshaw, N. Jarosik, D. Larson, M. R. Nolta, L. Page, D. N. Spergel, M. Halpern, R. S. Hill, A. Kogut, M. Limon, S. S. Meyer, N. Odegard, G. S. Tucker, J. L. Weiland, E. Wollack, and E. L. Wright. Seven-year Wilkinson Microwave Anisotropy Probe (WMAP) Observations: Cosmological Interpretation. *The Astrophysical Journal Supplement Series*, 192(2):18, Feb. 2011. doi: 10.1088/0067-0049/192/2/18.
- A. V. Kravtsov and S. Borgani. Formation of Galaxy Clusters. *Annual Review of Astronomy and Astrophysics*, 50:353–409, Sept. 2012. doi: 10.1146/annurev-astro-081811-125502.
- M. W. Kunz, J. Squire, S. A. Balbus, S. D. Bale, C. H. K. Chen, E. Churazov, S. C. Cowley, C. B. Forest, C. F. Gammie, E. Quataert, C. S. Reynolds, A. A. Schekochihin, L. Sironi, A. Spitkovsky, J. M. Stone, I. Zhuravleva, and E. G. Zweibel. [Plasma 2020 Decadal] The Material Properties of Weakly Collisional, High-Beta Plasmas. *arXiv e-prints*, art. arXiv:1903.04080, Mar. 2019.
- L. D. Landau and E. M. Lifshitz. *Fluid mechanics*. 1959.
- M. Markevitch and A. Vikhlinin. Shocks and cold fronts in galaxy clusters. *Physics Reports*, 443(1):1–53, May 2007. doi: 10.1016/j.physrep.2007.01.001.
- M. Markevitch, A. H. Gonzalez, D. Clowe, A. Vikhlinin, W. Forman, C. Jones, S. Murray, and W. Tucker. Direct Constraints on the Dark Matter Self-Interaction Cross Section from the Merging Galaxy Cluster 1E 0657-56. *The Astrophysical Journal*, 606(2):819–824, May 2004. doi: 10.1086/383178.
- C. Mastropietro and A. Burkert. Hydrodynamical Simulations of the Bullet Cluster (With 15 Figures). *Reviews in Modern Astronomy*, 20:228, Oct. 2008. doi: 10.1002/9783527622993.ch10.
- A. Ragagnin, K. Dolag, V. Biffi, M. Cadolle Bel, N. J. Hammer, A. Krukau, M. Petkova, and D. Steinborn. A web portal for hydrodynamical, cosmological simulations. *Astronomy and Computing*, 20:52–67, July 2017. doi: 10.1016/j.ascom.2017.05.001.
- C. L. Sarazin. X-ray emission from clusters of galaxies. *Reviews of Modern Physics*, 58(1): 1–115, Jan. 1986. doi: 10.1103/RevModPhys.58.1.
- P. Schneider. *Einführung in die extragalaktische Astronomie und Kosmologie*. 2006.
- U. Schollwöck. Lecture Notes on Thermodynamics and Statistical Physics. *Ludwig-Maximilians-Universität München*, 2021.
- L. Spitzer. *Physics of Fully Ionized Gases*. 1962.

- V. Springel. The cosmological simulation code GADGET-2. *Monthly Notices of the Royal Astronomical Society*, 364(4):1105–1134, Dec. 2005a. doi: 10.1111/j.1365-2966.2005.09655.x.
- V. Springel. User guide for GADGET-2. pages 1–46, May 2005b. doi: <https://wwwmpa.mpa-garching.mpg.de/gadget/users-guide.pdf>.
- C. Zhang, I. Zhuravleva, A. Kravtsov, and E. Churazov. Evolution of splashback boundaries and gaseous outskirts: insights from mergers of self-similar galaxy clusters. *Monthly Notices of the Royal Astronomical Society*, 506(1):839–863, Sept. 2021. doi: 10.1093/mnras/stab1546.
- J. ZuHone and Y. Su. The Merger Dynamics of the X-ray Emitting Plasma in Clusters of Galaxies. *arXiv e-prints*, art. arXiv:2202.06712, Feb. 2022.
- F. Zwicky. Die Rotverschiebung von extragalaktischen Nebeln. *Helvetica Physica Acta*, 6: 110–127, Jan. 1933.

List of Figures

1.1	The gas of merging galaxy clusters; shaded circles depict dense cores of the colliding subclusters; The shock fronts 1 and 2 in the central region will propagate to the outskirts without affecting the cores; taken from (Markevitch and Vikhlinin 2007).	2
1.2	Virial overdensities Δ_m and Δ_c for ρ_m and ρ_c as a function of the redshift z in the Λ CDM-model.	8
1.3	Massive body of mass M and smaller body of mass $m \ll M$ approximated as two smaller bodies of masses m/s in order to estimate tidal forces.	9
1.4	Composite image of the Bullet Cluster (1E 0657-56). Optical background image from HST and Magellan; <i>Chandra</i> X-ray Observatory image in pink; Projected total mass map obtained from weak lensing in blue (Clowe et al. 2006) (Image created by the <i>Chandra</i> press group).	10
1.5	The Rankine-Hugoniot jump ratios for density, pressure and temperature. For large $M \gg 1$ the density jump ratio approaches 4 while the temperature and pressure jump ratios can grow infinitely with the Mach number; The dashed lines represent relativistic gas where $\gamma = 4/3$	13
1.6	Top: Total hydrostatic mass and total gas mass profiles as given by the isothermal β -model (Eq. 1.38); Bottom: Ratio of Gas Mass and Total Mass. It suggests, that the fraction of gas is higher in the outskirts, i.e. there is more DM in the core. The typical values used are $n_g = 0.05 \text{ cm}^{-3}$, $T_g = 4 \text{ keV}$, $r_c = 100 \text{ kpc}$ and $\beta = 0.6$	15
1.7	Top: Blue dots are radial binned data points taken from the ACCEPT Archive (Cavagnolo et al. 2009); The red line is a least-square fit to the β -model (Eq. 1.38); The dashed line is at the radius 340 kpc which is roughly where the substructure is located; Bottom: Ratio of radial binned data points and the β -model fit showing a peak where the substructure is located.	16
1.8	Length (left panel) and Time scales (right panel) as predicted by the above equations and the isothermal beta model. The typical values used are $n_{g,0} = 0.05 \text{ cm}^{-3}$, $T_g = 4 \text{ keV}$, $r_c = 100 \text{ kpc}$ and $\beta = 0.6$	18
1.9	The blue dots are radial binned data points taken from the ACCEPT Archive (Cavagnolo et al. 2009); The red line is a least-square fit to the K -model (Eq. 1.54); The dashed line is at the radius 340 kpc which is roughly where the substructure is located.	19

2.1	Evolution of an orbit of a point mass around a fixed massive center and the evolution of the specific orbital energy computed with different integration schemes: Second Order Runge-Kutta (upper left panel), fourth order Runge-Kutta (upper right panel) and KDK leap-frog integration (lower panel). The energy evolution shows, that the Runge-Kutta integration schemes don't conserve energy while the leap-frog integration does. In the fourth order Runge-Kutta integration a longer time step was used for illustrative reasons.	25
2.2	Peano-Hilbert curves in 3D (top row) and 2D (bottom row). Image taken from (Springel 2005a).	29
2.3	Decomposition of the velocity \mathbf{v} into radial velocity v_r and tangential velocity v_t .	32
2.4	Idealized phase-space distribution of DM particles (black) and radial velocity profile of gas; taken from (Zhang et al. 2021).	32
3.1	X-ray emission map of the UID 1 cluster in s027; the colorbar shows the total number of counts for a virtual observation with $t_{\text{obs}} = 10^7$ s and an effective area of $A_{\text{eff}} = 10^3$ cm ² ; left panel: 20×20 Mpc/h box; right panel: zoomed in 5×5 Mpc/h box.	34
3.2	Scatter plot of gas particles colored according to their radial velocity fractions in the reference frame of the COM; green: negative (infalling); red: positive (outgoing); yellow: close to zero (mostly tangential).	35
3.3	Scatter plot of DM particles colored according to their radial velocity fractions in the reference frame of the COM; green: negative (infalling); red: positive (outgoing); yellow: close to zero (mostly tangential).	36
3.4	Scatter plot of star particles colored according to their radial velocity fractions in the reference frame of the COM; green: negative (infalling); red: positive (outgoing); yellow: close to zero (mostly tangential).	37
3.5	Scatter plot of gas particles colored according to their temperature.	38
3.6	Scatter plot of gas particles colored according to their gas density.	39
3.7	Scatter plot of gas particles colored according to their entropy.	41
3.8	Phase diagrams for gas particles.	42
3.9	Phase diagrams for DM particles.	42
3.10	Phase diagrams for star particles.	42
3.11	Phase diagrams for gas particles and traced gas particles.	43
3.12	Phase diagrams for DM particles and traced DM particles.	43
3.13	Phase diagrams for star particles and traced star particles.	43
3.14	Scatter plot of gas particles colored according to their radial velocity fractions and traced gas particles in cyan.	45
3.15	Scatter plot of DM particles colored according to their radial velocity fractions and traced DM particles in cyan.	46
3.16	Scatter plot of star particles colored according to their radial velocity fractions and traced star particles in cyan.	47

3.17	From top left to the bottom: temperature, gas density and entropy; the blue line is the median of each property, the red lines are the 32- and 68-quantile and the black line is the median of the background particles (bulk of cluster).	48
3.18	Top left: Mean of the total metallicity of the sub sample (blue) and mean of the total metallicity of the main cluster (black) in solar units; bottom left: Same as above but normalized (divided by the mean of all snapshots); top right: Mean of the ratio of the iron abundance to the oxygen abundance for the sub sample (blue) and the main cluster (black) in solar units; bottom left: Same as above but normalized.	49
3.19	Tracks of 50 gas particles.	50
3.20	Tracks of 50 DM particles; the bottom two panels are the same because the DM particles left the shown frame.	51
3.21	Top: Radial velocities of the gas particles; Bottom: Radial velocities of the DM particles.	52
3.22	Scatter plot colored according to the temperature jump.	54
3.23	Scatter plot colored according to the gas density jump.	55
3.24	Scatter plot colored according to α for $T_{\text{jump}} > 1.2$	56
3.25	Scatter plot colored according to $\alpha < 0.1$ for $T_{\text{jump}} > 0.95$	57
3.26	Temperature radial profile in direction of substructure; blue line: median; red lines: 32- and 68-quantiles; green: linear fit; $T_{\text{jump, points}}$ is calculated from the points where the dashed lines cross; $T_{\text{jump, fit}}$ is calculated from the maximum of the left fit over the maximum of the right fit.	58
3.27	Left: Geometry of s028 in temperature and the vertical dotted lines from (Fig. 3.26); Right: Geometry of s028 in gas density and the vertical dotted line from (Fig. 3.28).	59
3.28	Gas density radial profile in direction of substructure; blue line: median; red lines: 32- and 68-quantiles; there is no discontinuity as in the temperature profile.	60
3.29	Gas density radial profile in direction of substructure; blue line: median; red lines: 32- and 68-quantiles; There is a sharp discontinuity at $r = 580$ kpc and a small one at $r = 980$ kpc.	60
3.30	Geometry of s028 in entropy and the vertical dotted line from Fig. 3.29.	61
3.31	Radial velocity radial profile in the direction of the substructure; blue line: median; red lines: 32- and 68-quantiles; the velocity difference $\Delta v_{\text{rad}} \approx 1200$ km/s is calculated from the points where the dashed lines cross; $c_s \approx 1300$ km/s is calculated from the temperature in the bin at the dashed line at $r = 590$ kpc.	61
3.32	Top: Gas density radial profile for the whole cluster; blue line: median; red lines: 32- and 68-quantiles; green: fitted β -profile (Eq. 1.38); Bottom: Ratio of radial binned data points and the β -model fit; There is a peak at $r \approx 635$ kpc which is where the substructure is located.	62
3.33	Temperature radial profile in direction of substructure; blue line: median; red lines: 32- and 68-quantiles; green: linear fit; $T_{\text{jump, points}}$ is calculated from the points where the dashed lines cross; $T_{\text{jump, fit}}$ is calculated from the maximum of the left fit over the maximum of the right fit.	63

3.34	Geometry of s030 in temperature and the vertical dotted lines from (Fig. 3.33).	63
B.1	Comparison of gaussian and B_2 -spline kernel for SPH.	86

List of Tables

1.1	The cosmological parameters (from left to right): Baryon density today, Cold dark matter density today, Matter density today, Dark energy density today, Radiation density today, Hubble constant and the age of the universe today as determined by (Komatsu et al. 2011, Tab. 1, column 2) except for $\Omega_{r,0}$, which was taken from (Bartelmann 2019, p.19). From these values one finds that matter consists of about 16.7% baryons and 83.3% CDM.	5
1.2	Time and length scales that are of interest in the ICM for electrons and protons; The last two time scales were calculated as $t_{\text{Debye}} = \lambda_{\text{Debye}}/v$ and $t_{\text{Lamor}} = 2\pi\lambda_{\text{Lamor}}/v$, where $v = \sqrt{2k_B T/m}$ is the most probable velocity in a Maxwellian velocity distribution.	18
2.1	Specifications of the simulation boxes: row 2 lists the volumes of the boxes and rows 3 to 6 list the numbers of particles for each resolution level mr (medium resolution), hr (high resolution), uhr (ultra high resolution), xhr (extra high resolution). Box3/uhr and Box5/xhr were stopped at about $z \sim 2$; Box4/xhr is planned for the future and Box2b/hr was stopped at around $z \sim 0.25$. These values were taken from the <i>Magneticum Website</i> and verified in (Dolag et al. 2017).	28
C.1	Snapshot file data blocks (less important blocks are not shown).	87
C.2	Snapshot file header (less important parts are not shown)	88
D.1	Data of the UID 1 cluster in Box 2bhr for several snapshots. Data taken from the <i>Magneticum Website</i>	89

Appendices

Appendix A

Derivation of the Rankine-Hugoniot Jump Conditions

As mentioned in Sec. 1.3.5 one can derive the Rankine-Hugoniot Jump Conditions from the conservation of mass, energy and momentum

$$\rho_1 v_1 = \rho_2 v_2 \equiv j \quad (\text{A.1})$$

$$\frac{1}{2} v_1^2 + w_1 = \frac{1}{2} v_2^2 + w_2 \quad (\text{A.2})$$

$$p_1 + \rho_1 v_1^2 = p_2 + \rho_2 v_2^2 \quad (\text{A.3})$$

The following definition is useful

$$V = \frac{1}{\rho} \quad (\text{A.4})$$

The "heat function":

$$w = C_P T = \frac{\gamma p V}{\gamma - 1} = \frac{c^2}{\gamma - 1} \quad (\text{A.5})$$

The ideal gas law:

$$pV = N k_B T \quad (\text{A.6})$$

The Mach number:

$$M = \frac{v}{c_s} \quad (\text{A.7})$$

From (A.4) and (A.1) the velocities can be written as

$$v_1 = j V_1 \quad v_2 = j V_2 \quad (\text{A.8})$$

Inserting (A.8) into (A.3) yields

$$\begin{aligned}
 p_1 + j^2 V_1 &= p_2 + j^2 V_2 \iff p_2 - p_1 = j^2 (V_1 - V_2) \\
 j^2 &= \frac{p_2 - p_1}{V_1 - V_2}
 \end{aligned} \tag{A.9}$$

Starting with (A.2)

$$\begin{aligned}
 w_1 - w_2 &= \frac{1}{2}(v_2^2 - v_1^2) \stackrel{(A.1)}{=} \frac{1}{2}j^2(\rho_2^{-2} - \rho_1^{-2}) \stackrel{(A.4)}{=} \frac{1}{2}j^2(V_2^2 - V_1^2) = \\
 &\stackrel{(A.9)}{=} \frac{1}{2}(p_2 - p_1)\frac{V_2^2 - V_1^2}{V_1 - V_2} = -\frac{1}{2}(p_2 - p_1)(V_1 + V_2) = \frac{1}{2}(p_1 - p_2)(V_1 + V_2) \\
 &\stackrel{(A.5)}{\iff} \frac{2\gamma p_1 V_1}{\gamma - 1} - \frac{2\gamma p_2 V_2}{\gamma - 1} = V_1 p_1 + p_1 V_2 - p_2 V_1 - p_2 V_2 \\
 &\iff \frac{2\gamma}{\gamma - 1} p_1 V_1 - \frac{2\gamma}{\gamma - 1} p_2 V_2 - p_1 V_1 + p_2 V_2 = V_2 p_1 - V_1 p_2 \\
 &\iff \left(\frac{2\gamma}{\gamma - 1} - 1\right) p_1 V_1 - \left(\frac{2\gamma}{\gamma - 1} - 1\right) p_2 V_2 = V_2 p_1 - V_1 p_2 \\
 &\iff \left(\frac{\gamma + 1}{\gamma - 1}\right) p_1 V_1 - \left(\frac{\gamma + 1}{\gamma - 1}\right) p_2 V_2 = V_2 p_1 - V_1 p_2 \\
 &\stackrel{\cdot V_1^{-1}}{\iff} \frac{\gamma + 1}{\gamma - 1} p_1 - \frac{\gamma + 1}{\gamma - 1} p_2 \frac{V_2}{V_1} = p_1 \frac{V_2}{V_1} - p_2 \\
 &\iff \frac{V_2}{V_1} \left(\frac{\gamma + 1}{\gamma - 1} p_2 + p_1\right) = p_2 + \frac{\gamma + 1}{\gamma - 1} p_1 \\
 &\iff \frac{V_2}{V_1} \left(\frac{(\gamma + 1)p_2 + (\gamma - 1)p_1}{\gamma - 1}\right) = \left(\frac{(\gamma - 1)p_2 + (\gamma + 1)p_1}{\gamma - 1}\right) \\
 \frac{V_2}{V_1} &= \frac{\left((\gamma + 1)p_1 + (\gamma - 1)p_2\right)(\gamma - 1)}{(\gamma - 1)\left((\gamma + 1)p_2 + (\gamma - 1)p_1\right)} = \frac{(\gamma + 1)p_1 + (\gamma - 1)p_2}{(\gamma + 1)p_2 + (\gamma - 1)p_1}
 \end{aligned} \tag{A.10}$$

From the ideal gas law (A.6)

$$\frac{T_2}{T_1} = \frac{p_2 V_2}{p_1 V_1} \tag{A.11}$$

Inserting (A.10) into (A.9)

$$\begin{aligned}
 j^2 &= \frac{p_2 - p_1}{V_1 - V_1 \frac{(\gamma + 1)p_1 + (\gamma - 1)p_2}{(\gamma + 1)p_2 + (\gamma - 1)p_1}} = \frac{(p_2 - p_1)/V_1}{1 - \frac{(\gamma + 1)p_1 + (\gamma - 1)p_2}{(\gamma + 1)p_2 + (\gamma - 1)p_1}} = \\
 &= \frac{\left((\gamma - 1)p_1 + (\gamma + 1)p_2\right)(p_2 - p_1)/V_1}{(\gamma - 1)p_1 + (\gamma + 1)p_2(\gamma + 1)p_1 - (\gamma - 1)p_2} = \frac{\left((\gamma - 1)p_1 + (\gamma + 1)p_2\right)(p_2 - p_1)/V_1}{2(p_2 - p_1)} = \\
 j^2 &= \frac{(\gamma - 1)p_1 + (\gamma + 1)p_2}{2V_1}
 \end{aligned} \tag{A.12}$$

Inserting (A.12) in (A.8)

$$v_1^2 = j^2 V_1^2 \stackrel{(A.12)}{=} \frac{1}{2} \left((\gamma - 1)p_1 + (\gamma + 1)p_2 \right) V_1 \stackrel{(A.5)}{=} \frac{c_1^2}{2\gamma} (\gamma - 1 + (\gamma + 1)p_2/p_1) \tag{A.13}$$

Now we can finally start with the jump ratios. Starting with pressure: Inserting (A.7) into (A.13)

$$\begin{aligned}
v_1^2 &= \frac{v_1^2}{2\gamma M_1^2}(\gamma - 1 + (\gamma + 1)p_2/p_1) \iff 2 = \frac{\gamma - 1}{\gamma M_1^2} + \frac{p_2(\gamma + 1)}{p_1\gamma M_1^2} \\
&\iff 2 - \frac{\gamma - 1}{\gamma M_1^2} = \frac{p_2}{p_1} \frac{\gamma + 1}{\gamma M_1^2} \iff \\
&\frac{p_2}{p_1} = \frac{2\gamma M_1^2}{\gamma + 1} - \frac{\gamma - 1}{\gamma + 1}
\end{aligned} \tag{A.14}$$

Now the density ratio. Combining (A.10) and (A.4):

$$\begin{aligned}
\frac{\rho_2}{\rho_1} &= \frac{V_1}{V_2} = \frac{(\gamma - 1)p_1 + (\gamma + 1)p_2}{(\gamma + 1)p_1 + (\gamma - 1)p_2} = \frac{(\gamma - 1) + (\gamma + 1)p_2/p_1}{(\gamma + 1) + (\gamma - 1)p_2/p_1} \stackrel{(A.14)}{=} \\
&= \frac{(\gamma - 1) + (\gamma + 1)\frac{2\gamma M_1^2 - \gamma + 1}{\gamma + 1}}{(\gamma + 1) + (\gamma - 1)\frac{2\gamma M_1^2 - \gamma + 1}{\gamma + 1}} = \frac{\gamma - 1 + 2\gamma M_1^2 - \gamma + 1}{\gamma + 1 + \frac{\gamma - 1}{\gamma + 1}(2\gamma M_1^2 - \gamma + 1)} = \\
&= \frac{2\gamma M_1^2(\gamma + 1)}{(\gamma + 1)^2 + (\gamma - 1)(2\gamma M_1^2 - \gamma + 1)} = \frac{2\gamma M_1^2(\gamma + 1)}{(\gamma + 1)^2 + 2\gamma M_1^2(\gamma - 1) - (\gamma + 1)^2} = \\
&= \frac{2\gamma M_1^2(\gamma + 1)}{2\gamma M_1^2(\gamma - 1) + \gamma^2 + 2\gamma + 1 - \gamma^2 + 2\gamma - 1} = \frac{2\gamma M_1^2(\gamma + 1)}{2\gamma M_1^2(\gamma - 1) + 4\gamma} = \\
&\frac{\rho_2}{\rho_1} = \frac{V_1}{V_2} \stackrel{(A.8)}{=} \frac{v_1}{v_2} = \frac{M_1^2(\gamma + 1)}{M_1^2(\gamma - 1) + 2}
\end{aligned} \tag{A.15}$$

At last the temperature ratio. Starting with (A.11) and (A.4):

$$\begin{aligned}
\frac{T_2}{T_1} &= \frac{p_2 V_2}{p_1 V_1} = \frac{p_2 \rho_1}{p_1 \rho_2} \stackrel{(A.11), (A.14)}{=} \frac{2\gamma M_1^2 - (\gamma - 1)}{\gamma + 1} \cdot \frac{(\gamma - 1) + 2/M_1^2}{\gamma + 1} = \\
\frac{T_2}{T_1} &= \frac{(2\gamma M_1^2 - (\gamma - 1))((\gamma - 1)M_1^2 + 2)}{(\gamma + 1)^2 M_1^2}
\end{aligned} \tag{A.16}$$

Appendix B

Methodology

B.1 Python Code Orbit

```
import numpy as np
import matplotlib.pyplot as plt

def grav(M,m,R,r,G):
    """
    Calculate the gravitational force between two masses
    M    is a scalar of one mass
    m    is a scalar of the other mass
    R    is a 1 x 3 matrix of the position of one mass
    r    is a 1 x 3 matrix of the position of the other mass
    G    is the gravitational constant (6.67430e-11 Nm2kg-2)
    """
    dx = R[0] - r[0]
    dy = R[1] - r[1]
    dz = R[2] - r[2]
    d = np.sqrt(dx**2 + dy**2 + dz**2)
    f = np.zeros(3)
    f[0] = G*M*m*dx/d**3
    f[1] = G*M*m*dy/d**3
    f[2] = G*M*m*dz/d**3

    return f

def KDK(Nt, dt, r, R, vel, M, m, G):
    """
    Loop for a KDK leap-frog integration
    Nt   is a scalar of the total number of time steps
    dt   is a scalar of a time step
    r    is a N x 3 matrix of the position of one particle
    R    is a 1 x 3 matrix of the position of the center
    vel  is a 1 x 3 matrix of the velocity
    M    is a scalar of the center mass
    m    is a scalar of the particle mass
    G    is the gravitational constant (6.67430e-11 Nm2kg-2)
    """
```

```

#save positions
r_save = np.zeros((Nt+1, 3))
r_save[0] = r
for i in range(Nt):
    vel = vel + grav(M,m,R,r,G)/m*dt/2 # 1/2 kick
    r = r + vel*dt #drift
    vel = vel + grav(M,m,R,r,G)/m*dt/2 # 1/2 kick
    r_save[i+1] = r
return r_save

def DKD(Nt, dt, r, R, vel, M, m, G):
    """
    Loop for a KDK leap-frog integration
    Nt is a scalar of the total number of time steps
    dt is a scalar of a time step
    r is a N x 3 matrix of the position of one particle
    R is a 1 x 3 matrix of the position of the center
    vel is a 1 x 3 matrix of the velocity
    M is a scalar of the center mass
    m is a scalar of the particle mass
    G is the gravitational constant (6.67430e-11 Nm2kg-2)
    """

    #save positions
    r_save = np.zeros((Nt+1, 3))
    r_save[0] = r

    for i in range(Nt):
        r = r + vel*dt/2 # 1/2 drift
        vel = vel + grav(M,m,R,r,G)/m*dt #kick
        r = r + vel*dt/2 # 1/2 drift
        r_save[i+1] = r
    return r_save

def second_RK(Nt, dt, r, R, vel, M, m, G):
    """
    Loop for a second order Runge-Kutta integration
    Nt is a scalar of the total number of time steps
    r is a N x 3 matrix of the position of one particle
    R is a 1 x 3 matrix of the position of the center
    vel is a 1 x 3 matrix of the velocity
    M is a scalar of the center mass
    m is a scalar of the particle mass
    G is the gravitational constant (6.67430e-11 Nm2kg-2)
    """

    #save positions
    r_save = np.zeros((Nt+1, 3))
    r_save[0] = r

    for i in range(Nt):

```

```

    k_1 = grav(M,m,R, r ,G)/m
    h_1 = vel
    k_2 = grav(M,m,R, r+h_1*dt ,G)/m
    h_2 = vel+k_1*dt
    vel = vel + 0.5*(k_1+k_2)*dt
    r = r + 0.5*(h_1+h_2)*dt
    r_save[i+1] = r
return r_save

```

```
def fourth_RK_energy(Nt, dt, r, R, vel, M, m, G):
```

```
    """
```

```
    Loop for a second order Runge–Kutta integration
```

```
    Nt is a scalar of the total number of time steps
```

```
    r is a N x 3 matrix of the position of one particle
```

```
    R is a 1 x 3 matrix of the position of the center
```

```
    vel is a 1 x 3 matrix of the velocity
```

```
    M is a scalar of the center mass
```

```
    m is a scalar of the particle mass
```

```
    G is the gravitational constant (6.67430e-11 Nm2kg-2)
```

```
    """
```

```
#save positions
```

```
r_save = np.zeros((Nt+1, 3))
```

```
r_save[0] = r
```

```
for i in range(Nt):
```

```
    k_1_v = grav(M,m,R, r ,G)/m
```

```
    k_1_r = vel
```

```
    k_2_v = grav(M,m,R, r+k_1_r*dt/2,G)/m
```

```
    k_2_r = vel+k_1_v*dt/2
```

```
    k_3_v = grav(M,m,R, r+k_2_r*dt/2,G)/m
```

```
    k_3_r = vel+k_2_v*dt/2
```

```
    k_4_v = grav(M,m,R, r+k_3_r*dt ,G)/m
```

```
    k_4_r = vel+k_3_v*dt
```

```
    vel = vel + dt/6*(k_1_v+2*k_2_v+2*k_3_v+k_4_v)
```

```
    r = r + dt/6*(k_1_r+2*k_2_r+2*k_3_r+k_4_r)
```

```
    r_save[i+1] = r
```

```
return r_save
```

B.2 Comparison of a Gaussian and B_2 -spline Kernel for SPH

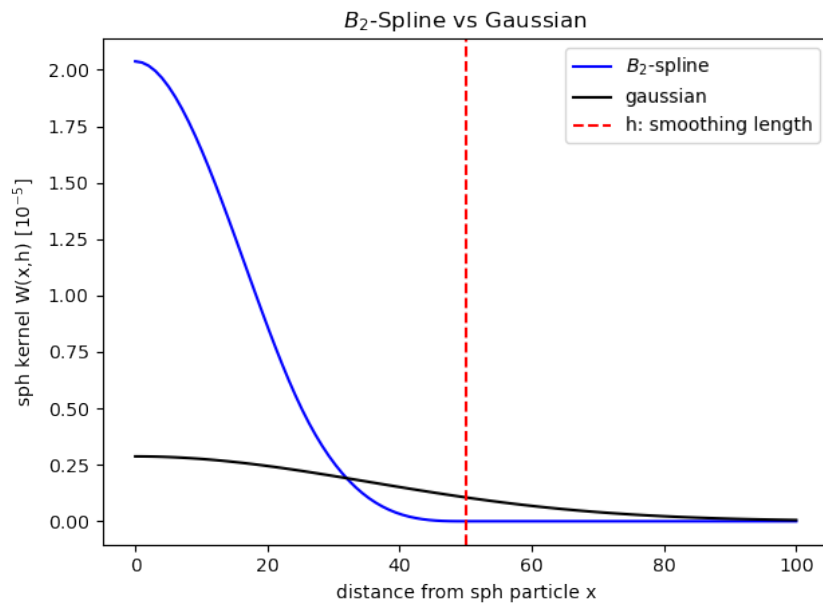


Figure B.1: Comparison of gaussian and B_2 -spline kernel for SPH.

Appendix C

Snapshot File

C.1 Snapshot Blocks

#	format 2 identifier	block content
1	'HEAD'	File header
2	'POS '	Particle positions
3	'VEL '	Particle velocities
4	'ID '	Particle IDs
5	'MASS'	Mass of particles ^a
6	'U '	Internal energy of gas particles
7	'RHO '	Density
8	'NE '	Number density of free electrons
9	'NH '	Number density of neutral hydrogen
10	'HSML'	Variable smoothing length of gas particles h
11	'SFR '	Star formation rate
12	'AGE '	Expansion factor at which star (or BH) is born
19	'POT '	Potential
20	'PHID'	dPotential/dt
21	'ABVC'	Artificial bulk viscosity constant for gas particle
24	'TNGB'	True number of neighbors (gas particles) (N_{sph})
26	'Zs '	Metallicity (e.g. Composition) of gas and stars (11 dimensions)
29	'TEMP'	mean gas temperature [K]

Table C.1: Snapshot file data blocks (less important blocks are not shown).

C.2 Snapshot Header

#	name	description
1	npart	Number of particles in the snapshot per type
2	massarr	Mass of particles per type ^a
3	time	Time of snapshot
4	z	Redshift of snapshot
7	nall	Total number of particles in the simulation per particle type
9	num_files	Number of snapshots over which the simulation data is distributed
10	boxsize	Total size of the simulation box
11	omega_0	Omega matter
12	omega_l	Omega dark energy
13	h0	dimensionless Hubble constant
21	fill	The HEAD block needs to be filled with zeros to have a size of 256 bytes

Table C.2: Snapshot file header (less important parts are not shown)

a: If a particle type has a constant mass for each particle its value is stored in the massarr in the header. If a particle type has a non constant mass the corresponding element in massarr will be zero and the masses will be stored in the 'MASS' block.

Appendix D

Data of the Investigated UID1 Cluster

The investigated cluster has the UID 1 in the *Magneticum* Box 2bhr. The cosmological parameters are $\Omega_c = 0.272$, $\Omega_\Lambda = 0.728$ and $h = 0.704$. r_{500c} is the radius of a sphere within which the mean density is 500 times the critical density at the respective redshift z . The sphere is centered on the center of the cluster. m_{500c} is the total mass within this sphere (See Sec. 1.3.2).

snapshot number	redshift z	r_{500c} [kpc/h]	m_{500c} [M_\odot/h]	T [keV]
s026	0.47019408	1180.01	4.78589E14	6.23096
s027	0.42372720	1157.33	4.72399E14	6.49616
s028	0.37872894	1252.78	6.28383E14	6.8865
s029	0.33515290	1283.52	7.10309E14	8.36688
s030	0.29295412	1307.45	7.90967E14	7.76548
s031	0.25208907	1262.35	7.51708E14	7.31031

Table D.1: Data of the UID 1 cluster in Box 2bhr for several snapshots. Data taken from the *Magneticum* Website.

Acknowledgements

Am Ende möchte ich mich noch bei einigen Personen bedanken, die mir sehr beim Verfassen dieser Arbeit geholfen haben.

Beginnend bei meinen Betreuern PD Dr. Klaus Dolag und Dr. Ildar Khabibullin. Sie waren nicht nur in den wöchentlichen Meetings für Fragen offen, sondern jeden Tag der Woche. Dabei wurden mir alle Fragen beantwortet aber auch jedes Mal neue Aufgaben gestellt, von denen ich anfangs dachte, ich könnte sie nicht bewältigen, was sich aber dank ihrer Hilfe als falsch herausstellte. Auch die lobenden Worte haben mich jede Woche wieder motiviert die nötige Zeit und Arbeit in das Lösen der Probleme zu stecken. Zusätzlicher Antrieb brachte auch das Teilnehmen an den Meetings der CAST Gruppe, welche interessante Themen beinhalteten. Man fühlte sich der Gruppe sofort sehr zugehörig, da man auch von den anderen Teilnehmern freundlich aufgenommen wird. Deswegen auch vielen Dank für das Einbeziehen in die Gruppe. Besondere Dank gilt Ildar für die häufigen zusätzlichen Meetings, ob an der Sternwarte oder über Zoom, und außerdem für das Korrekturlesen der Arbeit. Auch für das gemeinsame Überprüfen meines Codes bin ich sehr dankbar.

Weitere Dank gilt Stephan Vladutescu-Zopp für das Heraussuchen der solaren Metallizitätsliste und produzieren der Photonenliste für das untersuchte Cluster.

Vielen Dank auch an Tadziu Hoffmann für das Bereitstellen des persönlichen USM Accounts, mit dem ich auf den Servern der Sternwarte arbeiten konnte.

Bei Julian Sommer, welcher letztes Jahr seine Bachelorarbeit bei Klaus geschrieben hat, möchte ich mich für das Bereitstellen des LaTeX-Template bedanken.

Vielen Dank an Dr. Eugene Churazov, der sich meine Bachelorarbeit durchgelesen hat.

Zusätzlich möchte ich meinen Kommilitonen, welche mit mir in der Bibliothek oder im Computerraum der Sternwarte gesessen sind, um an ihrer Bachelorarbeit zu arbeiten, danken. Dadurch war die Umstellung vom strikten Zeitplan der vorherigen Semester, zum selbständigen Arbeiten einfacher.

Als Letztes gilt meiner Familie und Freunden Dank, für welche ich manchmal weniger Zeit hatte als zuvor. Außerdem waren sie nicht genervt, wenn ich wieder einmal zu viel über die Inhalte der Arbeit erzählt habe.

Vielen Dank an alle, die mich beim Erstellen der Arbeit und darüber hinaus beim Physik Studium unterstützen und weiterhin unterstützen werden.

Selbstständigkeitserklärung

Ich versichere hiermit, die vorliegende Arbeit mit dem Titel

Tracing of Gas Properties in Merging Galaxy Clusters in *Magneticum*

selbstständig verfasst zu haben und keine anderen als die angegebenen Quellen und Hilfsmittel verwendet zu haben.

Vorname, Name

München, den 15. Juli 2022